

The Pennsylvania State University
The Graduate School
Department of Electrical Engineering

IONIC ELECTROACTIVE POLYMER COMPOSITE ACTUATORS

A Dissertation in
Electrical Engineering
by
Yang Liu

© 2012 Yang Liu

Submitted in Partial Fulfillment
of the Requirements
for the Degree of

Doctor of Philosophy

August 2012

The dissertation of Yang Liu was reviewed and approved* by the following:

Qiming Zhang
Distinguished Professor of Electrical Engineering
Dissertation Advisor
Chair of Committee

Srinivas Tadigadapa
Professor of Electrical Engineering

Shizhuo Yin
Professor of Electrical Engineering

Ralph H. Colby
Professor of Materials Science and Engineering

Kultegin Aydin
Professor of Electrical Engineering
Interim Head of Department of Electrical Engineering

*Signatures are on file in the Graduate School

ABSTRACT

In the past decades, ionic electroactive polymers (*i*-EAPs) have become attractive transduction materials due to their relatively large electromechanical actuations that can be generated under low voltages (~ a few volts) and many other advantages, such as flexibility and light weight. These *i*-EAP actuators hold promises for applications including artificial muscles, robots, micro-electromechanical systems (MEMS), nano-electromechanical systems (NEMS), and energy harvesting. On the other hand, one critical issue in utilizing *i*-EAPs for those applications is how to significantly improve the electromechanical performance, including the actuation speed, actuation strain level and efficiency. Particularly, extremely low efficiency is the major drawback of current *i*-EAP actuators.

This dissertation discusses the physics in ionic polymer composite actuators and develops solutions to improve the actuation strain, speed, and efficiency. One general approach through the entire dissertation is to electrically and electromechanically analyze ionic polymer composite actuators to identify the limiting factors, and design a strategy to guide material selection or device fabrication for better performance.

Two types of ionic polymer actuators will be discussed: (i) ionic polymer conductive network composite (IPCNC) actuators that consist of an ionic liquid (IL) containing polymer membrane and large surface area composite electrodes, referred to as the “IPCNC actuator”; and (ii) IL containing ionic polymer membranes with planar Au electrodes, referred to as the “ionic polymer membrane actuator”. While the composite electrodes in the IPCNCs provide large specific capacitance for ion storage which enhances the bending actuation, the ionic polymer membrane actuators offer a simple structure for device modeling and material analysis.

IPCNC actuators are fabricated and discussed first. IPCNCs with disordered CNC nanomorphology (nanoscale morphology), mostly made with conducting nanoparticles, are discussed in Chapter 3, while IPCNCs with ordered CNC nanomorphology, in which vertically aligned carbon nanotubes (VA-CNTs) are implemented, are discussed in Chapter 4. In these chapters, electrical and electromechanical models are established to analyze the performance of IPCNC actuators.

Firstly, electronic equivalent circuits are developed to model the complex frequency-dependent impedance and explain the initial response ($t < 10$ s) of ionic polymer composite actuators. It is found that the low frequency responses of these actuators indicate Warburg diffusion (semi-finite diffusion). When there is no CNC or when CNC is very thin (tens of nm), a simple equivalent circuit, which only consists of Warburg impedance A_w , bulk resistance R , and electric double layer capacitance C_{dl} can be used, where C_{dl} and A_w dominate the fast and slow responses of the actuator, respectively. When the CNC is thick (several μm), the aforementioned equivalent circuit is no longer adequate; therefore, the de Levi transmission line is introduced to model the CNC layer, which shows that the device transport time constant increases with CNC thickness. Secondly, by combining the time domain electric and electromechanical responses, a two-carrier model is established to explain the long time actuation response ($t > 10$ s), and also provide quantitative information on transport behavior of the two mobile ions (i.e., cation and anion) in IPCNCs. By employing this model, the total excess ions stored and strains generated by the cations and anions, and their transport times in the nanocomposites can be determined, which all depend critically on the morphologies of the conductor network nanocomposites. The model further reveals that, for EMI-Tf or EMI-BF₄, anions have a larger effective ion size than cations, and thus dominate the long time response ($t > 10$ s) of the ionic polymer actuators, while cations account for the initial response ($t < 10$ s) of the actuators. Finally, IPCNCs with high volume

fraction VA-CNTs are fabricated to improve the electromechanical performance of IPCNC actuators. The results demonstrate that the VA-CNTs create non-isotropic elastic modulus in the composite electrodes which markedly enhance the actuation strain (8.2%) compared to that of IPCNCs with RuO_2 nanoparticles (2.1%), and provide inter-VA-CNT ion channels that enable faster actuation ($\tau=0.82$ s) than that of IPCNCs with RuO_2 nanoparticles ($\tau=3$ s).

Besides studies on IPCNC actuators, two other studies are performed on ionic polymer membrane actuators to understand the physics of ions transport in ionic liquid electrolytes and ion-polymer interaction, which are difficult to be tackled by directly studying the complex IPCNC actuators.

Electrically, the ion distribution of the electrical double layer and the diffuse layer, which has been extensively analyzed with equivalent circuits, is of great interest. Hence, direct observations of the ion distribution in ionic polymer membrane actuator with 1-butyl-2,3-dimethylimidazolium chloride (BMMI-Cl) electrolyte are performed by employing Time-of-Flight Secondary Ion Mass Spectrometry (ToF-SIMS). The results reveal that Cl^- and BMMI^+ accumulate near both cathode and anode due to a strong Coulomb force between the ions and the ion size difference (17 times) causes the BMMI^+ space charge layers (~ 6 μm) to be much thicker than those of Cl^- (~ 0.5 μm). These findings emphasize the importance of engineering the electrolyte for IPCNC actuators, as well as show the dominance of large ions on the long time actuation response.

At last, progress in addressing the electromechanical coupling between the ions and the electroactive polymers, is made by applying P(VDF-CTFE), crosslinked P(VDF-CTFE)/PMMA, and crosslinked P(VDF-TrFE-CFE) for ionic polymer membrane actuators. Compared to the conventional ionic polymers, such as Nafion and Aquivion ionomers that were popularly utilized in previous IPCNC actuator studies, these PVDF based polymers remarkably enhance the stress

generation and significantly depress the charge consumption of the ionic polymer membrane actuators, both of which leads to higher energy conversion efficiency.

TABLE OF CONTENTS

LIST OF FIGURES	x
LIST OF TABLES.....	xviii
ACKNOWLEDGEMENTS.....	xix
Chapter 1 Introduction	1
1.1 Introduction.....	1
1.1.1 Ionic electroactive polymers (<i>i</i> -EAP) actuators.....	2
1.1.2 Ionic Polymer Metal Composite (IPMC) and Ionic Polymer Conductor Network Composite (IPCNC)	3
1.2 Main Components of IPCNC Actuators	6
1.2.1 Ionomers/ionic polymers.....	6
1.2.2 Ionic liquids.....	7
1.2.3 Conductor network composite (CNC).....	8
1.3 Research Contribution and Dissertation Organization.....	9
Chapter 2 Electrical and Mechanical Characterization Methods.....	11
2.1 List of Symbols	11
2.2 Characterization Setups.....	12
2.2.1 Electrical characterization setups	12
2.2.2 Mechanical characterization setups.....	14
2.2.3 Electromechanical characterization setups.....	16
2.2.4 Chemical characterization setups (Secondary Ion Mass Spectroscopy)	18
2.3 Properties and Models of Ionic Polymer Actuators	20
2.3.1 Mechanical properties	20
2.3.1.1 <i>Intrinsic stress and strain in a bimorph actuator</i>	21
2.3.1.2 <i>Intrinsic stress and strain in an IPCNC actuator</i>	23
2.3.1.3 <i>Elastic modulus</i>	25
2.3.1.4 <i>Mechanical energy and electromechanical efficiency</i>	27
2.3.2 Electrical properties and models	28
2.3.2.1 <i>Electrical impedance and equivalent circuits</i>	28
2.3.2.2 <i>Electrical double layer theories and ionic conductivity</i>	31
2.3.2.3 <i>Electrode polarization (EP) model</i>	34
2.3.2.4 <i>Potentiostatic method</i>	38
Chapter 3 IPCNC Actuators with Disordered CNC Nanomorphology	42
3.1 Introduction.....	42
3.1.1 Actuation magnitude and speed	42
3.2 IPCNC Fabrication and Characterization.....	45
3.2.1 Layer-by-layer (LbL) self assembled CNCs	46
3.2.2 Direct assembly process (DAP) CNCs.....	47

3.2.3 Actuator fabrication and characterization	49
3.3 Results and Discussion.....	50
3.3.1 Equivalent circuit modeling and analysis.....	50
3.3.1.1 <i>The ionomer membrane actuator</i>	53
3.3.1.2 <i>The IPCNC actuator via LbL self assembly</i>	55
3.3.1.3 <i>The IPCNC actuator via DAP</i>	56
3.3.2 Electro-mechanical modeling (2-carrier model)	59
3.4 Conclusion	67
Chapter 4 IPCNC Actuators with Ordered CNC Nanomorphology	69
4.1 Introduction.....	69
4.1.1 Introduction to CNT	69
4.1.2 Benefits of utilizing VA-CNTs	71
4.1.2 Anisotropic mechanical properties in VA-CNTs	74
4.2 Actuator Fabrication	75
4.2.1 CNT forest.....	75
4.2.2 VA-CNT actuator fabrication.....	77
4.2.3 RuO ₂ actuator fabrication.....	78
4.3 Results and Discussions	79
4.3.1 Electrical properties.....	79
4.3.2 Mechanical properties	80
4.3.3 Bending actuation.....	82
4.3.4 Impedance modeling and analysis.....	84
4.4 Conclusion	88
Chapter 5 Ion Distribution in Ionic Polymer Membrane Actuators.....	89
5.1 Introduction.....	89
5.2 Characterization of <i>i</i> -EAP Membrane Actuators	92
5.2.1 Sample preparation and characterization methods	92
5.2.2 ToF-SIMS	93
5.3 Results and Discussions	95
5.3.1 Electrical and electromechanical characterizations.....	95
5.3.2 Secondary ion mass spectroscopy (SIMS) spectra.....	99
5.3.3 Depth profile	100
5.3.3.1 <i>Ion aggregation</i>	104
5.3.3.2 <i>Asymmetry of ions</i>	109
5.5 Conclusion	111
Chapter 6 Polymer in Ionic Polymer Actuators	112
6.1 Introduction.....	112
6.2 Polymer Materials Fabrication	116
6.2.1 P(VDF-CTFE).....	116
6.2.2 Crosslinked P(VDF-CTFE)/PMMA.....	116
6.2.3 Crosslinked P(VDF-TrFE-CFE) terpolymer	117
6.2.4 CNCs with P(VDF-CTFE)/PMMA and RuO ₂ nanoparticles	118

6.2.5 Actuator fabrication and characterization	118
6.3 Results and Discussions	119
6.3.1 Mechanical properties	119
6.3.2 Electrical properties.....	123
6.3.3 Electromechanical coupling	126
6.3.3.1 <i>Bending actuation</i>	126
6.3.3.2 <i>Stress charge ratio</i>	127
6.3.3.3 <i>Energy Efficiency under direct current (DC) stimulus</i>	130
6.3.3.4 <i>Energy efficiency under alternating current (AC) stimulus</i>	133
6.3.3.5 <i>P(VDF-CTFE)/PMMA CNC</i>	134
Chapter 7 Conclusion and Future Work	138
7.1 Conclusion	138
7.2 Future Work	141
Appendix A: Derivation of Equation (2.6) and (2.12)	145
Appendix B: Gouy-Chapman Solution of Poisson-Boltzmann Equation	147
Appendix C: Derivation of Warburg Impedance	149
References.....	151
VITA	

LIST OF FIGURES

Figure 1-1: Photo and schematic from the 2005 EAP/Human Armwrestling Match. Also, a video of the competition is available on the Discovery channel's Daily Planet, March 15, 2005.[5].....	1
Figure 1-2: (a) The actuation of IPMC (or IPCNC) actuator (b) The IPMC (or IPCNC) actuator bending mechanism.....	3
Figure 1-3: (a) Schematic of cross-section of IPMC fabricated using chemical reduction method. (b) SEM image of porous Pt electrode near IPMC surface.[15].	4
Figure 1-4: Schematic of the cross-section of an IPCNC actuator.	6
Figure 1-5: Time history of the tip displacement of a Nafion actuator sample in the water and ionic liquid (EMI-Tf) forms. [22].....	7
Figure 2-1: Photo of Princeton Applied Research PARSTAT 2273 Potentiostat.....	13
Figure 2-2: Photo of Lecroy wavesurfer 42Xs-A Oscilloscope.....	13
Figure 2-3: Photo of TA DMA 2980 Dynamic mechanical analyzer with a liquid N ₂ Cooling unit.....	14
Figure 2-4: Schematic of modulus measurement set-up for ultra-soft materials.	15
Figure 2-5: Photo of modulus measurement set-up for ultra-soft materials.....	16
Figure 2-6: Schematic of bending actuation measurement set-up.	17
Figure 2-7: Photo of bending actuation measurement set-up.....	17
Figure 2-8: Schematics of secondary ion sputtering [32].	18
Figure 2-9: Components of SIMS [32].	18
Figure 2-10: ToF-SIMS located in Winograd Lab at Penn State.....	19
Figure 2-11: Mechanical schematic of a bimorph actuator.....	22
Figure 2-12: Mechanical schematic of an IPCNC actuator.....	24
Figure 2-13: Schematic of a bi-layer laminate for the characterization of the elastic modulus of individual layers.....	25
Figure 2-14: Nyquist plot of complex impedance.....	29

Figure 2-15: The complex plane representation of a simple electrostatic double layer, and a double layer with leakage resistance.	30
Figure 2-16: The complex plane representation of a pseudo-capacitor and a pseudo-capacitor with leakage resistance.	30
Figure 2-17: Electric double layer models for dilute solution. (a) Helmholtz model, (b) Gouy-Chapman, (c) Stern, and (d) Bockris, Devanathan, and Muller (BDM) model. [60]	31
Figure 2-18: Equivalent circuit of an ionic polymer membrane actuator.	32
Figure 2-19: The electrical double layer capacitance and bulk ionic resistance of an ionic polymer membrane actuator.....	33
Figure 2-20: Schematic of charge density distribution under a dc parallel-plate field. [49].	35
Figure 2-21: Schematic plot of the EP relaxation in ϵ' , ϵ'' , and $\tan \delta$ for a conductive system, with peak frequencies, dielectric relaxation strength, and ϵ_R denoted.[48].....	36
Figure 2-22: Schematics of an <i>i</i> -EAP membrane sandwiched between metal electrodes under an applied voltage. When the voltage rises from zero to V_0 , ions drift and diffuse towards the electrodes with opposite polarity.....	38
Figure 3-1: Bending curvatures of 25 μm Nafion with 0-80 nm PAH/Au CNCs that are fabricated via LbL method. Curvature increases linearly with the thickness of CNC. Data are taken under application of 4 V step function. (Redrawn from reference [58]).....	43
Figure 3-2: Bending curvatures (short time) of 50 μm Nafion with 0-13 μm Nafion/RuO ₂ CNCs that are fabricated via DAP method. Data are taken under application of 4 V step function (Collaboration with Francis Richey at Drexel University).	43
Figure 3-3: Bending Actuation (long time) of 50 μm Nafion with 0-13 μm Nafion/ RuO ₂ CNCs that are fabricated via DAP method. Data are taken under application of 4 V step function (Collaboration with Francis Richey at Drexel University).....	44
Figure 3-4: The actuator response as a function of time under a step voltage for 25 μm Nafion with 400 nm PAH/Au CNCs and 25 μm Nafion with 3 μm Nafion/RuO ₂ CNCs. [17].	45
Figure 3-5: Schematic of the layer-by-layer assembly deposition process using slides and beakers. Steps 1 and 3 represent the adsorption of a polyanion and polycation, respectively, and steps 2 and 4 are washing steps. The four steps are the basic buildup sequence for the simplest film architecture. [60].	46
Figure 3-6: SEM of the PAH/Au CNC studied in this chapter.	47

Figure 3-7: Schematic showing the four steps Direct Assembly Process (DAP) for building dry transducers[16].	48
Figure 3-8: SEM of the Nafion/RuO ₂ CNC served in this chapter.	48
Figure 3-9: Chemical formulae of the ILs 1-ethyl-3-methylimidazolium trifluoromethanesulfonate (EMI-Tf) and 1-ethyl-3-methylimidazolium tetrafluoroborate (EMI-BF ₄) that were utilized in this dissertation.	49
Figure 3-10: Bending actuations of Nafion and Nafion with LBL PAH/Au IPCNC actuator.	51
Figure 3-11: (a) RC equivalent circuit and (b) Equivalent Circuit with Warburg element.	52
Figure 3-12: (a) Impedance magnitude and (b) Phase of Nafion with 40 wt% EMI-Tf fitted by simple RC circuit and Equivalent Circuit with Warburg element.	53
Figure 3-13: Nyquist Plot of Nafion with 40 wt% EMI-Tf.	54
Figure 3-14: (a) Impedance magnitude and (b) phase of Nafion with 64 nm LbL PAH/Au composite actuator (contain 40 wt% of EMI-Tf).	55
Figure 3-15: (a) Impedance magnitude and (b) phase of Nafion with 6 μ m DAP Nafion/RuO ₂ composite actuator (contain 40 wt% of EMI-Tf).	57
Figure 3-16: Schematic for a transmission line model of the de Levie impedance.	57
Figure 3-17: Schematic for equivalent circuits with de Levie transmission line for different CNC thickness.	58
Figure 3-18: Bending actuation recorded at different times ($t_2 > t_1$) for the PAH/Au IPCNCs under 4V step voltage.	59
Figure 3-19: Bending actuations of (a) Nafion and Aquivion with ionic liquids EMI-Tf and (b) Nafion with BMI and Propylene Carbonate.	60
Figure 3-20: Data and fitting of charge and curvature vs. time for Nafion with 3 μ m thick Nafion/RuO ₂ composite electrodes at each side and EMI-BF ₄ IL under 3V step voltage.	60
Figure 3-21: Data and fitting of charge and curvature vs. time for Nafion with 3 μ m thick Nafion/RuO ₂ composite electrodes at each side and EMI-BF ₄ IL under 3V step voltage.	61
Figure 3-22: Data and fitting of charge and curvature vs. time for Nafion with 180 nm PAH/Au LbL composite electrodes and EMI-Tf IL under 4V step voltage.	61
Figure 3-23: Data and fitting of charge and curvature vs. time for curvature for Nafion with 400 nm PAH/CNT LbL composite and EMI-Tf IL under 4V step voltage.	61

Figure 3-24: Equivalent circuit with two carrier currents.....	62
Figure 3-25: Schematic diagram of strain cancellation effect in electrodes.	63
Figure 3-26: Cation, anion and device electromechanical energy efficiency of CNC1: Nafion with 3 μm thick Nafion/RuO ₂ composite electrodes at each side and EMIBF ₄ IL under 3V step voltage, CNC2: Aquivion with 3 μm Aquivion/RuO ₂ composite electrodes and EMITf IL under 3V step voltage, CNC3: Nafion with 180 nm PAH/Au LbL composite electrodes and EMITf IL under 4V step voltage, and CNC4: Nafion with 400 nm PAH/CNT LbL composite and EMITf IL under 4V step voltage.	66
Figure 4-1: Schematic of how to "roll up" a graphene sheet to make the nanotube. T denotes the tube axis, and a_1 and a_2 are the unit vectors of graphene in real space. [90].	70
Figure 4-2: (a) Schematic diagram of the collapse of the aligned low-density as-grown forest (above) to the highly densely packed SWNT solid (below). (b) Overlaid pictures illustrating the decrease in lateral dimensions before (grey) and after (black) collapse. (c) Schematic model comparing the ion diffusion for activated carbon and the SWNT solid material. (d) Change in the capacitance per volume using the SWNT solid sheet (red) and as-grown forest (black). (e) Capacitance versus discharge current density comparing SWNT solid (red) and activated carbon (blue) for 0.1 and 0.5mm electrode thicknesses (dashed and solid lines, respectively).[87].....	71
Figure 4-3: (left) Tortuous ion transport paths in nanoparticle/Nafion CNCs, where black dots are conductive nanoparticles. (right) Aligned ion transport channels in VA-CNT/Nafion CNCs.....	72
Figure 4-4: Schematic drawing of (a) a CNC/ionomer/CNC three layers bimorph actuator with VA-CNTs in the CNC layers (no voltage applied), (b) a bended actuator with excess ions on cathode side with voltage applied (z axis is in the thickness direction and x axis along length direction, i.e. actuation direction. In the actuator, the mobile ions are assumed to be cations.)	73
Figure 4-5: Schematic of vertically aligned CNT growth process: pretreatment of catalyst on substrate (metal film de-wetting into nanoclusters), nucleation of CNTs on the catalyst particles, and growth (Courtesy of Hulya Cebeci at MIT).....	74
Figure 4-6: (a) schematic of densification of variable volume fraction aligned-CNTs (b) Optical image of aligned CNT volume fraction from mechanical densification of 1mm tall A-CNT forests at 1% (as-grown), 8% (uniaxially densified), and 20% (biaxially densified) volume fraction. [97].	75
Figure 4-7: SEM images of (e) 1% Vf CNT forest as grown, and (f) 10% Vf CNT forest after densification.....	76

Figure 4-8: SEM images of (a) failure example due to fast solvent evaporation and (b) success example of Nafion/VA-CNT composite with CNT array in thickness (z) direction	77
Figure 4-9: SEM images of (a) as-made Nafion/VA-CNT actuator and (b) interface region, showing aligned CNTs in CNC layer.	78
Figure 4-10: Nyquist plots of IPCNCs: Nafion with 12 μm Naifon/VA-CNT CNC and Nafion with 12 μm Naifon/RuO ₂ CNC. All IPCNCs contains 40 wt% of EMI-Tf.	80
Figure 4-11: Strains generated from the absorption of ILs in the pure Nafion and Nafion/VA-CNT composite under same conditions	81
Figure 4-12: Bending curvature of Nafion/VA-CNT and Nafion/RuO ₂ composite actuators under 4 volts. Time constants are obtained by fitting the curvature data with exponential functions.	82
Figure 4-13: Strains and time constants of Nafion with 12 μm Nafion/VA-CNTs and Nafion with 12 μm Nafion/RuO ₂ composite actuators. Both actuators have 40 wt% uptake of EMI-Tf as electrolytes.....	83
Figure 4-14: Simplified equivalent circuits for IPCNC actuators.....	84
Figure 4-15: Data and fitting of bold impedance.	85
Figure 4-16: Data and fittings of phase.....	85
Figure 5-1: (a) An ionic polymer bending actuator under electric signal and (b) schematic of actuation mechanism.....	88
Figure 5-2: Operation mechanism of ToF-SIMS in this dissertation.....	91
Figure 5-3: (a) Schematic of device configuration and (b) molecular structure of BMMI-Cl and (c) EMI-Tf studied.....	92
Figure 5-4: (a) Nyquist Plot of Aquivion with BMMI-Cl at 25 $^{\circ}\text{C}$ and 105 $^{\circ}\text{C}$, compared to Aquivion with EMI-Tf at 25 $^{\circ}\text{C}$. (b) Charge versus time of Aquivion with BMMI-Cl at 25 $^{\circ}\text{C}$ and 105 $^{\circ}\text{C}$ under 2.5V.....	96
Figure 5-5: Linear Sweep Voltammetry of Aquivion with BMMI-Cl at 105 $^{\circ}\text{C}$ under AC stimulus.....	97
Figure 5-6: Image of bending magnitude of Aquivion with BMMI-Cl at 105 $^{\circ}\text{C}$ under AC stimulus.....	98
Figure 5-7: Time-resolved actuation of Aquivion with BMMI-Cl at 105 $^{\circ}\text{C}$ under AC stimulus.	98
Figure 5-8: Mass spectra of (a) positive ions and (b) negative ions	99

Figure 5-9: Control signal of Aquivion with 45 wt% BMMI-Cl ionic liquids (a) F^- and Cl^- (b) CF^+ and $BMMI^+$ without electrical bias.....	101
Figure 5-10: Cation distribution normalized by its middle region Counts (thickness is $0\mu m$ at cathode; thickness is $27\mu m$ at anode).	102
Figure 5-11: Anion distribution normalized by its middle region counts (thickness is $0\mu m$ at cathode; thickness is $27\mu m$ at anode).	102
Figure 5-12: Depth profile of polymer fragments under charged condition (2.5V).....	103
Figure 5-13: Voltage-dependent double-layer structure predicted by Bazant et al. Dimensionless cation (solid curve) and anion (dashed curve) concentrations and mass density (dash-dotted curve) at high voltage $\tilde{V} = eV / kT$. ($V=2.6V$ when $\tilde{V}=100$) Position x is measured from the distance of closest approach and scaled to the ion diameter $a=10\text{\AA}$. Model parameters $\gamma = 0.5$, which is the ratio of the bulk ion density to the maximum possible density, electrostatic correlation length $\delta_c = l_c / \lambda_D = 10$, and $\varepsilon = 5\varepsilon_0$ are those fitting ion profiles in simulations [99]......	105
Figure 5-14: Capacitance of Aquivion with 40 wt% EMI-Tf at different voltage and different time scale. (unpublished data from MURI ILEAD presentation by Zhang and Colby).....	107
Figure 5-15: Schematic diagram of ion distribution in ILs near a charged planar surface	107
Figure 5-16: One snapshot of BMI- NO_3 with 1000 ion pairs at $T=700\text{ K}$ with (a) tail groups only, (b) head groups only, and (c) anions only.[113].	109
Figure 5-17: Estimation of relative ion concentration.	110
Figure 6-1: The molecular structure of Nafion; (b) the cluster network morphology model by Gierke et al.[20].	113
Figure 6-2: Schematics of perfluorosulfonate ionomers and P(VDF-CTFE) with an extra ion.	114
Figure 6-3: Composition of ionic polymer membrane actuator.....	115
Figure 6-4: Chemical formula of (a) P(VDF-CTFE), (b) PMMA, and (c) P(VDF-TrFE-CTFE).	115
Figure 6-5: DMA curve of P(VDF-CTFE), P(VDF-CTFE)/PMMA blends (without initiator), and P(VDF-CTFE)/PMMA with initiator.	121
Figure 6-6: DSC curve of P(VDF-CTFE)/PMMA blends (without initiator) and P(VDF-CTFE)/PMMA with initiator.....	121

Figure 6-7: DMA curve of P(VDF-TrFE-CFE) without and with initiator and crosslink agent.....	122
Figure 6-8: DSC curve of P(VDF-TrFE-CFE) without and with initiator and crosslink agent.....	122
Figure 6-9: Frequency-dependent conductivity of the five types of ionic polymer membrane actuators with 40 wt% EMI-Tf under a 4 V step voltage.....	124
Figure 6-10: Charge density of the five types of i-EAP membrane actuators with 40 wt% EMI-Tf under a 4 V step voltage.	125
Figure 6-11: Bending curvature of the five types of ionic polymer membrane actuators with 40 wt% EMI-Tf under a 4 V step voltage.	126
Figure 6-12: Schematic of a bimorph bending actuator with a 3-layer structure and a conceptual diagram of the microscopic interaction between ionic liquids and the polymer matrix.....	128
Figure 6-13: Stress charge ratio of the five types of ionic polymer membrane actuators with 40 wt% EMI-Tf under a 4 V step voltage.	129
Figure 6-14: Areal mechanical energy of the five types of i-EAP membrane actuators with 40 wt% EMI-Tf under a 4 V step voltage.	131
Figure 6-15: Device energy efficiency of the five types of ionic polymer membrane actuators with 40 wt% EMI-Tf under a 4 V step voltage.....	132
Figure 6-16 Time-dependent diagram of the bending actuation of P(VDF-CTFE) membrane actuator under 4 V 0.1Hz triangle wave.....	133
Figure 6-17: Comparison of peak-to-peak bending magnitude and peak-to-peak current consumption of five types of ionic polymer membrane actuators driven by 4V 0.1 Hz triangle stimulus.	134
Figure 6-18: Bending curvature of two actuators with 40 wt% EMI-Tf under a 4 V step voltage, including P(VDF-CTFE)/PMMA and P(VDF-CTFE)/PMMA with CNC. CNC is made of P(VDF-CTFE)/PMMA with 40 vol% of RuO ₂	135
Figure 6-19: Normalized curves of two actuators with 40 wt% EMI-Tf under a 4 V step voltage, including P(VDF-CTFE)/PMMA and P(VDF-CTFE)/PMMA with CNC. CNC is made of P(VDF-CTFE)/PMMA with 40 vol% of RuO ₂	135
Figure 6-20: Energy conversion efficiency of two actuators with 40 wt% EMI-Tf under a 4 V step voltage, including P(VDF-CTFE)/PMMA and P(VDF-CTFE)/PMMA with CNC. CNC is made of P(VDF-CTFE)/PMMA with 40 vol% of RuO ₂	136
Figure 7-1: Capacitance and voltage drop near two charged electrodes.....	143

Figure 7-2: SEM image of aligned graphene sheets. [130].....	144
---	-----

LIST OF TABLES

Table 1-1: List of EAP materials [4]	2
Table 2-1: List of symbols and their meanings	11
Table 3-1: Properties of the ILs that were utilized in this chapter	48
Table 3-2: Summary of dimensions of Nafion membrane actuator and LbL actuator	50
Table 3-3: Fitting parameters for ionic polymer actuators	55
Table 3-4: Summary of fitting parameters for the IPCNCs discussed	62
Table 3-5: Diffusion coefficients (measured) and electrophoretic mobilities (calculated) from pulsed-gradient NMR for the ILs studied	63
Table 3-6: Ion size estimation [67]	64
Table 3-7: Young's modulus of each layer in IPCNCs [67]	64
Table 4-1: List of through plan conductivity of CNT forests, VA-CNT CNC, and RuO ₂ CNC	79
Table 4-2: Fitting parameters for Nafion membrane (from Chapter 3) and IPCNC actuators	86
Table 5-1: Sputter rate calculated from multiple sputtering craters	100
Table 5-2: Roughness test results of Aquivion membrane with 45 wt% of BMMI-Cl	103
Table 6-1: Moduli of polymers without and with 40 wt% of EMI-Tf uptake	118

ACKNOWLEDGEMENTS

I would like to first express my sincere gratitude to my advisor Professor Qiming Zhang for years of support. I am extremely fortunate to have an advisor who gave me both the freedom to explore on my own and guidance on how to tackle difficult research problems. His insights into this area led my dissertation to a level which I was incapable to achieve on my own.

I gratefully acknowledge my committee members Professor Srinivas Tadigadapa, Professor Shizhuo Yin, and Professor Ralph H. Colby. They have spent a lot of their precious time on reading my thesis, making constructive comments and advancing critical suggestions in my research process, and setting great examples of being a mature and serious researcher for me.

I sincerely thank all my colleagues, especially Dr. Minren Lin for his uncanny ability to help with nearly everything, Dr. Sheng Liu for being a fun and insightful research partner, Mr. Mehdi Ghaffari, Dr. Junhong Lin, Mr. Gokhan Hatipoglu, Ms. Ran Zhao, Dr. Jiping Cheng, Mr. Yue Zhou and my fellow students for their assistance and friendship during my PhD study.

Furthermore, I would like to thank my collaborators: Professor Ralph H. Colby at Penn State, Professor James R. Heflin at Virginia Tech, Professor Brian L. Wardle at MIT, Professor Nicholas Winograd at Penn State, Professor Yossef A. Elabd at Drexel, Professor Louis Madsen at Virginia Tech, Professor Chun Liu at Penn State, and their group members. Some of their group members I closely worked with are Dr. Caiyan Lu, Dr. Wenjuan Liu, Dr. Gregory Tudryn, Mr. U Hyeok Choi, Dr. Shih-Wa Wang, Mr. Siwei Liang, Mr. Francis Richey, Mr. Jianbo Hou, Dr. Jing Li, Dr. Vaibhav Jain, Dr. Reza Montazami, Mr. Dong Wang, Ms. Hülya Cebeci, and Dr. Roberto Guzmán de Villoria.

During my four year PhD study, research/career discussions with many lecturers at Penn State were very inspiring and helpful. I would like to give my acknowledgment to Prof. Thomas N. Jackson, Prof. Jerzy Ruzyllo and Professor Srinivas Tadigadapa.

I also would like to thank all the co-workers during my internship at Intel Corporation, especially Dr. Donald S. Gardner, Dr. Cary L. Pint and Dr. Zhaohui Chen for their kind guidance and help.

Special thanks go to my husband Kai Zhang, my parents Dawei Liu and Shunqin Yang, my parents in law Zuolong Zhang and Lihua Wang for their love throughout my many years of education.

The financial support of this research was provided by U.S. Army Research Office under Grant No. W911NF-07-1-0452 Ionic Liquids in Electro-Active Devices (ILEAD) MURI, NIH under Grant No. R01-EY018387-02, and NSF under grant (NIRT) No. CMMI 0709333.

Chapter 1

Introduction

1.1 Introduction

Electroactive polymers (EAPs) are polymers that exhibit a change in shape when stimulated by an electric field. As early as the 1880s, researchers had discovered a few types of polymers which can be regarded as EAPs, but the induced strain was relatively small.[1] Since the early 1990s, significant strain levels were generated from various EAPs [2-9] that EAPs started to attract a great attention of engineers and scientists from multiple disciplines. As polymers, EAPs can be easily engineered into various shapes so that they can potentially be integrated into micro-electro-mechanical-systems (MEMS) or microfluidic devices.[10-13] Since EAPs can be applied to mimic the movements of humans, animals, and insects, they are also attractive in the biomimetics field.[14-17] Hence, EAPs are often referred to as artificial muscles, and armwrestling matches between EAP actuated robotic arms and humans have been hold by NASA since 2005.[18]

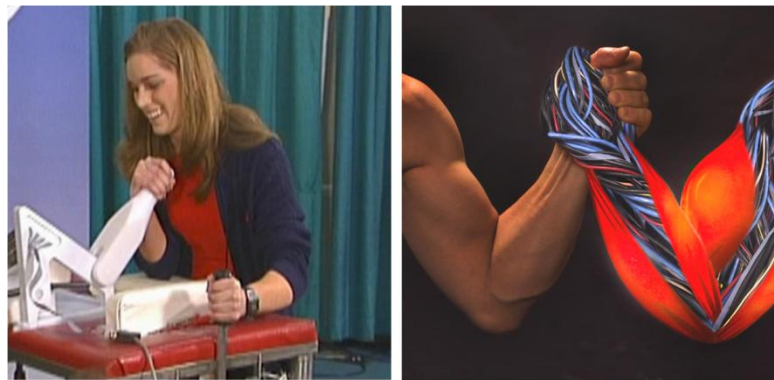


Figure 1-1 Photo and schematic from the 2005 EAP/Human Armwrestling Match. Also, a video of the competition is available on the Discovery channel's Daily Planet, March 15, 2005.[18]

1.1.1 Ionic electroactive polymers (*i*-EAP) actuators

According to the actuation mechanism, EAP can be divided into two categories: electronic EAP (or field activated EAP) and ionic EAP (*i*-EAP), [14] as shown in Table 1-1.

Table 1-1 List of EAP materials[9]

Electronic EAP	Ionic EAP (<i>i</i> -EAP)
Dielectric EAP	Ionic Polymer Metal Composite (IPMC)
Electrostrictive Graft Elastomers	Ionic Polymer Gels (IPG)
Electrostrictive Polymers	Carbon Nanotubes (CNT)
Electro-Viscoelastic Elastomers	Conductive Polymers (CP)
Ferroelectric Polymers	ElectroRheological Fluids (ERF)
Liquid Crystal Elastomers (LCE)	

The electronic EAPs are driven by Coulomb force and have a larger mechanical energy density than *i*-EAPs. Since they can hold the induced displacement under a DC voltage, electronic EAPs can be used for robotic application. However, a large strain generation of electronic EAPs usually requires a high activation field ($>100 \text{ V}/\mu\text{m}$) that may be close to their breakdown limit and may cause safety issues. In contrast, *i*-EAPs can usually be operated by as low as 2 or 3 volts and they generate a significant bending displacement. *i*-EAPs consist of two electrodes and electrolyte and they are driven by the drift and/or diffusion of ions in the electrolyte. The disadvantages of *i*-EAPs are their low energy conversion efficiency and their difficulty to sustain constant displacement under activation of a DC voltage (except for conductive polymers).

As shown in Table 1-1, leading examples of *i*-EAPs include ionic polymer-metal composites (IPMC),[15, 19] ionic polymer gels (IPG),[20] conductive polymers (CP),[10, 21, 22] carbon nanotubes (CNT),[23] and electrorheological fluids (ERF).[24] In this dissertation, new progresses in IPMC will be presented and a more general term “ionic polymer conductor network composite (IPCNC)” is used as a new term to distinguish with the traditional term of ionic

polymer metal composite (IPMC) since recent years, non-metal conductors are also used to make composites, instead of the more usual metal conductors.

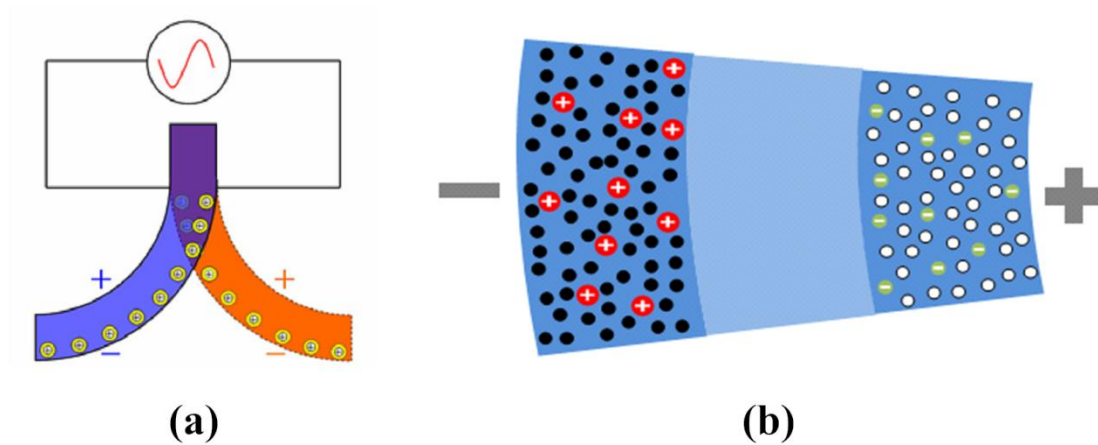


Figure 1-2. (a) The actuation of IPMC (or IPCNC) actuator (b) The IPMC (or IPCNC) actuator bending mechanism

The actuation mechanism of a typical IPMC (or IPCNC) actuator is shown in Figure 1-2. Under applied electrical field, the cations and anions drift into cathode and anode, respectively, therefore, swell the electrode regions and cause bending of the actuator if the sizes of cation and anion are different, and in most cases, $\text{cation} > \text{anion}$. The bending response is affected by many factors, such as device structure, accessible electrode surface area, elastic moduli of the materials, ionic conductivity of the electrolyte, etc.

1.1.2 Ionic Polymer Metal Composite (IPMC) and Ionic Polymer Conductor Network Composite (IPCNC)

IPMC was first fabricated and reported in 1992 by Oguro.[3] After several improvements, porous metal electrode was used as metal composite electrodes by a chemical reduction process. The most commonly used IPMCs are made by chemically reducing precious metals onto Nafion

membrane surfaces, which is a type of perfluoro-sulfonated ionomer membrane. In the reduction process, metal nanoparticles penetrate through the Nafion surface to form porous electrodes. The chemical reduction of Pt and Au onto a Nafion surface is presented as follows[25]:

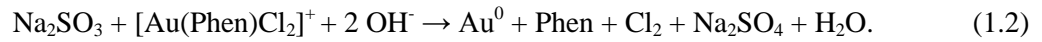
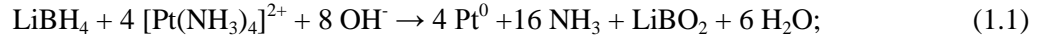


Figure 1-3 shows the schematic and Scanning Electron Microscope (SEM) of Pt on Nafion surfaces. This previous IPMC with porous metal electrodes provided extended surface area for ion polarization, and thus led to improved actuation levels. However, this fabrication method suffers from low rate of fabrication, poor control of thickness, and unpredictable composite morphology. It is found that the ion channels which initially transport the precious metal salts into the membrane are usually blocked by the reduced metal, leading to small strain and low actuation speed.

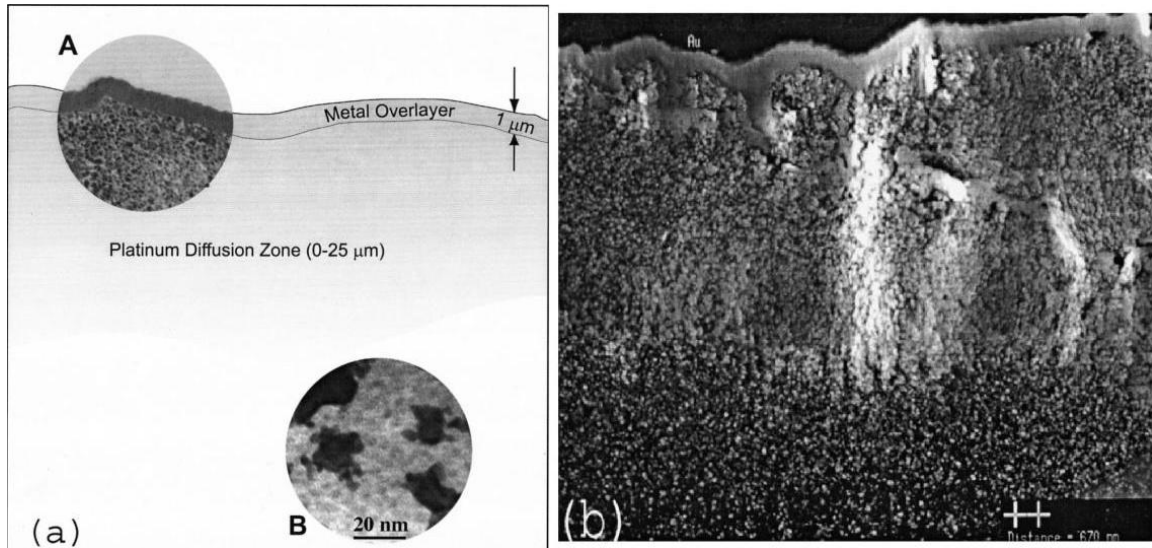


Figure 1-3 (a) Schematic of cross-section of IPMC fabricated using chemical reduction method. (b) SEM image of porous Pt electrode near IPMC surface.[26]

In 2007, Akle and Leo developed a direct assembly process to fabricate porous electrode composites in which conductor nano-particles were mixed with a solution of Nafion, and then

directly deposited onto a piece of Nafion membrane, which served as the substrate.[27] This direct assembly method to fabricate IPMC drew great attention immediately, because it allowed the utilization of various nano-size conductors including RuO₂ nanoparticles, carbon nanotubes, and graphene sheets. It also significantly simplified the fabrication process, achieved controlled composition and morphology, improved actuator performance, and enhanced reproducibility. [27] Therefore, to distinguish the new composite from traditional “metal composite”, ionic polymer conductor network composite (IPCNC) is introduced as the name of *i*-EAPs with composites made of ionic polymer and conductor fillers, which may or may not contain metals.

In 2009, another well controlled conductor network composite (CNC) fabrication method, layer-by-layer self assembly, was introduced by Liu, Montazami, and Heflin.[28] Layer-by-layer (LbL) films, also referred to as ionic self-assembled multilayer (ISAM) films,[29] allow to control structure and thickness at the molecular level. The fabrication process of LbL simply involves alternate immersions of a charged substrate into an aqueous solution of a polycation and an aqueous solution of a polyanion at room temperature. Since the adsorption is based on the electrostatic attraction of interlayer charges, each layer is self-limiting in thickness (typically 0.3 to 20 nm per layer, depending on materials and conditions) and is uniform at the molecular level. In energy storage devices such as batteries, supercapacitors, and ionic polymer actuators, these thin films are attractive composite electrodes (or porous electrodes) which provide high conductivity for both ions and electrons. In the next section, main components of the IPCNCs will be introduced, and in Chapter 3, the IPCNCs made by direct assembly process and Layer-by-layer self assembly process will be further discussed.

1.2 Main Components of IPCNC Actuators

IPCNC actuators consist of three main components: polymer matrix, electrolyte and conductor network composite (CNC). As illustrated in Figure 1-4, polymer (or ionomer in most cases) is the middle spacer and the matrix material in the CNC, electrolyte provides the mobile charge carriers through the entire system, and the CNC extends the electrode surface area.

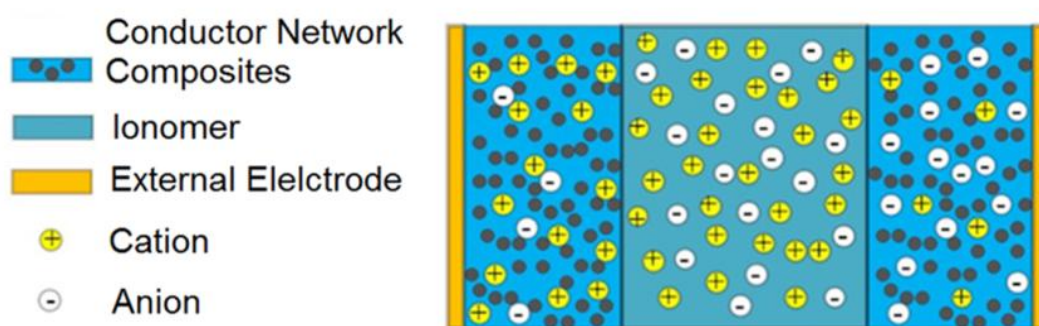


Figure 1-4 Schematic of the cross-section of an IPCNC actuator.

1.2.1 Ionomers/ionic polymers

The polymer matrix serves as a physical binder to support the whole actuator. This binder must be chemically stable and ionic conductive, namely it requires the polymer matrix neither dissolves in electrolytes nor blocks the ion transport between the two CNC layers. Ionomers, which are widely utilized in batteries, supercapacitors, and fuel cells, are often chosen as the polymer matrix in IPCNCs. They comprise both electrically neutral repeating units in the main chains and a fraction of ionized units in the side chains. Ionomers usually have unique physical properties, such as high ionic conductivities, specifically, from their broad ion channels[30, 31] that facilitate fast ion transport. Nafion, which is a benchmark of ionomers invented by Dupont, has been used and investigated extensively. Therefore, the IPCNC actuators based on Nafion will

be discussed in Chapters 3 and 4, and in Chapter 6 (the chapter of investigating polymer matrix), Nafion is selected as the main polymer matrix for a comparison of the new ionic polymers. The detailed morphology of Nafion will be further discussed in Chapter 6.

1.2.2 Ionic liquids

In IPCNC actuators, high ion mobility, large free ion concentration, and large ion size are required for high speed actuation and large strain. Traditional electrolytes in IPCNC actuators are usually neutral molecules, such as ethylene glycol and water.[32] Mobile ions come only from counter-ions in Nafion ionomer, which limits the actuation magnitude. In 2004, Bennett and Leo found that ionic liquids (ILs), which is a type of organic salts in liquid form at room temperature, can provide wider operation voltage range, larger plus faster strain response, and improved reliability for actuator applications, as shown in Figure 1-5. [19]

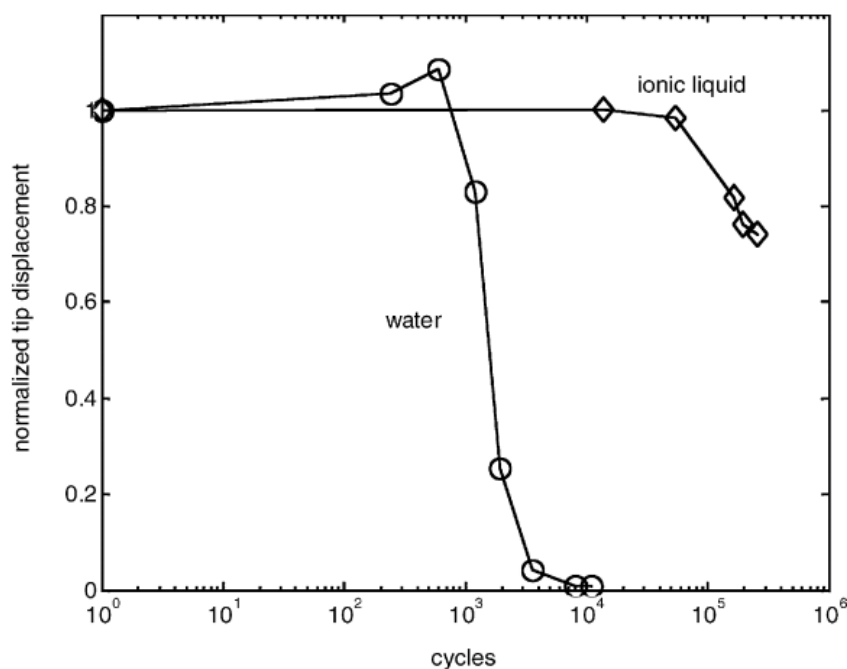


Figure 1-5 Time history of the tip displacement of a Nafion actuator sample in the water and ionic liquid (EMI-Tf) forms. [33]

ILs possess a variety of unique properties, such as negligible vapor pressure, large liquidus range, high thermal stability, high ionic conductivity, and large electrochemical window. All of these properties are highly desirable for electroactive devices such as ionic polymer actuators,[14, 28, 33-35] supercapacitors,[36, 37] batteries,[38, 39] fuel cells,[40] and dye-sensitized solar cells.[41, 42] For example, the negligible vapor pressure of ILs enables these electroactive devices to operate in ambient atmosphere with long life cycles and the wide electrochemical window allows these devices to work at higher voltage (4-5V).

Additionally, an intriguing actuator-oriented characteristic of the ILs is to fine tune the ion size difference by suitable choice of cations and anions. For actuators with ILs as electrolytes, how the mobile ions in ILs affect the bending actuation will be further discussed in Chapter 3 and Chapter 5.

1.2.3 Conductor network composite (CNC)

CNC composite electrodes, in which strain is mainly generated, are the key component in IPCNC actuators and its importance was not fully recognized for a quite long time in the literature of IPCNC (or IPMC).[15] Experimental results indicated that a high concentration of excess charges within the CNC is highly desirable in order to generate high electromechanical actuation. From this point of view, CNCs are fabricated as composites with nano-size materials which offer large electrode areas in contact with ionic polymers and electrolytes. Under electrical fields, excess charges are stored in the CNCs forming double layer capacitor due to the accumulation or depletion of ions near a conductive surface.

Another important aspect of CNCs is that the morphology of the CNC determines the actuation speed of IPCNCs, while traditional CNCs using disordered nanoparticles as conductor

fillers lead to tortuous ion transport paths. Aligned ion channels implemented into IPCNC, which will be discussed in Chapter 4, will achieve high actuation speed.

1.3 Research Contribution and Dissertation Organization

This dissertation develops an in-depth understanding of the physics in ionic polymer composite actuators and provides solutions to improve the actuation speed and the electromechanical energy conversion efficiency.

Important parameters, characterization set-ups, and theoretical models will be first introduced in Chapter 2. To understand the performance of IPCNC actuators with nanoporous electrodes and IL electrolytes, two models will be presented to describe the performance of IPCNCs in Chapter 3. Equivalent circuits are used to model physical components of the actuators, and thus find the major component that controls the actuation speed. Meanwhile, a two-carrier model is built to analyze the back relaxation of IPCNC actuators under a DC field, and thus reveals one of the reasons that lead to the low efficiency of IPCNC actuators. In Chapter 4, vertically aligned carbon nanotubes (VA-CNTs) are introduced to replace disordered nanoparticles in the CNC, which bring several advantages to IPCNC performance. It will be demonstrated that VA-CNTs create straight inter-VA-CNT ion channels for fast ion transport, minimize electrical conduction resistance for reduction of electrical loss, and create anisotropic elastic modulus of the CNCs, which restrict the strain generation in thickness direction, and thus transmitting more strain to the bending.

After discussing and optimizing the CNC, fundamental studies are then introduced in Chapter 5 and 6 for better understanding the roles of ionic liquids and polymer matrix in IPCNC actuators. To simplify the analysis, actuators made with ionic polymer membranes with planar electrodes are investigated. In Chapter 5, the ion distributions are studied by a powerful chemical

analyzing tool – secondary ion mass spectroscopy (SIMS) and the complicated ion cluster effect in ionic polymer actuators is directly observed for the first time. Based on this result, an improved theme of the ion distribution is presented. In Chapter 6, several PVDF based polymer matrices are introduced to substitute Nafion, which was popularly used in the ionic polymer actuators, and all these new polymers demonstrate a larger bending magnitude and an order-of-magnitude higher electromechanical efficiency.

Finally, a summary of this dissertation and the suggestions for future works will be presented in Chapter 7.

Chapter 2

Electrical and Mechanical Characterization Methods

In this chapter, an introduction to the entire dissertation, discussing both experiments and theories is provided. A list of symbols, which contains most parameters studied in this dissertation, is presented in Section 2.1. Furthermore, a series of characterization tools are introduced in Section 2.2. Finally, an intensive introduction and discussion of methods and theories are presented in Section 2.3.

2.1 List of Symbols

All the symbols frequently used in this dissertation are listed in Table 2.1. The ones that are not listed in Chapter 2 will be explained in their corresponding chapter.

Table 2-1 List of symbols and their meanings

Symbol	Meaning
A	Area
An (<i>superscript</i>)	Anion
C	Capacitance or concentration
Cat (<i>superscript</i>)	Cation
d	Distance
dl (<i>subscript</i>)	Double layer
e (<i>subscript</i>)	Effective layer or electrical
F	Force
i (<i>subscript</i>)	Ionic polymer
I	Momentum of inertia or Current
j	Imaginary unit
L	Length
m (<i>subscript</i>)	Metal electrode layer
M	Torque
Mw	Molecular weight

Q	Charge
R	Radius or Resistance
s_{ij}	Elastic compliance constant
s (<i>subscript</i>)	In series
S	Strain
t	Thickness or Time
T	Stress or Temperature
u	Energy density
U	Energy
V	Voltage or Volume
V_f	Volume fraction
w	Width
wt	Weight
Y	Young's modulus
Z	Electrical complex impedance
ε_0	Vacuum permittivity
ε_R	Relative permittivity
ϕ	Complex impedance phase angle
ω	Angular frequency ($2\pi f$)
τ	Time constant
κ	Bending curvature
σ	Conductivity
μ	Mobility
ρ	Density
η	Efficiency

2.2 Characterization Setups

2.2.1 Electrical characterization setups

Electrical Characterizations, such as Electrochemical Impedance Spectroscopy (EIS), Potentiostatic charging, Cyclic Voltammetry (CV), provide the most important information of the charge dynamics of the ionic polymer actuators. As shown in Figure 2-1, a Princeton Applied

Research PARSTAT 2273 Potentiostat was used in all the electrical characterizations. Since this potentiostat has a low sampling rate, fast changing signal may not be fully digitized. Therefore, a Lecroy WaveSurfer oscilloscope with a high sampling rate (500Mpts/s), as shown in Figure 2-2, was utilized to capture the fast charging/discharging response of the actuators.



Figure 2-1 Photo of Princeton Applied Research PARSTAT 2273 Potentiostat.

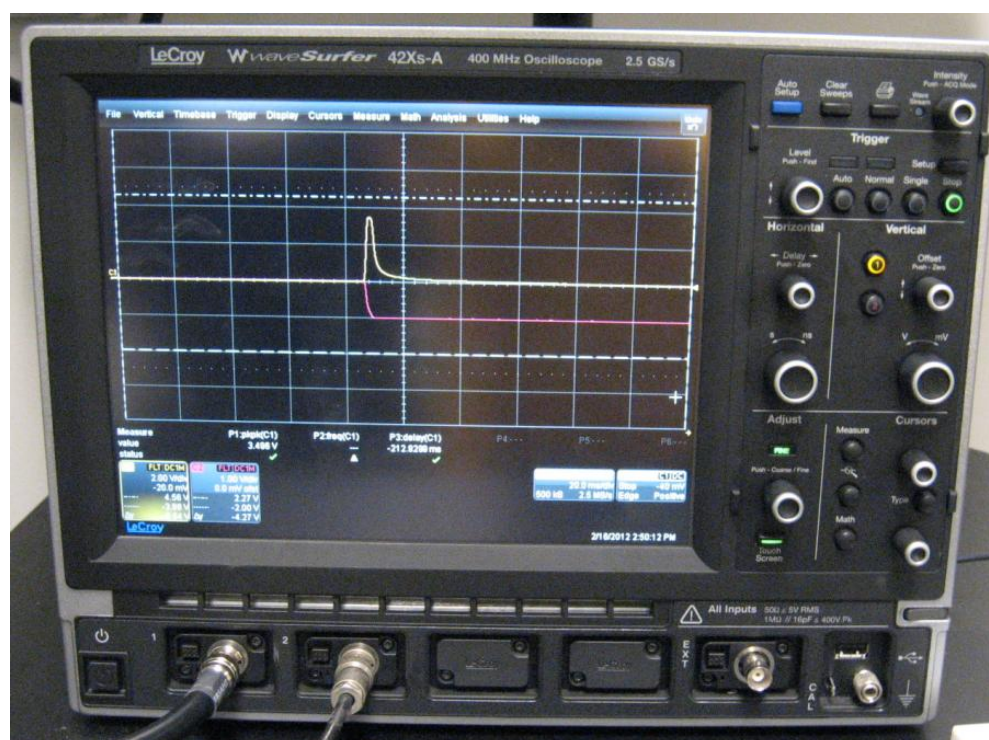


Figure 2-2 Photo of Lecroy wavesurfer 42Xs-A Oscilloscope

2.2.2 Mechanical characterization setups

A dynamic mechanical analyzer (TA DMA 2980 dynamic mechanical analyzer), as shown in Figure 2-3, was used to study and characterize the mechanical properties of the polymer materials in this dissertation. A sinusoidal stress was applied to a polymer stripe and the strain in the material was measured, allowing one to determine the complex modulus. The temperature of the sample and the frequency of the stress were varied, therefore temperature dependent modulus at different frequencies (usually 1,2,5,10Hz) were recorded.



Figure 2-3 Photo of TA DMA 2980 Dynamic mechanical analyzer with a liquid N₂ Cooling unit.

For some IL containing ionic polymer thin films, the modulus was too low for the DMA to capture or the sample yielded easily. Therefore, a set-up was specially designed to measure the low modulus of these soft thin films, as shown in Figure 2-4 and 2-5. An electromagnetic Shaker from KCF Technologies was used to stretch film periodically with adjustable amplitude and frequency. A load cell was used to measure force F on the fixed end of polymer film during stretching. A probe from photonic sensor MTI-2000 was set in front of the shaker so that the elongation amount is known. The three instruments were connected to a lock-in amplifier Stanford SR-830, which measured the input signal only from load cell and photonic sensor with the same frequency of output one to the shaker. The Young's modulus was then calculated with formula

$$Y = \frac{FL}{wt\Delta L} \quad (2.1)$$

where L , w , t , ΔL are the length, width, thickness and elongation of actuator films, respectively. F is the applied force.

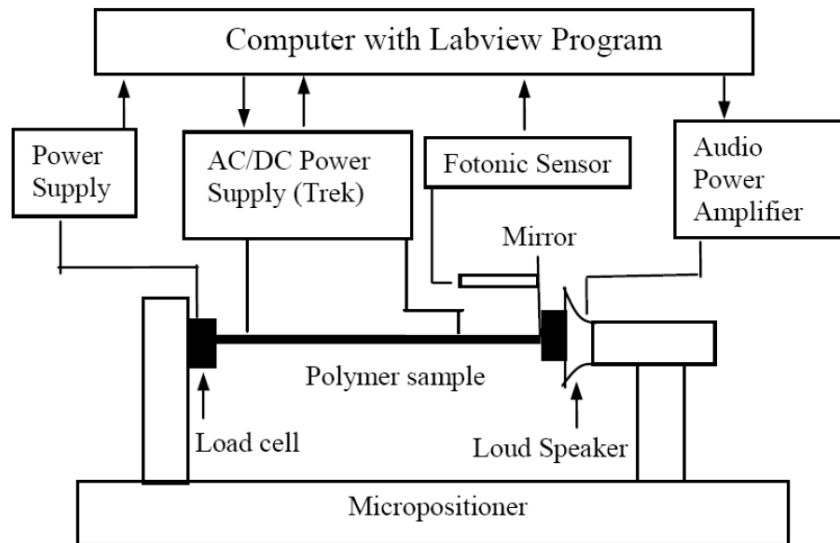


Figure 2-4 Schematic of modulus measurement set-up for ultra-soft materials[43]

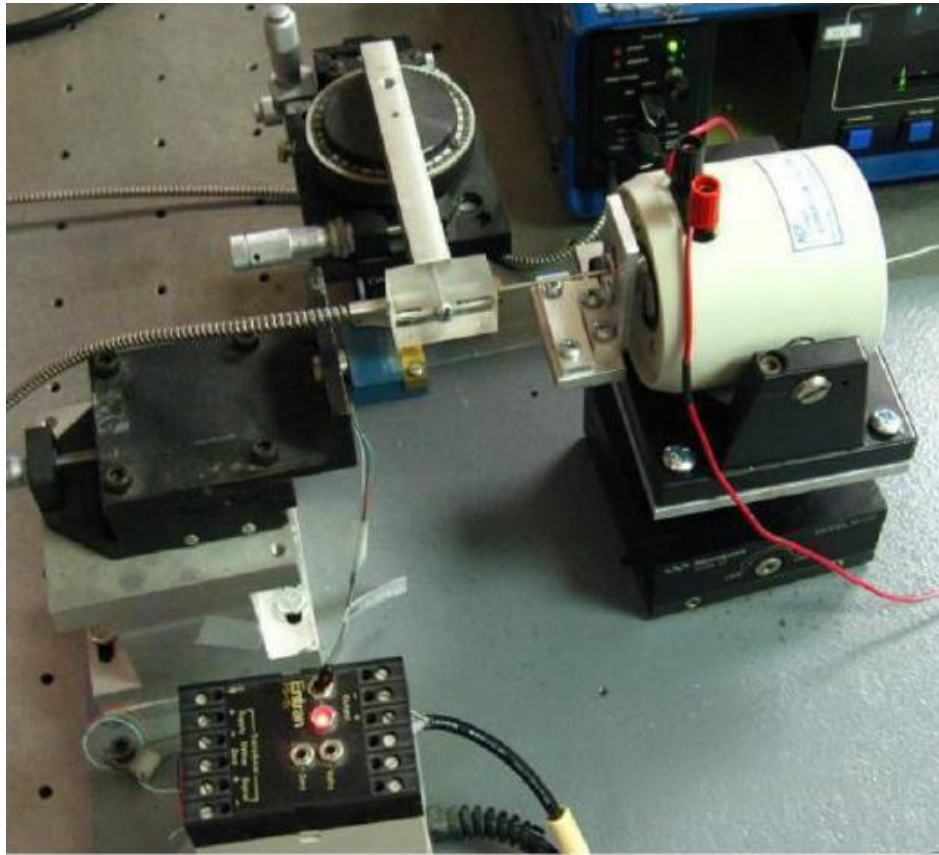


Figure 2-5 Photo of modulus measurement set-up for ultra-soft materials

2.2.3 Electromechanical characterization setups

In Figure 2-6 and Figure 2-7, a schematic drawing and a picture of the electromechanical measurement set-up are displayed, respectively. In this measurement, two probes, which were connected to a power supply or a function generator, are clamped to the actuator samples to provide both electrical connections and mechanical supports. Since the actuators were only about 8 to 10 mm long, their bending actuations were too small for a direct observation by the naked eye or an ordinary camera. Therefore, a microscope was used to amplify the actuation image and a charge-coupled device (CCD) camera was used to record the image with a rate 1-200 frames/s. The images were then collected and analyzed by a computer installed with Labview and Matlab.

Thus, the bending curvature, which is used to calculate strain, stress and mechanical energy through the entire dissertation, was retrieved from recorded images.

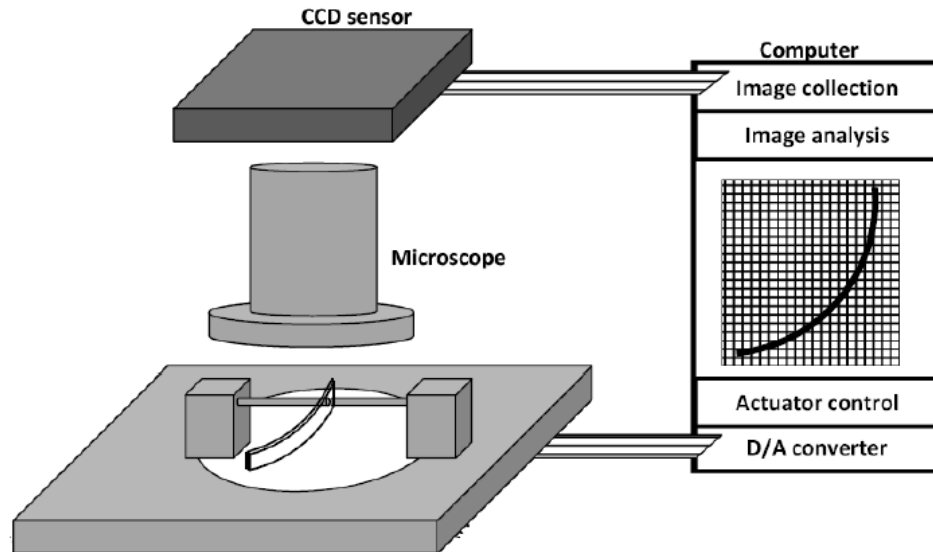


Figure 2-6 Schematic of bending actuation measurement set-up[43]

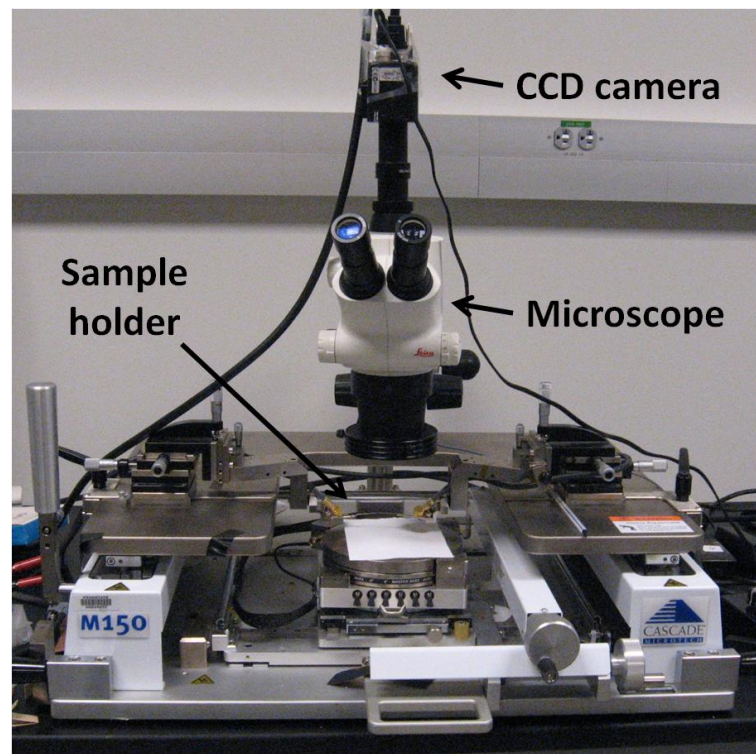


Figure 2-7 Photo of bending actuation measurement set-up

2.2.4 Chemical characterization setups (Secondary Ion Mass Spectroscopy)

Secondary ion mass spectrometry (SIMS), which is a technique used in materials science and surface science to profile the composition of solid surfaces and thin films, was utilized in Chapter 5 to study the ion distribution in ionic polymer actuators under an applied field. SIMS is based on the observation of secondary ions that are ejected from a sample surface when bombarded by a primary beam of heavy particles, as illustrated in Figure 2-8.

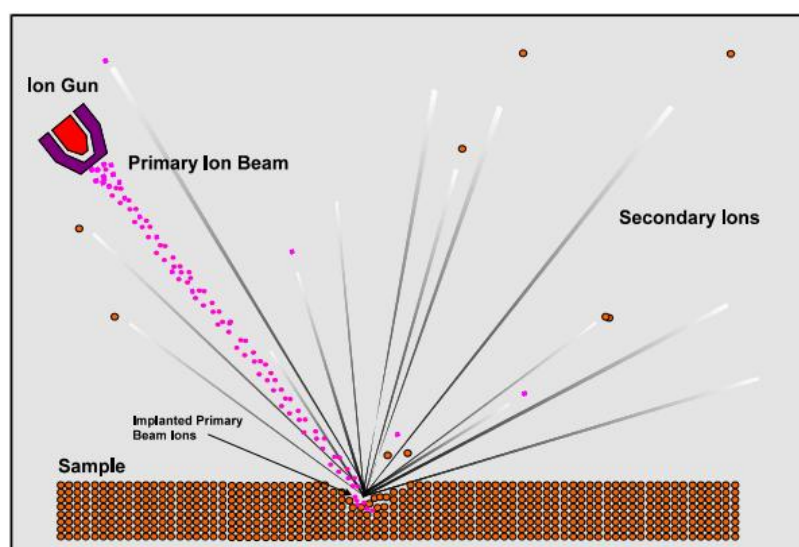


Figure 2-8. Schematics of secondary ion sputtering [44]

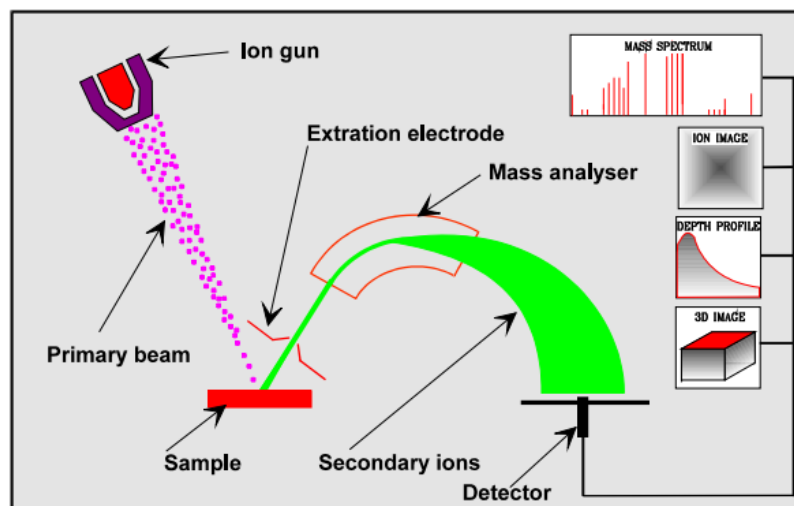


Figure 2-9. Components of SIMS [44]

As shown in Figure 2-9, a basic SIMS instrument consists of a primary beam source to supply the bombarding species, a target or sample that must be solid and stable in a vacuum, a method of collecting the ejected secondary ions, a mass analyser to isolate the ion of interest, and an ion detection system to record the magnitude of the secondary ion signal. The mass analyser may be a quadrupole mass analyser (with unit mass resolution), magnetic sector mass analyser or time-of-flight (ToF) analyser. Since ToF analysers provide substantially higher sensitivity and mass resolution, and a much greater mass range, they are preferred in the studies performed in this dissertation. This is based on the fact that ions with the same energy but different masses travel with different velocities, therefore, measuring the flight time for each ion allows the determination of its mass.

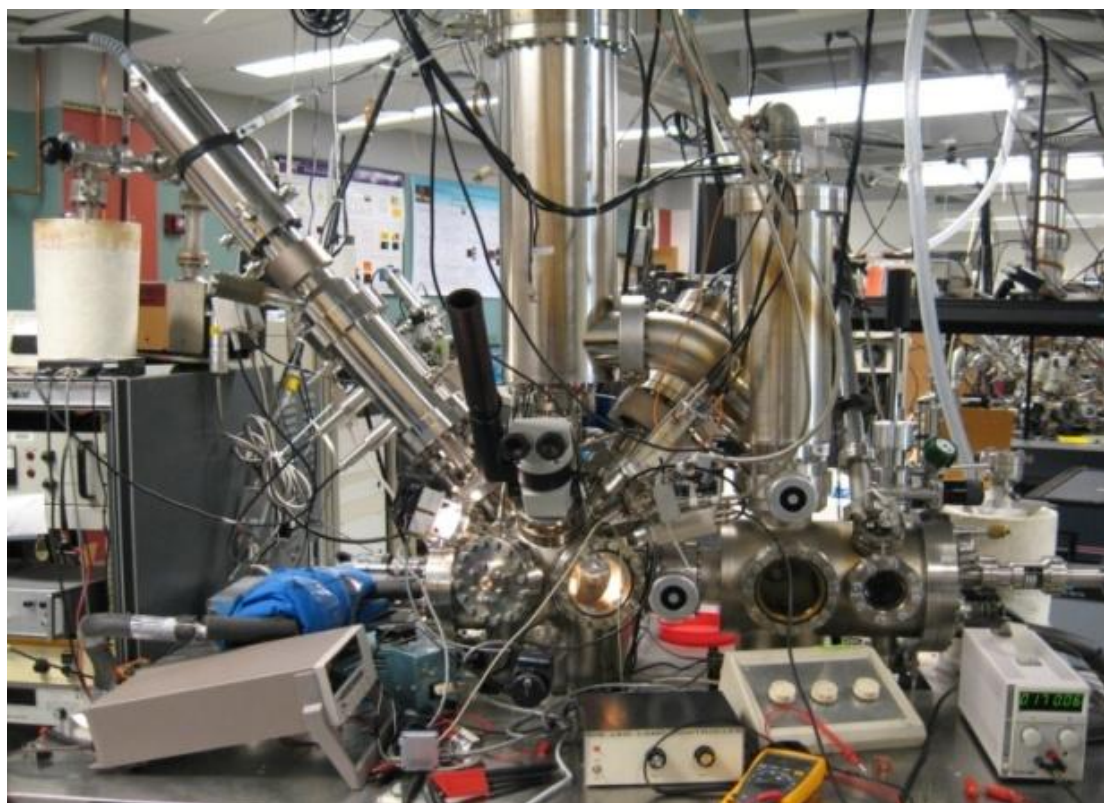


Figure 2-10. ToF-SIMS located in Winograd Lab at Penn State.

Time-of-Flight Secondary Ion Mass Spectrometry (ToF-SIMS) is a powerful tool in imaging of biomaterials, particularly tissue samples [45, 46] and single biological cells [47-49]. Figure 2-10 shows the ToF-SIMS that was utilized in this dissertation. High energy C_{60}^{+} primary ions are supplied by an ion gun and focused on to the target sample, which ionizes and sputters some atoms off the surface. These secondary ions are then collected by ion lenses and filtered according to atomic mass, then projected onto a Micro-channel plate (MCP) detector.

ToF-SIMS with cluster ion beam allows etching the organic materials without damaging their chemical integrity, so that the change in ion concentration along the film thickness direction can be probed directly.[49, 50] With this advantage, ToF-SIMS with C_{60}^{+} cluster ions has been successfully performed on various materials to collect molecular depth-profile information.[51-56] This unique property makes it possible to study the electrode-electrolyte interaction in IPCNC actuators, which will be discussed in Chapter 5, and an even broader range of organic material based energy storage devices, such as supercapacitors and Li-polymer batteries.

2.3 Properties and Models of Ionic Polymer Actuators

2.3.1 Mechanical properties

For ionic polymer actuators which convert electricity into mechanical energy, their mechanical properties have the highest priority to be characterized; therefore some key mechanical properties of ionic polymer actuators are discussed in this section.

2.3.1.1 Intrinsic stress and strain in a bimorph actuator

As introduced in Chapter 1, in this dissertation, two types of ionic polymer actuators are investigated. One is ionic polymer membrane actuators with planar electrodes, which will be mechanically analyzed in this section, and the other one is IPCNC actuators that will be discussed in the next section.

In bending actuators studied in this dissertation, the intrinsic stress/strain that is initially generated in the actuator materials can be extracted from the bending curvature of actuators. In this section, an *i*-EAP membrane actuator is modeled as a bimorph beam with an assumption that an intrinsic extension strain $+S_{10}^i$ (contraction strain $-S_{10}^i$) is uniformly generated in the upper (lower) half of the polymer membrane, as shown in Figure 2-11. The subscripts i and m denote the quantities in the ionic polymer layer and the Au metal layer, respectively. In the bending actuators, the actual strain in the ionic polymer is reduced due to the stress from Au layer, i.e.,

$$S_1^i = S_{10}^i + s_{11}^i T_1^i \quad (2.2)$$

where s_{11}^i is the elastic compliance and T_1^i is the stress along the film surface.

For the bimorph actuator in Figure 2-11, it can be derived that the strain S_1^i is related to the radius of curvature R .

$$S_1^i = \frac{L' - L}{L} = \frac{(d + R)\theta - R\theta}{R\theta} = \frac{d}{R} = \kappa d \quad (2.3)$$

where L' and L are the length at $y=0$ and $y=d$, respectively. d is the distance in the thickness direction of the layer to the middle plane (assume bimorph is symmetric); θ is the center angle of the bending curvature; κ is the curvature. Substituting (2.3) into (2.2) and noting that the elastic compliance s_{11}^i is the reciprocal of Young's modulus Y^i , the stress T_1^i can be deduced as

$$T_1^i = (s_{11}^i)^{-1} S_1^i - (s_{11}^i)^{-1} S_{10}^i = Y^i (\kappa d) \pm Y^i S_{10}^i \quad (2.4)$$

Similarly, since Au layer does not generate strain, T_1^m can also be derived as

$$T_1^m = Y^m(\kappa d) \quad (2.5)$$

Since the actuator length is much larger than the thickness and width, we assume that all the other stress components are very small compared to T_1 .

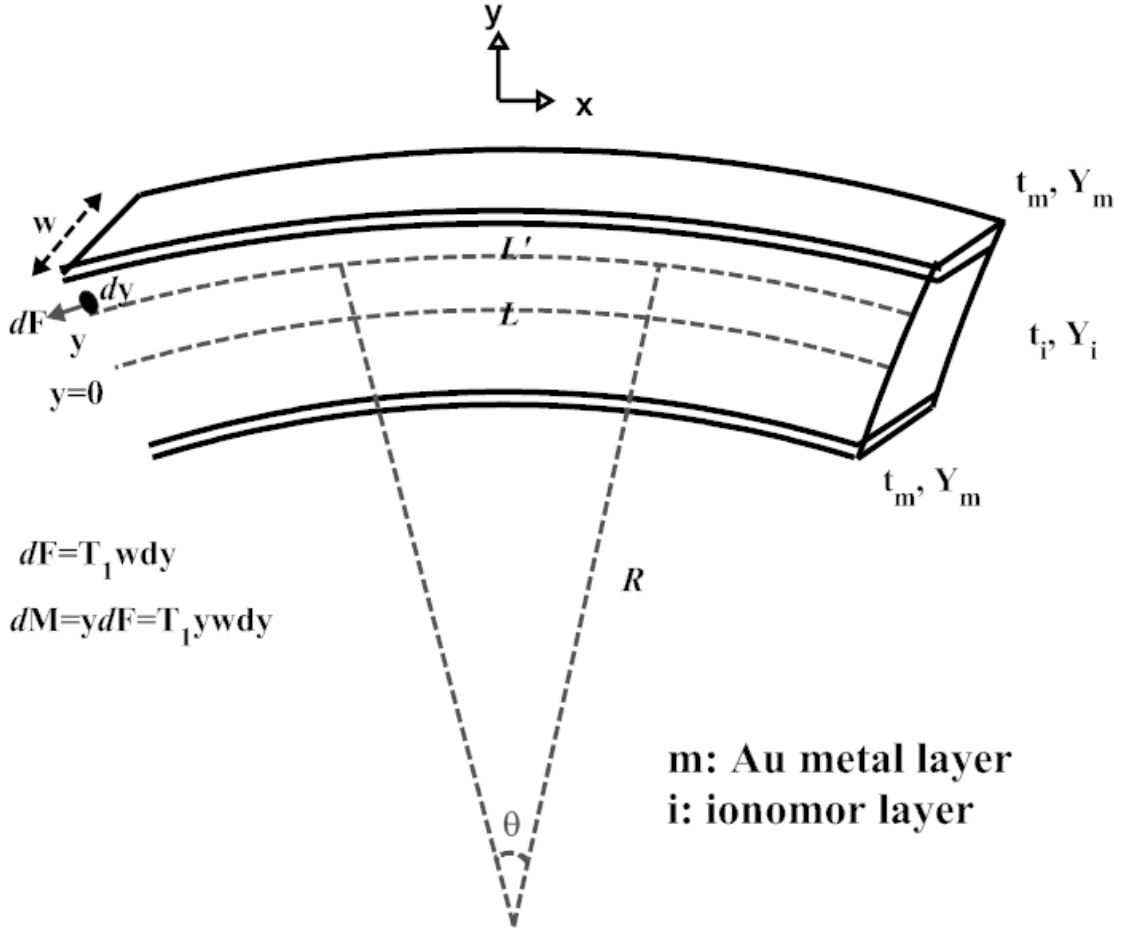


Figure 2-11. Mechanical schematic of a bimorph actuator

From the equilibrium conditions, when there is no external force or moment, the total moment M and total force F satisfy $\int dM = 0$ and $\int dF = 0$. When the strain in the two CNC

layers of the bending actuator are the same magnitude with opposite sign, the intrinsic strain S_{10}^i and intrinsic stress $T_{10}^i = Y^i S_{10}^i$ can be deduced as follows, (shown in Appendix A)

$$S_{10}^i = -\frac{Y^m(8t^m{}^3 + 12t^m{}^2 t^i + 6t^m t^i{}^2) + Y^i t^i{}^3}{3Y^i t^i{}^2} \cdot \kappa \quad (2.6)$$

$$T_{10}^i = -\frac{Y^m(8t^m{}^3 + 12t^m{}^2 t^i + 6t^m t^i{}^2) + Y^i t^i{}^3}{3t^i{}^2} \cdot \kappa \quad (2.7)$$

where t^m , t^i are the thickness of the Au metal layer and polymer layer, respectively.

2.3.1.2 Intrinsic stress and strain in an IPCNC actuator

Presented in Figure 2-12 is the mechanical schematic of an IPCNC actuator. The subscripts i , e and m denote the quantities in the ionic polymer layer, effective (CNC) layer and Au metal layer, respectively. In most of the cases, especially Nafion based IPCNC actuators, the bending motion of IPCNC actuator is much larger than the membrane actuators without CNC, so that the stress generated in the middle layer spacer of IPCNC actuator is usually neglected.

In the model for IPCNC actuators, it is assumed that the bending actuation is generated by a uniform intrinsic strain $\pm S_{10}^e$ only in the effective (CNC) layers. Following the derivation in the last section, one could obtain the relations below,

$$S_1^e = \frac{L' - L}{L} = \frac{(d + R)\theta - R\theta}{R\theta} = \frac{d}{R} = \kappa d \quad (2.8)$$

$$T_1^e = (s_{11}^e)^{-1} S_1^e - (s_{11}^e)^{-1} S_{10}^e = Y^e(\kappa d) \pm Y^e S_{10}^e \quad (2.9)$$

and similarly,

$$T_1^m = (s_{11}^m)^{-1} S_1^m = Y^m(\kappa d) \quad (2.10)$$

$$T_1^i = (s_{11}^i)^{-1} S_1^i = Y^i (\kappa d) \quad (2.11)$$

where s_{11}^e , s_{11}^m , s_{11}^i are the elastic compliances of the effective (CNC) layer, Au metal layer, and ionic polymer layer; Y^e , Y^m , Y^i are the Young's modulus of the effective (CNC) layer, Au metal layer, and ionic polymer layer; T_1^e , T_1^m , T_1^i are the stresses along the film surface of the effective (CNC) layer, Au metal layer, and ionic polymer layer, respectively.

In equilibrium conditions, when there is no external force or moment, the total moment M and total force F of the bending actuator satisfy $\int dF = 0$ and $\int dM = 0$. Therefore, the intrinsic strain S_{10}^e and intrinsic stress $T_{10}^e = Y^e S_{10}^e$ in the CNC layer can be derived as, (shown in Appendix A)

$$S_{10}^e = - \frac{Y^m \left(\frac{2t^m{}^3}{3} + 2t^m \left(t^m + \frac{t^i}{2} \right)^2 + t^m{}^2 (2t^e + t^i) \right) + Y^e \left(\frac{2t^e{}^3}{3} + t^e \frac{t^i{}^2}{2} + t^e{}^2 t^i \right) + Y^i \frac{t^i{}^3}{12}}{Y^e (t^i t^e + t^e{}^2)} \cdot \kappa \quad (2.12)$$

$$T_{10}^e = - \frac{Y^m \left(\frac{2t^m{}^3}{3} + 2t^m \left(t^m + \frac{t^i}{2} \right)^2 + t^m{}^2 (2t^e + t^i) \right) + Y^e \left(\frac{2t^e{}^3}{3} + t^e \frac{t^i{}^2}{2} + t^e{}^2 t^i \right) + Y^i \frac{t^i{}^3}{12}}{Y^e (t^i t^e + t^e{}^2)} \cdot \kappa \quad (2.13)$$

where t^e , t^m , t^i are the thickness of the effective (CNC) layer, Au metal layer, and ionic polymer layer, respectively.

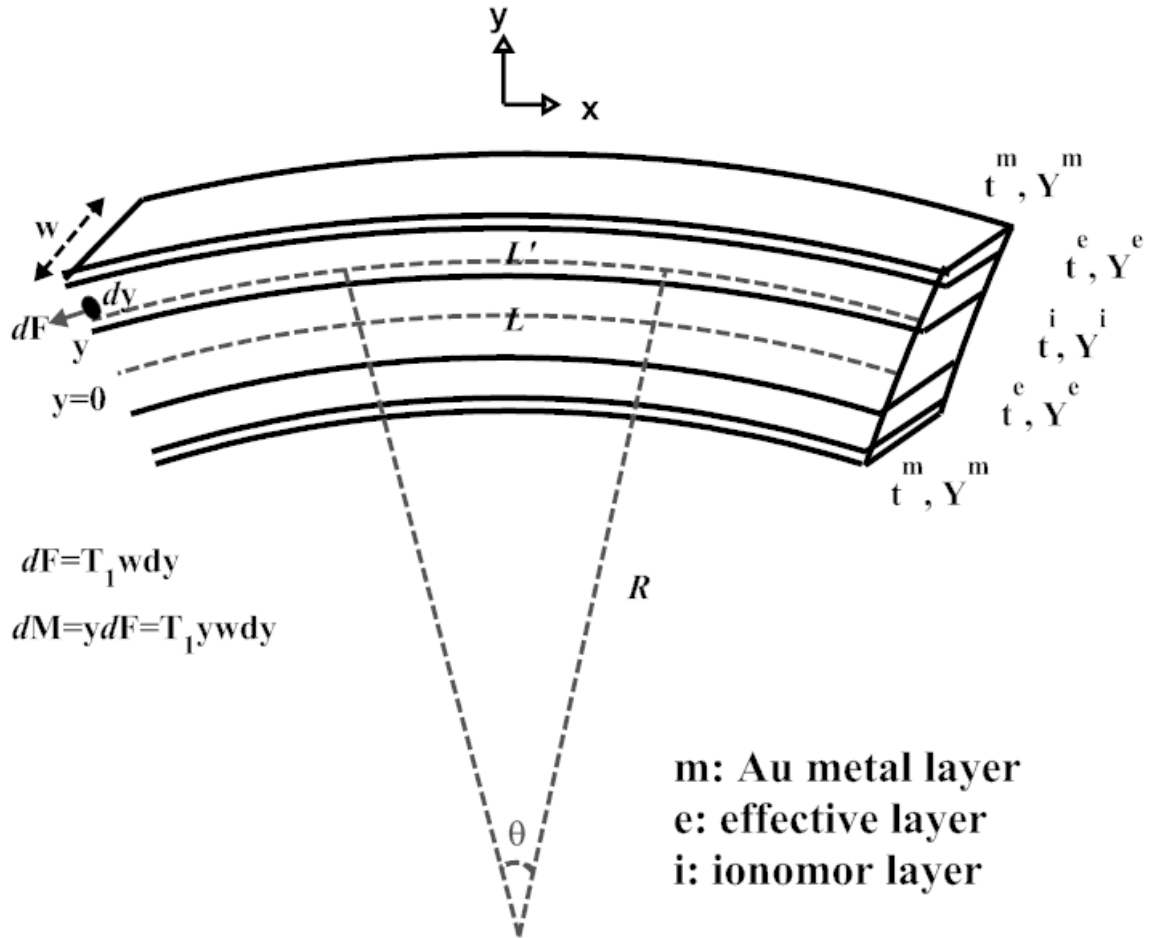


Figure 2-12 Mechanical schematic of an IPCNC actuator

2.3.1.3 Elastic modulus

As can be seen from the last two sections, the Young's moduli of all different layers are important parameters in deriving the stress and strain in bimorph ionic polymer membrane actuators and IPCNC actuators. For most materials used in ionic polymer membrane actuators, the moduli could be easily measured by instruments such as dynamic mechanical analysis (DMA) that is shown in Section 2.2.2. But for the multi-layer structures used in IPCNC actuators, determining the modulus of an individual CNC layer which was either very thin or not

mechanically strong enough to form a free standing film, is very difficult. In these cases, the CNC layers were attached to a piece of free standing polymer film whose modulus was known. For the bi-layer laminate with length much larger than the other dimensions, as illustrated in Figure 2-13, the measured elastic modulus Y is related to the Young's modulus of each layer Y_a and Y_b as

$$Y = aY_a + bY_b = \frac{t_1Y_a + t_2Y_b}{t_1 + t_2} \quad (2.14)$$

where a and b are the volume fractions of each layer, respectively, and both a and b could be calculated from the thickness of each layer, t_1 and t_2 . Therefore, when Y_a and Y are known, Y_b could be calculated.

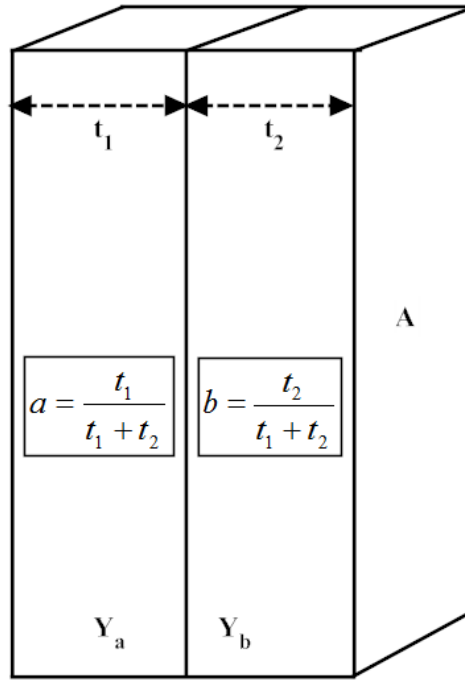


Figure 2-13 Schematic of a bi-layer laminate for the characterization of the elastic modulus of individual layers.

2.3.1.4 Mechanical energy and electromechanical efficiency

In ionic polymer actuators, the input energy comes from electricity of an external power source and the output energy is in the form of strain and stress. The efficiency of energy conversion from electrical to mechanical energy is known as the electromechanical energy efficiency, which is an important parameter in evaluating actuators based on *i*-EAPs or other types of EAPs.

The mechanical energy of the ionic polymer membrane actuator and IPCNC actuators can be calculated from the bending curvature κ and the Young's modulus of each layer by the equations below,

$$U_m = wL \left[\int_0^{\frac{t_i}{2}} Y_i(\kappa y)^2 dy + \int_{\frac{t_i}{2}}^{\frac{t_i}{2} + t_m} Y_m(\kappa y)^2 dy \right] \text{ (for membrane actuators)} \quad (2.15)$$

$$U_m = wL \left[\int_0^{\frac{t_i}{2}} Y_i(\kappa y)^2 dy + \int_{\frac{t_i}{2}}^{\frac{t_i}{2} + t_e} Y_e(\kappa y)^2 dy + \int_{\frac{t_i}{2} + t_e}^{\frac{t_i}{2} + t_e + t_m} Y_m(\kappa y)^2 dy \right] \text{ (for IPCNC actuators)} \quad (2.16)$$

where y is the distance from the middle plane of the actuator, w is the width of the actuator, and L is the length of the actuator, as shown in Figure 2-11 and 2-12.

The total input electric energy U_e of the ionic polymer actuators is

$$U_e = \int Q(V) dV \quad (2.17)$$

Under a direct current (DC) bias, the electrical energy U_e of the ionic polymer actuators can be calculated as follows,

$$U_e = QV \quad (2.18)$$

where Q is the charge, V is the applied voltage.

Hence, the electromechanical energy efficiency of the actuators can be deduced by the following relation,

$$\eta = U_m / U_e \times 100\% \quad (2.19)$$

2.3.2 Electrical properties and models

Electrical properties of the ionic polymer actuators are also crucial to their performance. In this section, technical terms that are commonly discussed in Chapter 3-6, such as electrical impedance, equivalent circuits, ionic conductivity, and electrical double layer capacitance are introduced. Some important electrical models and the relations between these electrical models, such as the relation between electrode polarization model and equivalent circuits, are also derived in this section by the author.

2.3.2.1 Electrical impedance and equivalent circuits

In electrochemical devices, the complex impedance, which is the complex ratio of the voltage to the current in an alternating current (AC) circuit, is commonly characterized to illustrate electrical properties of the system. The polar form of the complex impedance Z is shown below, in which both magnitude and phase characteristics are captured.

$$Z(\omega) = |Z(\omega)| e^{j\phi(\omega)} \quad (2.20)$$

where the magnitude $|Z(\omega)|$ represents the ratio of the voltage difference amplitude to the current amplitude, ϕ gives the phase difference between voltage and current, and ω is the frequency.

Z can also be presented in Cartesian form as below,

$$Z(\omega) = Z'(\omega) + jZ''(\omega) \quad (2.21)$$

where $Z'(\omega)$ is real impedance, $Z''(\omega)$ is imaginary impedance.

With impedance spectroscopy, the charge dynamics of mobile charge in the bulk or interface region of solid or liquid can be analyzed, where small voltage ($\sim k_B T/e$) perturbation results in linear response of the system.

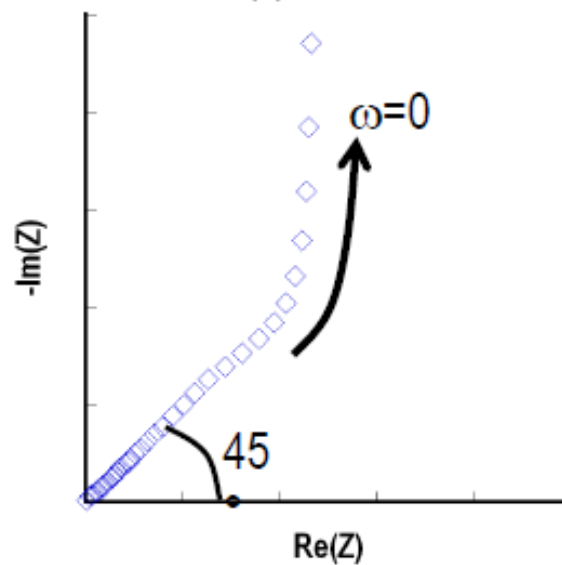


Figure 2-14 Nyquist plot of complex impedance

Beside the above presentations of the electric impedance, Z is often represented in the so-called Nyquist plot, where the imaginary part of the impedance Z'' is plotted as a function of the real part Z' , as shown in Figure 2-14. Equivalent circuit models are widely used to analyze the Nyquist plot (electric impedance), where they provide understandings on how various components contribute to the device performance, as illustrated in Figure 2-15 and 2-16.

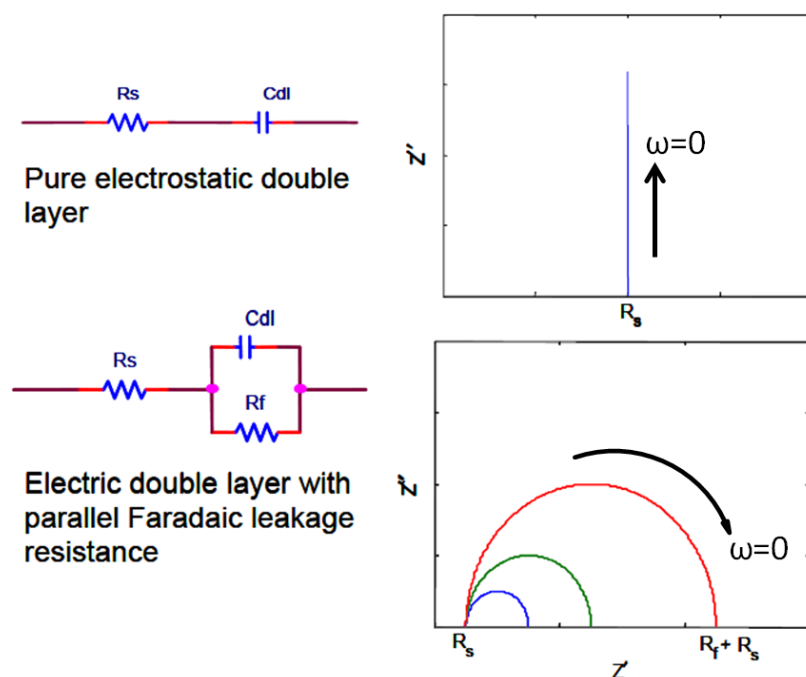


Figure 2-15: The complex plane representation of a simple electric double layer, and a double layer with leakage resistance.[57]

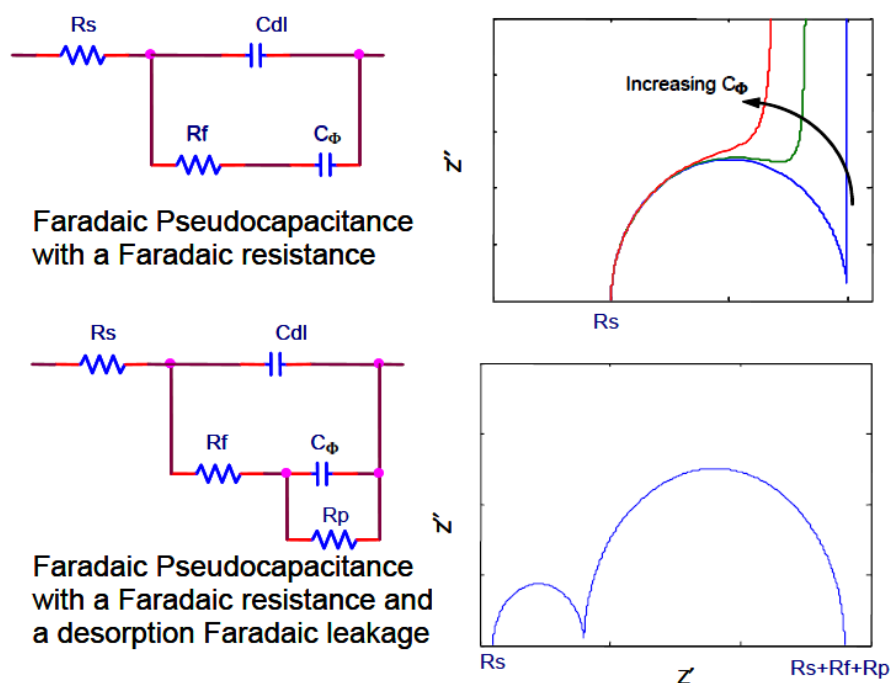


Figure 2-16 The complex plane representation of a pseudo-capacitor and a pseudo-capacitor with leakage resistance.[57]

2.3.2.2 Electrical double layer theories and ionic conductivity

The electric impedance of ionic polymer membrane actuators is strongly frequency dependent and actually is more complicated than R-C networks. Classic Gouy-Chapman-Stern (GCS) model introduced a concept called electric double layer, which consists two layers: Stern layer and diffuse layer to describe the ion concentration profile near charged electrodes, as shown in Figure 2-17. Since this model was mathematically described with Debye-Hückel equation (linearized Poisson-Boltzmann equation), the electric double layer hence possesses a characteristic length L_D , called Debye screening length, which is in the range of nanometer.[57] However, all the above theories were originally derived for dilute solutions, so that for the devices operating with ionic liquids, which is a class of concentrated electrolytes, they cannot fully describe the picture of the ion response under an electric field.

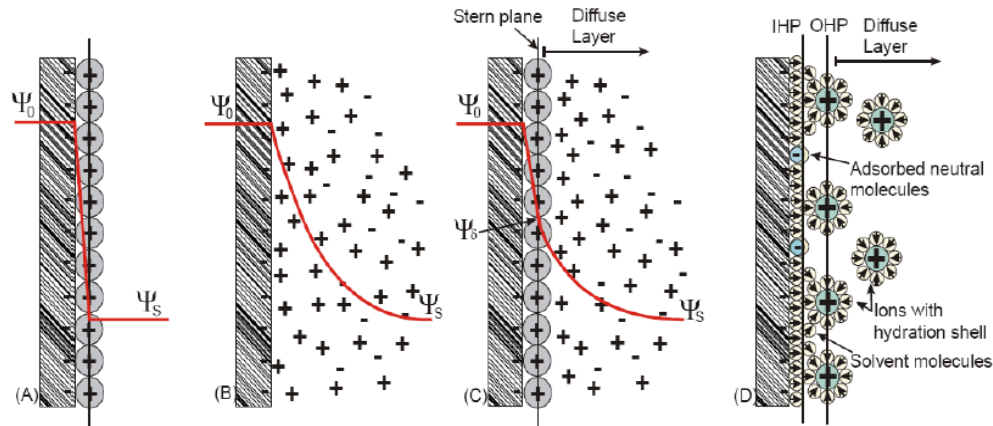


Figure 2-17 Electric double layer models for dilute solution. (a) Helmholtz model, (b) Gouy-Chapman, (c) Stern, and (d) Bockris, Devanathan, and Muller (BDM) model. [57]

Only under a small electric field, the electric response of ionic liquids can be linearized, therefore, recent studies successfully adopted Poisson-Nernst-Planck (PNP) equations to analyze the charge dynamics of ionic liquids, which will be introduced in Section 2.3.2.4.[58] Particularly, since the stationary solution of PNP equations is Poisson-Boltzmann (PB) equation and further linearizing PB equation gives Debye-Hückel equation, the Debye screening length is still an

important characteristic parameter for the electric double layer of ionic liquids, under the limit of low field (or short time scale, when the perturbation to the system is subtle). Gouy-Chapman solved the non-linear PB equation and their solution is provided in Appendix B.[59]

For ionic liquids, detailed structure of the electric double layer in GCS model may not be valid, particularly under high electric field. To illustrate the general picture of the ion distribution in a broad range of voltages, in this dissertation, the term “electric double layer” is used to represent the screening of the external field by drifting ions. Physically, the electric response of ionic liquids in a plane-parallel device consists two parts: fast ion drift (electric field driven) that leads to an electric double layer with Debye screening length L_D , and slow ion diffusion (concentration gradient driven) that builds a diffuse ion layer. Further discussion of current theories and the diffuse ion layer will be continued in Chapter 5.

At high enough frequencies, the diffuse ion layer, which possesses a long response time, cannot effectively form. Therefore, $C(f)$ and $R(f)$ in the frequency domain own plateau regions at high frequencies that are just corresponding to the electric double layer capacitance C_{dl} and bulk ionic resistance R of the ionic polymer, respectively, as shown in Figure 2-18.

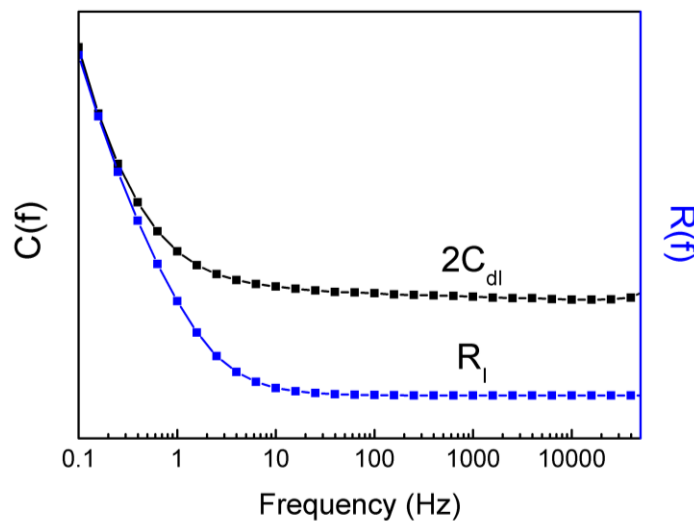


Figure 2-18 The electric double layer capacitance and bulk ionic resistance of an ionic polymer membrane actuator

In this case, the high frequency complex impedance of an ionic polymer membrane could be considered as a simple R-C circuit, as illustrated in Figure 2-19. Here, since the capacitance caused by the dielectric constant of the entire sample is much smaller than the electric double layer capacitance in the frequency range of our study, it is temporarily omitted in this section. At large enough frequency, this capacitance will dominate the response of the entire device, as modeled and discussed in the next section.

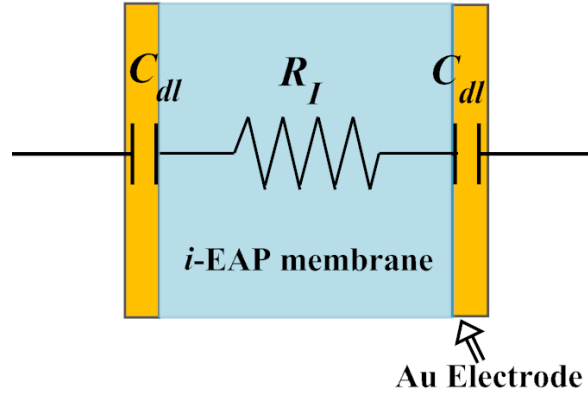


Figure 2-19 Equivalent circuit of an ionic polymer membrane actuator

Hence R_I and C_{dl} could be calculated from Z' and Z'' as follows,

$$R_I = Z' \quad (2.22)$$

$$C_{dl} = \frac{1}{2\omega Z''} = \epsilon \frac{A}{L_D} \quad (2.23)$$

where ϵ is the dielectric constant of the material, A is the area of the ionic polymer membrane and L_D is the Debye length. The ionic conductivity σ of the ionic polymer membrane can be calculated from R_I by the following formula,

$$\sigma = \frac{L}{R_I A} \quad (2.24)$$

where L is the thickness of the ionic polymer membrane. The ionic conductivity discussed in this dissertation is also called dc ionic conductivity in the literature. [60]

Similarly, electrical properties of IPCNC actuators can also be extracted from their high frequency impedance. As frequency increases, the real part of the impedance Z' gradually approaches $R_I + R_{CNC}$, where R_{CNC} is the resistance in CNC layers. Since R_I can be determined from another single piece of ionic polymer membrane which is the same as the one used in IPCNC actuators, after deducing R_I from Z' at high frequency, the ionic conductivity of the CNC σ_i could be calculated with the following formula,

$$\sigma_i = \frac{t_{CNC}}{R_{CNC}A} \quad (2.25)$$

where t_{CNC} is the total thickness of CNC layers and A is the area of the IPCNC actuator.

Although conductivity and electrical double layer capacitance can be obtained from high frequency impedance, due to the un-defined nature of the capacitance value measured from impedance at low frequency, it is hard to obtain explicit information of the diffuse layer formation. Additionally, the impedance method is not suitable for characterizations under high applied voltage, due to heating and the rise of highly non-linear responses. Therefore, a time domain characterization method and theory about the charge dynamics in ionic polymer membrane actuators will be introduced in Section 2.3.2.4.

2.3.2.3 Electrode polarization (EP) model

Another approach to understand the electric impedance of an ionic polymer membrane actuator is to explain the complex dielectric constant versus frequency with the theories of electrode polarization (EP).[60-62] A simple condition, which is a parallel-plate under an

electrical bias, is discussed in the EP model. The charge distribution of an ionic polymer membrane between parallel plates is shown in Figure 2-20.

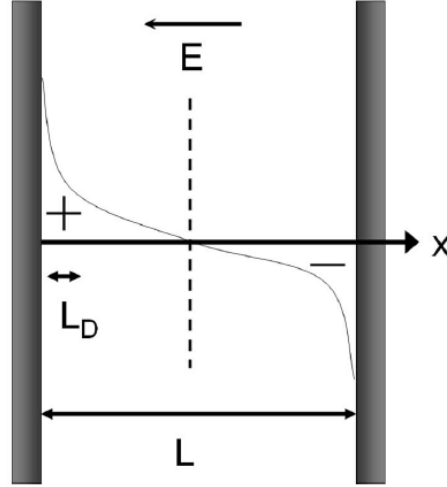


Figure 2-20 Schematic of charge density distribution under a dc parallel-plate field. [61]

Here, it is assumed that the AC applied field $E = E_a e^{i\omega t}$ is a small magnitude that the charge concentration throughout the ionic polymer membrane remains close to the equilibrium charge concentration n_0 , so that the concentration $n(x)$ could be written into

$$n(x) = n_0 + v(x)e^{i\omega t} \quad (2.26)$$

where the perturbation of the carrier concentration $v(x)$ is very small in magnitude comparing to n_0 , and ω is the angular frequency of the applied field.

When Poisson's equation and the carrier conservation are applied to local carrier concentration $n(x)$ and local current density $j(x)$, a simple second-order equation can be obtained,

$$\frac{d^2 v}{dX^2} - v = 0, \quad (2.27)$$

where $X = (x/L_D)\sqrt{1+j\omega\tau}$, L_D is the Debye length, $L_D = (1/e)\sqrt{\epsilon kT/n_0}$ and τ is the dielectric relaxation time, $\tau = \epsilon/n_0 e\mu$. Here, k is Boltzmann's constant and T is temperature.

Integration of equation (2.27) gives $v(x)$, from which the charge distribution, $\rho(x)$, and the polarization $P = (1/L) \int x\rho(x)dx$ can be obtained. Furthermore, the effective dielectric constant $\varepsilon^* = \varepsilon + P(\omega)/E_a$, thus can be written into a simple Debye relaxation,

$$\varepsilon_{EP} = \varepsilon_R \left(1 + \frac{M-1}{jM\omega\tau + 1}\right) \quad (2.28)$$

where ε_{EP} is ε^* , ε_R is the dielectric permittivity of the material, and $M = L/2L_D$. [60]

By defining $\Delta\varepsilon_R = (M-1)\varepsilon_R$ and $\tau_{EP} = M\tau$, the dielectric constants could be finally written into the following format and are fitted to the data. [60]

$$\varepsilon'_{EP} = \varepsilon_R + \frac{\Delta\varepsilon_{EP}}{1 + \omega^2\tau_{EP}^2} = \frac{M\varepsilon_R + \omega^2\tau_{EP}^2\varepsilon_R}{1 + \omega^2\tau_{EP}^2} \quad (2.28)$$

$$\varepsilon''_{EP} = \frac{\Delta\varepsilon_{EP}\omega\tau_{EP}}{1 + \omega^2\tau_{EP}^2} = \frac{\varepsilon_R(M-1)\omega\tau_{EP}}{1 + \omega^2\tau_{EP}^2} \quad (2.29)$$

A schematic plot of the EP relaxation is shown in Figure 2-21. [60]

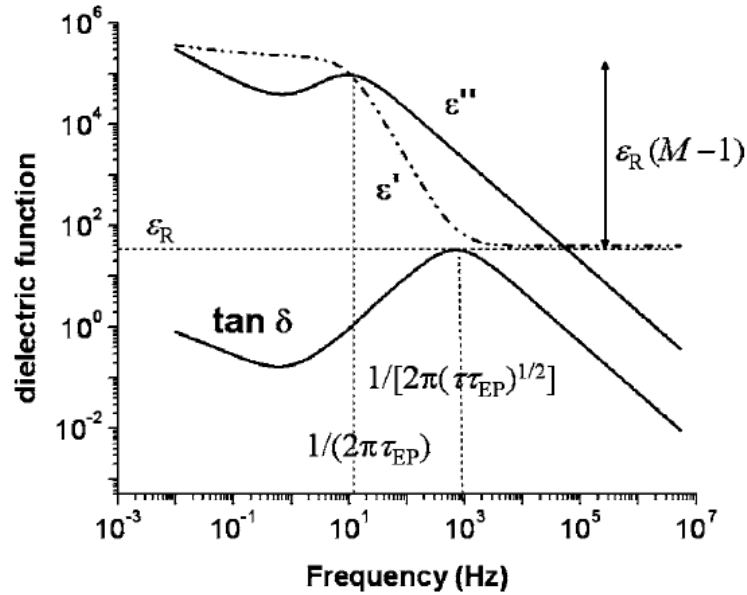


Figure 2-21 Schematic plot of the EP relaxation in ε' , ε'' , and $\tan \delta$ for a conductive system, with peak frequencies, dielectric relaxation strength, and ε_R denoted. [60]

The simple R-C equivalent circuit that was introduced in the previous section, indeed, is similar to the EP model in describing the ionic polymer membranes. To deduce the dielectric constants from the equivalent circuit model in Section 2.3.2.2, one can first convert the Z' and Z'' into dielectric constants by the following relation.

$$(\varepsilon'_{EP} + j\varepsilon''_{EP}) \frac{A}{L} = \frac{1}{-j\omega(Z' + jZ'')} \quad (2.30)$$

Hence, we have

$$\varepsilon'_{EP} = \frac{LZ''}{\omega A(Z'^2 + Z''^2)} \quad (2.31)$$

$$\varepsilon''_{EP} = \frac{LZ'}{\omega A(Z'^2 + Z''^2)} \quad (2.32)$$

From equations (2.22)-(2.24) and equations (2.31)-(2.32) and by defining $M = L / 2L_D$, $\tau = \varepsilon / n_0 e \mu$, and $\tau_{EP} = M\tau$, dielectric constants in the equivalent circuit model could be further written into the following expressions (Here dielectric contribution of the entire sample is added as ε_R),

$$\varepsilon'_{EP} = \frac{M\varepsilon_R}{1 + \omega^2 \tau_{EP}^2} + \varepsilon_R \quad (2.33)$$

$$\varepsilon''_{EP} = \frac{\varepsilon_R M \omega \tau_{EP}}{1 + \omega^2 \tau_{EP}^2} \quad (2.34)$$

By comparing the expressions of dielectric constants from the EP model (equations (2.28) - (2.29)) and the equivalent circuit model (equations (2.33) - (2.34)), it can be found that under certain limits, such as $M \gg 1$, these two models (equations (2.28) - (2.29)) and (equations (2.33) - (2.34)) are the same. For the ionic polymer membrane actuators studied in this dissertation, M is in the range of 10^4 and τ_{EP} is in the range of 10^{-4} s,[58] so that the EP model and the R-C equivalent circuit are approximately the same for the frequencies of interest ($f < 10^5$ Hz). Further

discussion of the impedance analysis will be continued in Chapter 3 and 4, where an improvement in equivalent circuit modeling will be introduced.

2.3.2.4 Potentiostatic method

Besides impedance spectroscopy, which is a frequency domain analysis, a time domain analysis, where the charge responses under a step voltage are measured, can also be utilized to understand the charging process shown in Figure 2-20. [58, 63] To clearly illustrate the charge dynamics, Figure 2-22 schematically shows the ion distribution without and with a voltage bias.

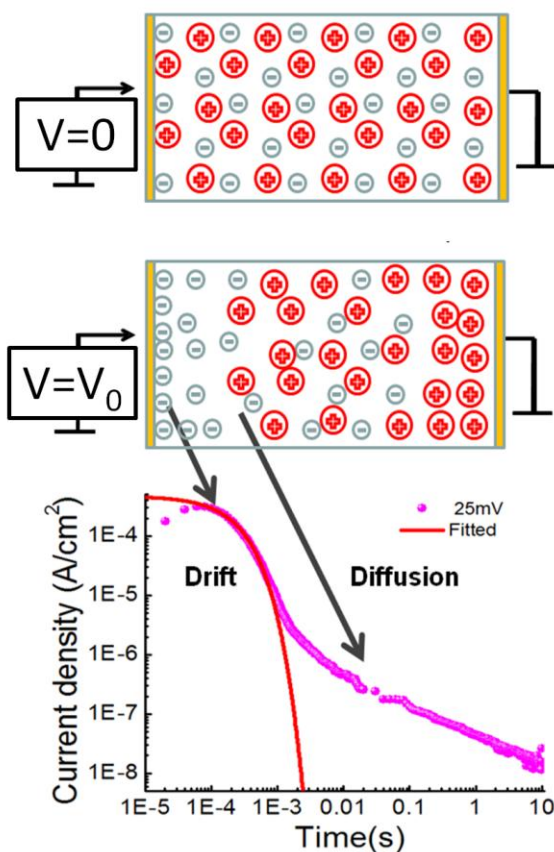


Figure 2-22 Schematics of an ionic polymer membrane sandwiched between planar metal electrodes under a step voltage. When the voltage rises from zero to V_0 , ions drift and diffuse towards the electrodes with opposite polarity.[58]

In general, charge transport of ionic system with planar blocking electrodes is a result of drift and diffusion, and for dilute solution, they can be described by Poisson-Nernst-Planck (PNP) equations, [64]

$$-\nabla(\varepsilon \nabla \phi) = \rho \quad (2.35)$$

$$\frac{\partial n_i}{\partial t} - \nabla \left[D_i \left(\nabla n_i + \frac{z_i e n_i}{k_B T} \nabla \phi \right) \right] = 0 \quad (2.36)$$

where ε is the dielectric constant, ϕ is the electric potential, z_i is the valence, n_i is the concentration, and D_i is the diffusion coefficient. These PNP equations are deduced from Poisson equation and conservation of mass equation with a few approximations, such as no convective transport ($\vec{u} = 0$), no electrostatic correlations ($D_i = \text{const}$ and $\mu^{\text{excess}} = 0$ (μ^{excess} is the contribution of ion-ion correlation on the chemical potential)), and substitution of local ion concentration with mean ion concentrations, which are only valid for dilute solutions.

As mentioned in Section 2.3.2.2, the steady state limit of the PNP equations give Poisson-Boltzmann (PB) equation,

$$-\varepsilon \nabla^2 \phi = \sum_i z_i e \nu_i n_0 \exp\left(-\frac{z_i e \phi}{k_B T}\right) \quad (2.37)$$

where ν_i is stoichiometric coefficient, and for small potentials ($|\phi| < k_B T/e$), the PB equation can be linearized into Debye-Huckel equation, which gives Debye screening length λ_D ;

$$\lambda_D^2 \nabla^2 \phi = \phi \quad \lambda_D^2 = \frac{\varepsilon k_B T}{\sum_i (z_i e)^2 \nu_i n_0} \quad (2.38)$$

therefore, λ_D becomes an important characteristic length of these aforementioned ionic systems.

Ideally, in the case of concentrated solutions or solids, the flux expression in Eqn. 2.36 should be revised to account for the excess chemical potential and the dependence of the diffusivity on concentration, and the Poisson equation may also require modification to go

beyond the mean field approximation. However, Lin and Zhang [63] experimentally showed that when the perturbation to the ion concentration is small (small voltage or short time scale), even highly concentrated ionic liquids respond linearly to the applied electric field and the 1-dimensional PNP equations can still be adopted to analyze ion transport. It should be noted that under a large voltage (high field), this approximation is not true, which will be intensively discussed in Chapter 5.

$$\varepsilon \frac{\partial E}{\partial x} = \rho \quad (2.39)$$

$$\frac{\partial n_{\pm}}{\partial t} = \pm \mu n_{\pm} E - D_{IL} \frac{\partial n_{\pm}}{\partial x} \quad (2.40)$$

where ρ is the charge concentration, D_{IL} is the diffusion coefficient, μ is the ion mobility, n is the ion concentration (the subscripts + and – indicate positive and negative charges), E is the electric field, and D_{IL} is the diffusion coefficient. For the ionic liquids studied here, we assume $n_{+}=n_{-}$ for the simplicity of analysis. Since the perturbation to the concentration is very small, this approximation works in previous analysis [63, 65, 66]

For the ionic polymer membrane actuator with ionic liquids under a step voltage (Figure 2-22), the initial transient current that occurs before the screening of the electric field is $I_0=V/R$. When the applied voltage is not high, this current follows the charging of the electric double layer capacitors C_{dl} in series with a bulk resistor R as introduced in Section 2.3.2.2 (Figure 2-20), [58, 63, 67, 68]

$$I(t) = I_0 \exp(-t / \tau_{dl}) \quad (2.41)$$

where $\tau_{dl} = RC = RC_{dl} / 2$, $I_0 = qn\mu V / d = \sigma E$.

By fitting the experimental transient current $I(t)$ with equation (2.41), as illustrated in Figure 2-22, σ and τ_{dl} can be obtained. When the static dielectric constant ε of the ionic

polymer membrane is known, the mobile ion concentration n , and the mobility μ can also be obtained by the following relation, [63, 68, 69]

$$\mu = \frac{qVS\epsilon_0 d}{4kT\tau_{dl}^2 I_0} \quad (2.42)$$

$$n = \frac{4kTI_0^2 \tau_{dl}^2}{\epsilon_0 q^2 V^2 S^2} \quad (2.43)$$

It can be further shown that at longer time, the charge diffusion from the bulk to the double layer region leads to a power law decay of the diffusion current (see Figure 2-22, in which the initial current fits well by equation (2.41), followed by a power law decay of the diffusion current.)[58]

Chapter 3

IPCNC Actuators with Disordered CNC Nanomorphology

3.1 Introduction

As introduced in Chapter 1, CNCs increase the surface area of the electrodes, so they attract more ions and cause larger bending magnitude. In this chapter, IPCNC actuators made with ionomer/nanoparticle composites are discussed extensively. To understand the physics of these IPCNC actuators and thus improve the device performance, a couple of electrical and electromechanical models are developed. In Section 3.3.1, new equivalent circuits are built to describe how drift and diffusion charges affect the bending actuation. In Section 3.3.2, a two-carrier model is developed to explain the back relaxation in the IPCNC actuators and its effect on the electromechanical energy efficiency.

3.1.1 Actuation magnitude and speed

IPCNC actuators are complex systems that their bending actuation is affected by many factors, including overall actuator structure, thickness and Young's modulus of each layer, and properties of electrolyte and polymer matrix. As introduced in Chapter 1, there are various methods to fabricate CNCs, such as chemical reduction method, Layer-by-layer self assembly (LbL), and direct assembly process (DAP). Actuation curvatures of different IPCNC samples over time with step voltage are plotted in the following figures. Usually, with the same CNC fabrication method, it is found that the initial response (i.e. $t < 10\text{s}$) of IPCNC actuators

progressively increases with the CNC thickness, where LbL CNC ranges from 0-80 nm or DAP CNC ranges from 0 to 13 μm , as shown in Figure 3-1 and Figure 3-2.

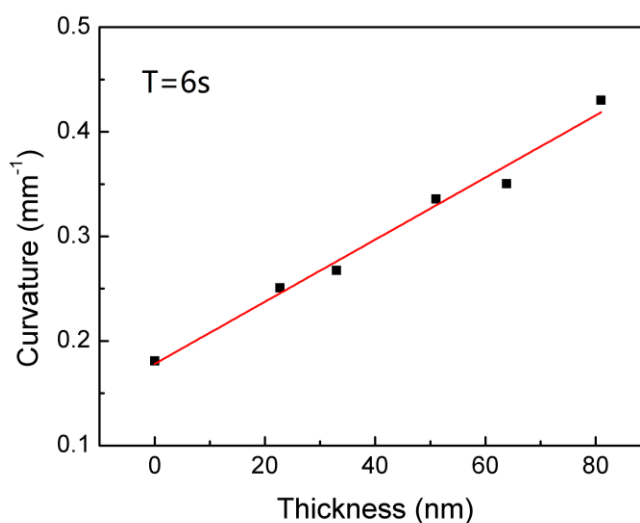


Figure 3-1 Bending curvatures of 25 μm Nafion with 0-80 nm PAH/Au CNCs that are fabricated via LbL method. Curvature increases linearly with the thickness of CNC. Data are taken under application of 4 V step function. (Redrawn from reference [70])

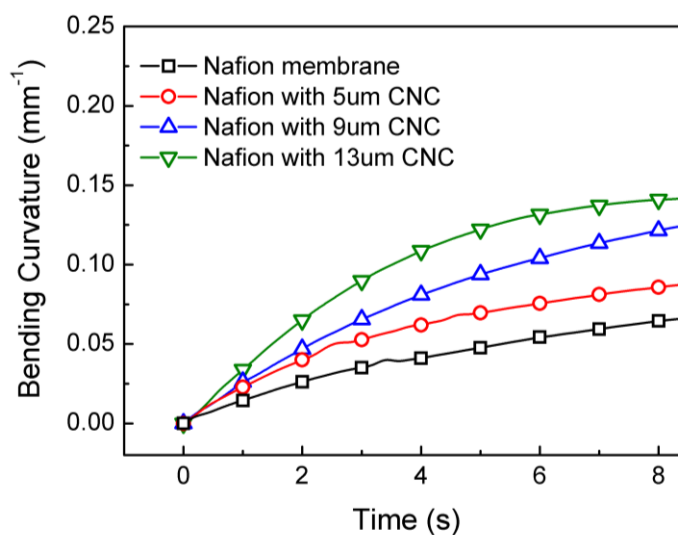


Figure 3-2 Bending curvatures (short time) of 50 μm Nafion with 0-13 μm Nafion/RuO₂ CNCs that are fabricated via DAP method. Data are taken under application of 4 V step function. Nafion with 20 μm Nafion/RuO₂ CNCs (not shown) start to show much slower actuation due to high resistance in the CNC. (Collaboration with Francis Richey at Drexel University)

On the contrast, the long time actuation (i.e. $t > 10s$) of IPCNC actuators exhibits a complicated dependence on the CNC thickness, as an example shown in Figure 3-3. The data also reveals that under a step voltage, the actuation cannot sustain a stable bending magnitude. In fact the bending actuation reverses the direction at large time scale for step and DC operations, which is the major disadvantage of *i*-EAP actuators introduced in Chapter 1.

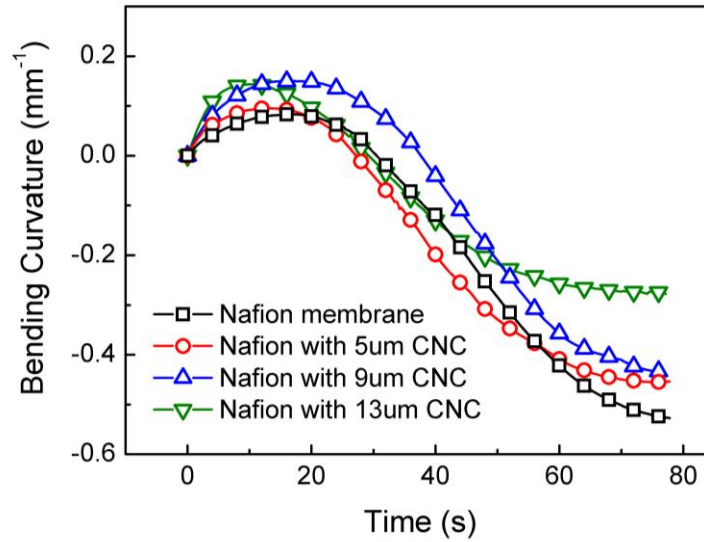


Figure 3-3 Bending Actuation (long time) of 50 μm Nafion with 0-13 μm Nafion/ RuO_2 CNCs that are fabricated via DAP method. Data are taken under application of 4 V step function. Nafion with 20 μm Nafion/ RuO_2 CNCs (not shown) start to show much slower actuation due to high resistance in the CNC. (Collaboration with Francis Richey at Drexel University)

In this chapter, an in-depth analysis of the IPCNC actuation will be presented to understand the behaviors shown in Figure 3-1, 3-2, and 3-3, by dividing the actuation into two time ranges: initial response ($t < 10s$) and long time response ($t > 10s$). Furthermore, although CNCs fabricated by different methods (LbL and DAP) show similar trends in initial bending response (Figure 3-1 and 3-2), due to their different electrical and mechanical properties, it is hard to compare their performance from the bending curvature directly. Therefore, in the literature, these devices were evaluated with their maximum intrinsic strain S_{0max} (S_0 is introduced in Chapter 2

Section 2.3.1.2) and the time constant τ to reach this S_{0max} . The time constant τ of initial response is determined with the following equation.[28]

$$S_0(t) = S_{0max} (1 - e^{-t/\tau}) \quad (3.1)$$

Previous studies found that the PAH/Au CNCs made with LbL method, gives a larger maximum intrinsic strain $S_{0max}=6.8\%$ and a smaller time constant $\tau=0.18$ s than those of the Nafion/RuO₂ CNCs made with DAP method (3.3% and 1.03s). [28] The difference in time constants are mainly resulted from the difference in thickness of the CNCs, which will be modeled and discussed by equivalent circuits in Section 3.3.1 of this chapter.

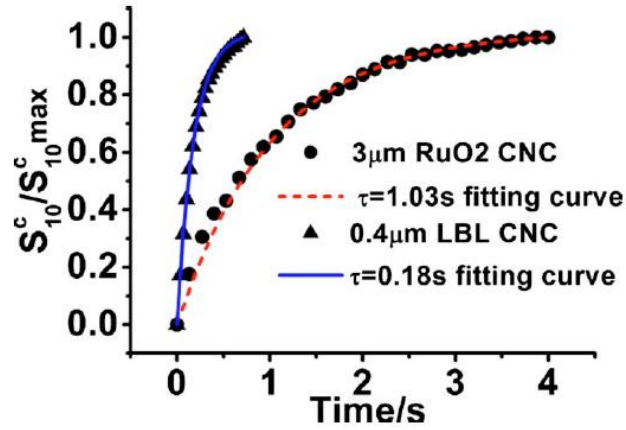


Figure 3-4 The actuator response as a function of time under a step voltage for 25 μm Nafion with 400 nm PAH/Au CNCs and 25 μm Nafion with 3 μm Nafion/RuO₂ CNCs. [28]

3.2 IPCNC Fabrication and Characterization

Two groups of IPCNCs are studied in this chapter, which include IPCNCs fabricated with NafionTM and AquivionTM ionomers via the direct assembly process (DAP) [27, 71] and IPCNCs by the Layer-by-Layer (LbL) self assembly method.[28, 71, 72].

3.2.1 Layer-by-layer (LbL) self assembled CNCs

The IPCNCs with LbL composites in this chapter were fabricated by alternately immersing the Nafion NR-211 film (Aldrich) into two aqueous solutions containing PAH as the polycation and anionic Au nanoparticles (3 nm diameter, Purest Colloids Inc.) or Carbon nanotubes (CNTs) (from Carbon Solutions Inc.) for certain number of cycles. The composites grew via the electrostatic force between PAH and the Au nanoparticles. [28, 71] The LbL CNCs in this chapter comprise 30 bilayers (64nm) of PAH/Au, 100 bilayers (180nm) of PAH/Au and 30 bilayers (400nm) of PAH/CNT, respectively. The lateral dimensions of the IPCNCs studied were 1 mm x 8 mm with tens of nm thick CNC on each side and a total thickness of approximately 25 μm . [70]

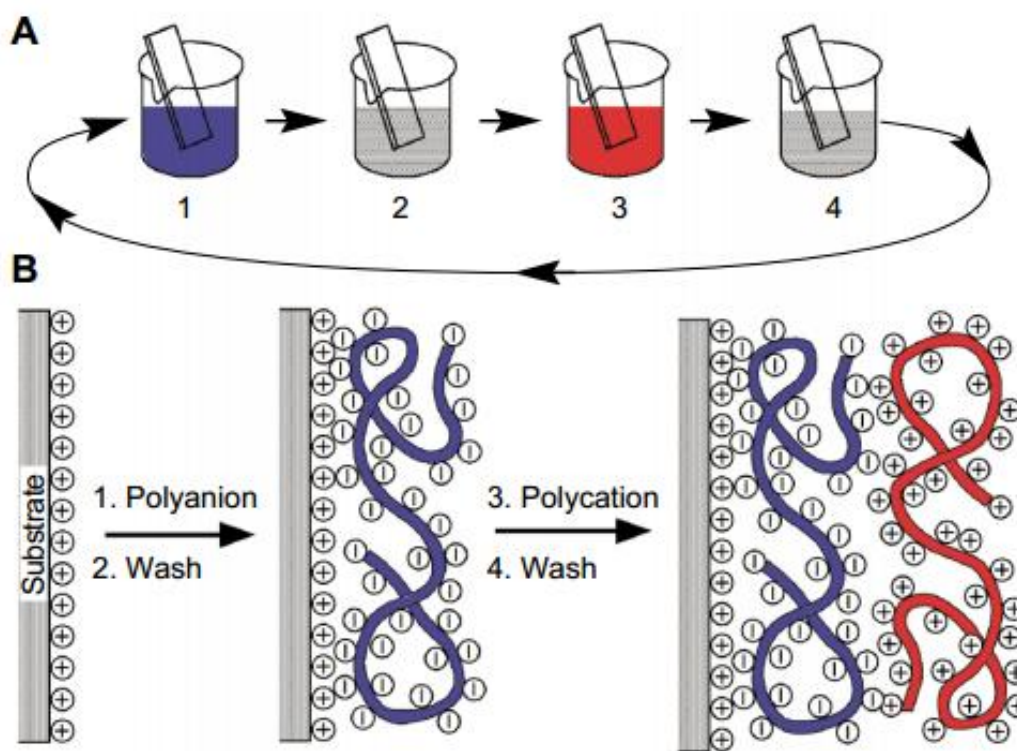


Figure 3-5 Schematic of the layer-by-layer assembly deposition process using slides and beakers. Steps 1 and 3 represent the adsorption of a polyanion and polycation, respectively, and steps 2

and 4 are washing steps. The four steps are the basic buildup sequence for the simplest film architecture. [72]

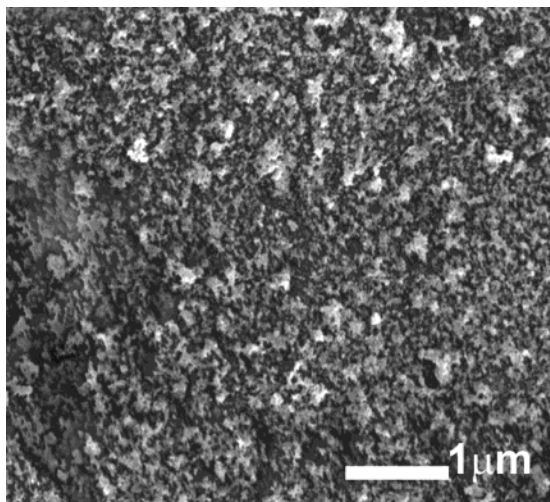


Figure 3-6 SEM of the PAH/Au CNC studied in this chapter[43]

3.2.2 Direct assembly process (DAP) CNCs

For the IPCNCs fabricated with the directly assembly method, the fabrication process here partially followed the DAP steps in Figure 3-7. Either 25 μm thick commercial Nafion film NR-211 from Aldrich (or Aquivion film 79-03 from Solvay) was chosen as the spacer layer, which was briefly introduced in Chapter 1 Section 1.2. Nafion/RuO₂ (or Aquivion/RuO₂) composite was fabricated by mixing RuO₂ nanoparticles (from Alfa Aesar with 13-19 nm diameter) with 20 wt% Nafion dispersion from Aldrich (or 20 wt% Aquivion dispersion from Solvay). Since the percolation threshold of the electrode is around 20 vol% of RuO₂, [27] a CNC layer with 40 vol% of RuO₂ nanoparticles was used to ensure good electrode conductivity. The mixture was then sonicated and sprayed onto the two surfaces of Nafion (or Aquivion) film. After spraying, these films were transferred to vacuum oven to remove the solvent and annealed at 130°C for one hour. 3 μm of Nafion/RuO₂ (or Aquivion/RuO₂) CNCs was coated and studied in this chapter. An SEM of as-made Nafion/RuO₂ CNC is presented in Figure 3-8.

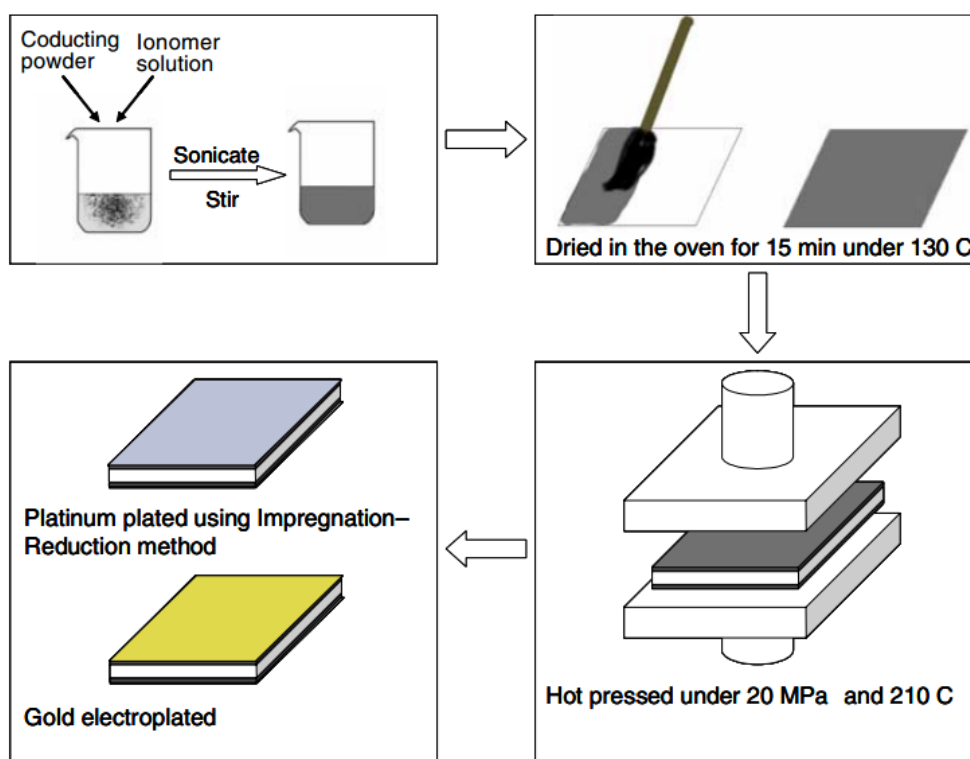


Figure 3-7 Schematic showing the four steps Direct Assembly Process (DAP) for building dry transducers[27]

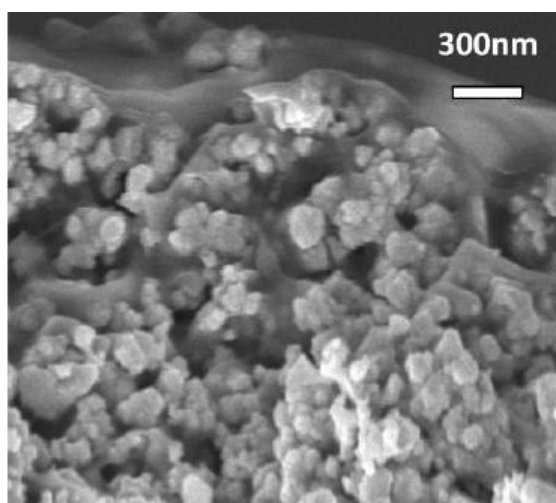


Figure 3-8 SEM of the Nafion/RuO₂ CNC served in this chapter[43]

3.2.3 Actuator fabrication and characterization

In this chapter, 40 wt% of ionic liquids, 1-ethyl-3-methylimidazolium trifluoromethanesulfonate (EMI-Tf) or 1-ethyl-3-methylimidazolium tetrafluoroborate (EMI-BF₄), as shown in Figure 3-9 and Table 3-1, was soaked into Nafion (or Aquivion) ionomer membranes or IPCNC actuators at 60 °C. The uptake of the ionic liquids within the ionomer membrane or IPCNC actuators was calculated from measuring the weight gain after swelling. After achieving a 40 wt% uptake, 50 nm thick gold electrodes (L. A. Gold Leaf) were hot-pressed on two sides of the actuator surfaces to increase the surface conductivity.

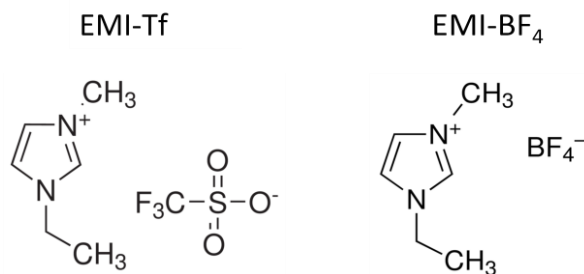


Figure 3-9 Chemical formulae of the ILs 1-ethyl-3-methylimidazolium trifluoromethanesulfonate (EMI-Tf) and 1-ethyl-3-methylimidazolium tetrafluoroborate (EMI-BF₄) that were utilized in this dissertation

Table 3-1 Properties of the ILs that were utilized in this chapter

Name	Molecular Weight (g/mol)	Density (g/cc)	Melting Point (°C)	Ionic Conductivity (S/cm)
EMI-Tf	260.23	1.381	-12	7.7
EMI-BF ₄	197.97	1.304	14	11.4

The electrical characteristics were measured in air by a potentiostat (Princeton Applied Research 2273) with 2-electrode settings as shown in Chapter 2 Section 2.2.1. In terms of actuation, a DC step voltage was applied on the IPCNC samples and the time resolved electromechanical response of the actuators in air was recorded by using a probe station (Cascade

Microtech M150) equipped with a Leica microscope and a CCD camera (Pulnix 6740CL), as shown in Chapter 2 Section 2.2.3.

3.3 Results and Discussion

3.3.1 Equivalent circuit modeling and analysis

In the past decades, great efforts have been devoted to investigate the charge dynamics in ionic electroactive devices, such as *i*-EAP actuators and supercapacitors. As introduced in Chapter 2 Section 2.3.2.3, the EP model, [60] based on the analysis of electric impedance spectra of ion containing membrane, has been used to describe the electric double layer in ionic polymer membrane, which generally forms within milliseconds [58] and is on the order of nanometer thickness near the charged electrodes (\sim the Debye length L_D). As further derived in Chapter 2 Section 2.3.2.3, within the frequency range of interest, this EP model can be expressed schematically as a simple R-C circuit, where $R=d/\sigma S$ and $C=C_{dl}=\epsilon\epsilon_0 S/L_D$. Here, d , σ , and S are the thickness, conductivity, and the area of the ionomer membrane actuator, respectively.

In this section, it will be shown that although this simple EP model can fit the data for the ionomer membrane actuator well at frequencies above 1 kHz, it cannot describe the low frequency response of ions or ion containing polymeric systems under electric stimulus. In fact, the electromechanical responses of *i*-EAP actuators usually occur at this low frequency range, specifically, at frequencies below 10 Hz.

Presented in Figure 3-10 are bending actuations of Nafion and Nafion with LBL PAH/Au IPCNC actuator after application of 4 volts. It can be seen that the bending actuation significantly increase over a few seconds and the both the bending actuation and the actuation speed increase with CNC. In this section, new equivalent circuit models will be established to analyze the

electric impedance spectra of ionic polymer actuators with and without CNCs, which leads to an in-depth understanding of the charge dynamics in the ionic polymer membrane and the contribution of the CNCs.

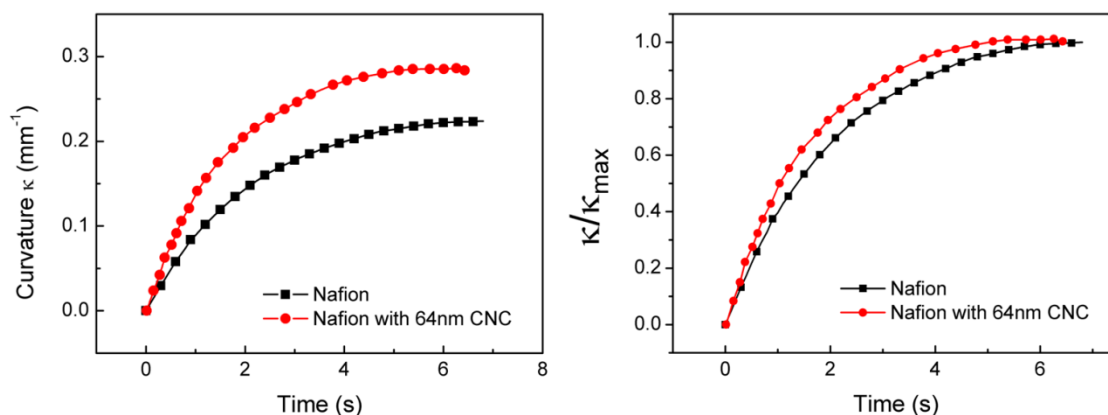


Figure 3-10 Bending actuations of Nafion and Nafion with LBL PAH/Au IPCNC actuator

The actuators studied with the new equivalent circuit models include (i) an ionomer membrane actuator consisting of a 25 μm thick Nafion membrane with planar Au electrodes and swelled with 40 wt% of EMI-Tf, referred to as the “Nafion membrane actuator” and two state-of-the-art IPCNC actuators fabricated by (ii) a layer-by-layer (LbL) self-assembly process and swelled with 40 wt% EMI-Tf, referred to as the “LbL actuator”, and (iii) direct assembly process (DAP) and swelled with 40 wt% EMI-Tf, referred to as the “DAP actuator”. Compared to the simple membrane actuator (i), the IPCNC in (ii) and (iii) possess larger electrode surface areas, and thus exhibit higher bending actuations, as shown in Figure 3-10. The actuator dimensions are summarized in Table 3-2.

Table 3-2 Summary of dimensions of Nafion membrane actuator and LbL actuator

	Width	Length	Membrane thickness	CNC thickness	Total thickness
Nafion	1 mm	8 mm	25 μm	0 μm	25 μm
LbL	1 mm	8 mm	25 μm	0.064 μm	25.13 μm

In order to quantify the low frequency ionic responses (diffusion process), which dominates the actuation response in Figure 3-10, the Warburg impedance element, a constant phase element (CPE) that is commonly used to represent diffusion controlled charge transfer process in pseudo-capacitors, should be added to the EP circuit elements, as illustrated in Figure 3-11.

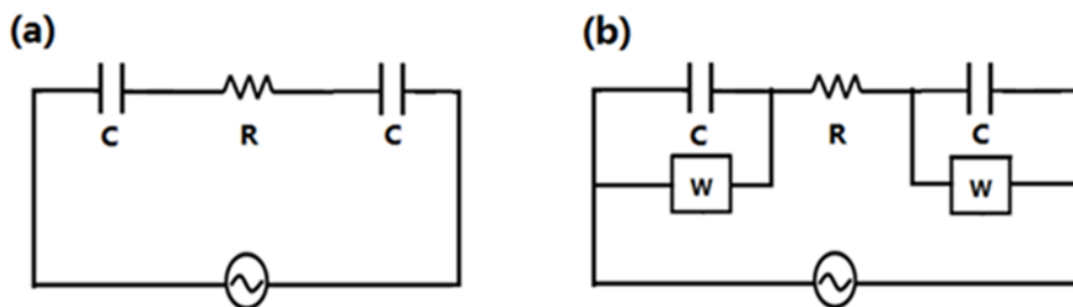


Figure 3-11 (a) RC equivalent circuit and (b) Equivalent Circuit with Warburg element

Although compared to a pseudo-capacitor, an ionomer or IPCNC with ILs has little red-ox reaction under low voltage (~ 0.1 V), it has been shown in Chapter 2 Section 2.3.2.4 that the ion diffusion dominates the electric response above the time scale of milliseconds. [58] Therefore, it will be demonstrated that the equivalent circuit with Warburg impedance element can fit the impedance spectra for ionic polymer membranes with ILs very well in the entire frequency range. Moreover, it is found that the equivalent circuit with Warburg impedance element can also be used to fit the impedance spectra for IPCNC actuator systems with thin CNC layer such as LbL actuators, which have CNC layer thickness ~ 64 nm.

3.3.1.1 The ionomer membrane actuator

Despite the actual data as markers, dashed curves presented in Figure 3-12(a) and (b) are the fittings of the electric impedance magnitude and phase of the Nafion membrane actuator using the simple R-C circuit model (Figure 3-11(a)). It is obvious that although the model can fit the impedance spectrum well at frequencies above 100 Hz, it deviates significantly from the data at lower frequencies. It should be noted that the resistive element R can be easily determined from the real part of impedance data at high frequencies (>50 kHz) where the imaginary part of the impedance is related to the electric double layer capacitor element C_{dl} , as introduced in Chapter 2 Section 2.3.2.2.

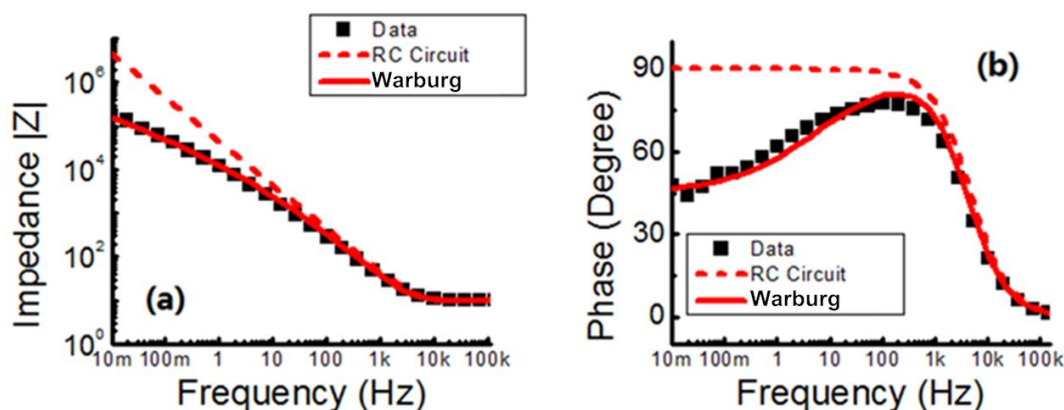


Figure 3-12 (a) Impedance magnitude and (b) Phase of Nafion with 40 wt% EMI-Tf fitted by simple RC circuit and Equivalent Circuit with Warburg element

The fitting with simple R-C circuit (dashed curves in Figure 3-12) implies that the low frequency response of this system intrinsically differs from the behaviors of either resistors or capacitors. A diffuse layer continuously contributes to the charging and discharging current so that the system behaves more lossy than an ideal R-C circuit. To describe the contribution of the diffuse layer, a Warburg element [73-75] is introduced in parallel with the electric double layer capacitance C_{dl} in Figure 3-11(b), as the total stored charge is the sum of the electric double layer

charges and the diffuse layer charges. [63] The diffusion process here is assumed as a semi-infinite linear diffusion, that is, unrestricted diffusion to a planar electrode. The Warburg element has an explicit expression as $Z_W = A_W/(j\omega)^{0.5}$, where A_W is the Warburg coefficient (Appendix C). [73-75] A much improved fitting (solid curves) from the equivalent circuit with the Warburg element (Figure 3-11(b)) is presented in Figure 3-12(a) and (b), where the electric double layer capacitance C_{dl} is $7.5 \mu\text{F}/\text{cm}^2$, the bulk resistance R is $9.7 \Omega \times \text{cm}^2$ and the Warburg coefficient A_W is $10^5 \Omega \times \text{cm}^2 \text{s}^{-1/2}$, respectively.

To demonstrate the dominance of the diffusion contribution to the charging and actuation response, Nyquist plot is presented in Figure 3-13. It is clear that at low frequencies, the Nyquist plot of the ionic polymer membrane has a 45 degree phase angle, indicating the dominance of the Warburg impedance over the electric double layer capacitance.

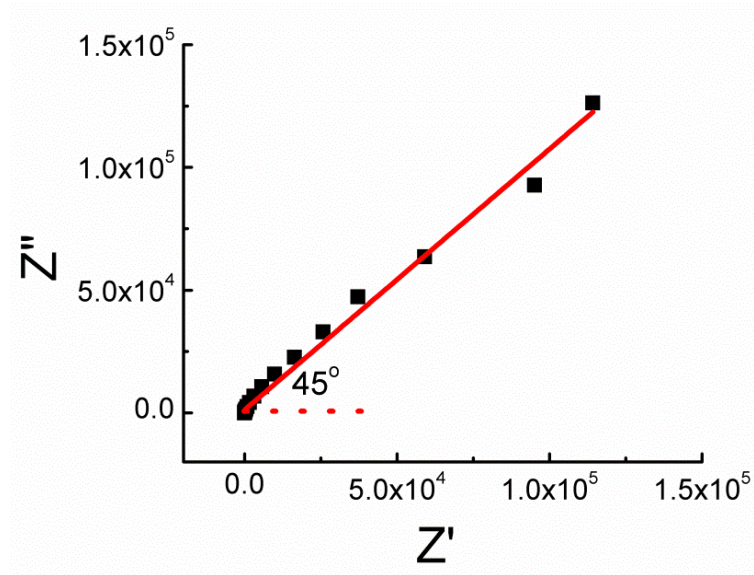


Figure 3-13 Nyquist Plot of Nafion with 40 wt% EMI-Tf

Meanwhile, from the time domain analysis introduced in Chapter 2 Section 2.3.2.4, the fitting of the initial current of the Nafion membrane actuator yields a $\tau_{dl} = 2.66 \times 10^{-4} \text{ s}$ and $C = 3.5 \mu\text{F}/\text{cm}^2$, since R can be independently determined from I_0 . This result is consistent with the

capacitance fitted from the impedance spectroscopy, where C is the total capacitance of the electrical double layer capacitance C_{dl} at two electrolyte-electrode interfaces.

3.3.1.2 The IPCNC actuator via LbL self assembly

To enhance the performance of ionic polymer membrane actuator, as introduced in Chapter 1 Section 1.2 and Chapter 3 Section 3.1, CNC are coated on the membrane to increase the electrode surface area, and hence the ion storage for strain generation. Previous studies (introduced in Chapter 3 Section 3.1) showed that the actuation magnitude gradually increases with CNC thickness, when the CNCs are fabricated by LbL or DAP methods. [70]

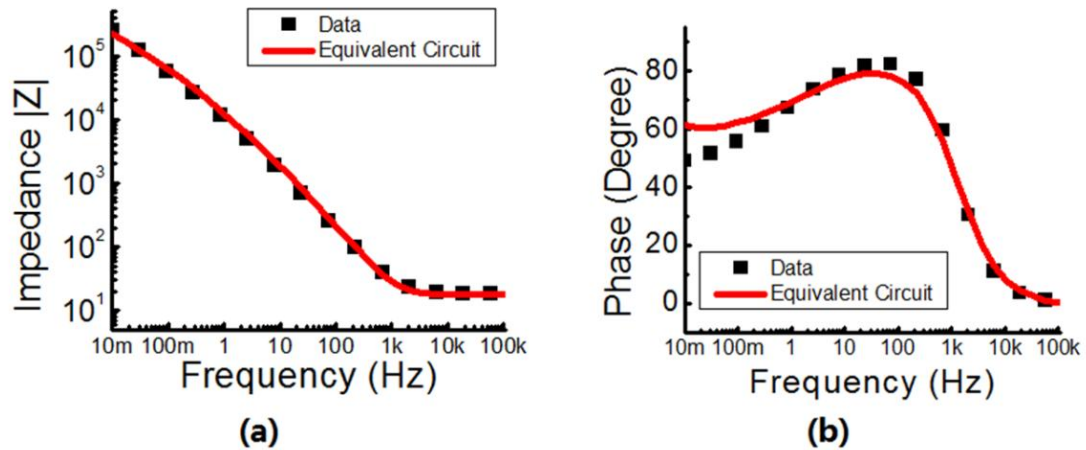


Figure 3-14 (a) Impedance magnitude and (b) phase of Nafion with 64 nm LbL PAH/Au composite actuator (contain 40 wt% of EMI-Tf)

Figure 3-14 (a) and (b) show the fitting of impedance and phase of a LbL IPCNC actuator with 64nm CNC. All the fitting parameters for membrane actuator and LbL actuator are summarized in Table 3-3.

Table 3-3 Fitting parameters for ionic polymer actuators

	$C_{dl}(\mu\text{Fcm}^{-2})$	$R(\Omega\text{cm}^2)$	$A_w(\Omega\text{cm}^2\text{s}^{-1/2})$
Nafion	7.5	9.7	1×10^5
	$C_{dl}(\mu\text{Fcm}^{-2})$	$R(\Omega\text{cm}^2)$	$A_w(\Omega\text{cm}^2\text{s}^{-1/2})$
LBL	11.4	18.1	1.1×10^5

For the LbL actuators, it was found that the equivalent circuit of Figure 3-10 (b) can fit the data well in the entire frequency range and returns meaningful fitting parameters, which indicates that the contribution of the charge transport within the composite electrodes to the actuation is negligible due to the thinness of the CNC layer (~ 64 nm). However, the significantly increased capacitance C_{dl} ($11.4 \mu\text{Fcm}^{-2}$) results in a large increase in the actuation, while A_w ($1.1 \times 10^5 \Omega\text{cm}^2\text{s}^{-1/2}$) is almost the same as that in Nafion membrane actuator. As a result, the actuation speed, which is directly driven by the ion migration, is improved due to the increase in fast actuation component, i.e., the electric double layer capacitance C_{dl} . It explains why LbL actuators can achieve fast response in Figure 3-10.

3.3.1.3 The IPCNC actuator via DAP

When the CNC layer grows thicker ($> \mu\text{m}$), although the simple equivalent circuit with Warburg element in Figure 3-11 (b) can still barely fit the experimental data (shown in Figure 3-15) with fitting parameters $C_{dl}=17.7 \mu\text{Fcm}^{-2}$, $R=12 \Omega\text{cm}^2$, and $A_w= 4160 \Omega\text{cm}^2\text{s}^{-1/2}$, these fitting parameters lose their physical meaning in modeling the IPCNC actuators.

In general, the CNC electrode here is electrically very similar to the porous electrodes used in the supercapacitors.[57, 76] The ion transport in porous electrodes, as shown by de Levie, is an electrical field driven diffusion process, and for uniform pores it can be modeled as a uniform R-C transmission line as illustrated in Figure 3-16. [57, 76, 77] When over-simplify this

transmission line circuit into a simple equivalent circuit with Warburg element, the complex R-C network is represented by only C_{dl} and A_w that leads to diminished values.

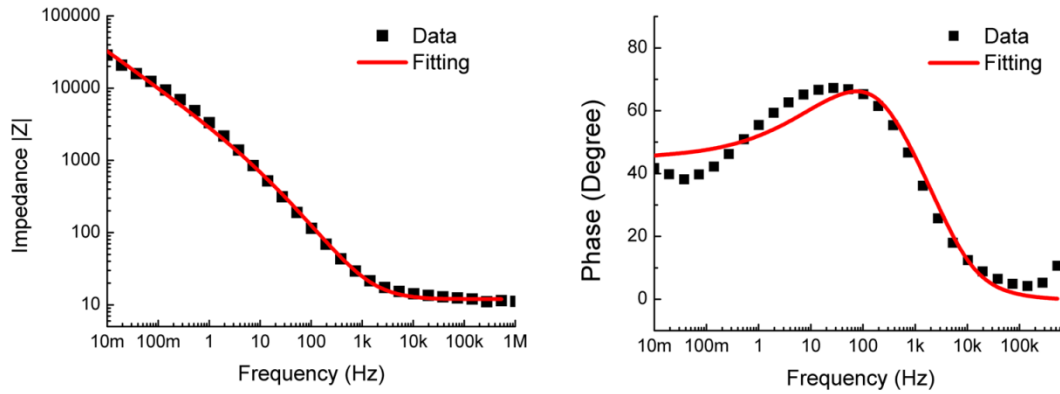


Figure 3-15 (a) Impedance magnitude and (b) phase of Nafion with 6 μm DAP Nafion/ RuO_2 composite actuator (contain 40 wt% of EMI-Tf).

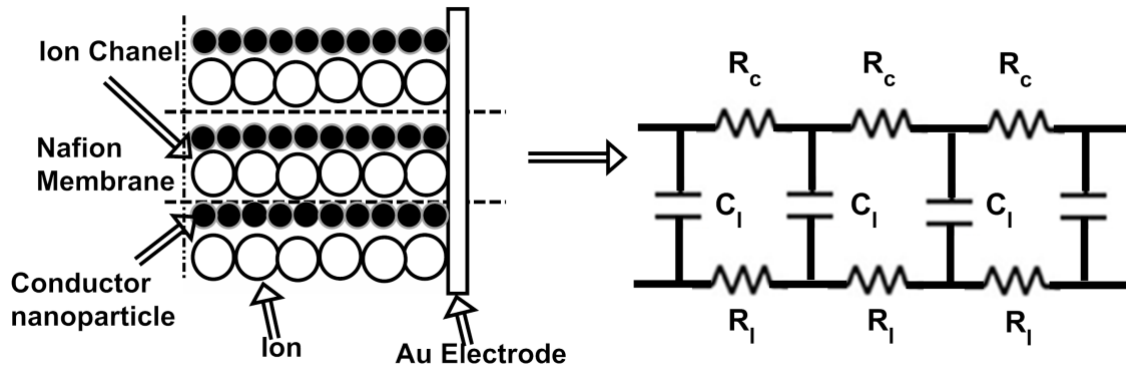


Figure 3-16 schematic for a transmission line model of the de Levie impedance

Presented in Figure 3-17 are the equivalent circuits of IPCNC actuators with various thicknesses of CNC layers, where the de Levie transmission line is adopted. In the figure, C_l is the unit length electric double layer capacitor formed at the electronic conductor and ionic conductor, W is the Warburg element, R_l is the unit length resistance of the ion transport in ionic conductor, and resistor R_c represents the imperfect electrical contact between the conductive nanoparticles.

In order for the CNCs to function as an effective porous electrode (low electronic resistance in the conductor network), R_C usually is much smaller than R_I . These equivalent circuits, precisely describe the physics of the CNC layers, however, they introduce too many fitting parameters that make the quantitative data fitting practically impossible.

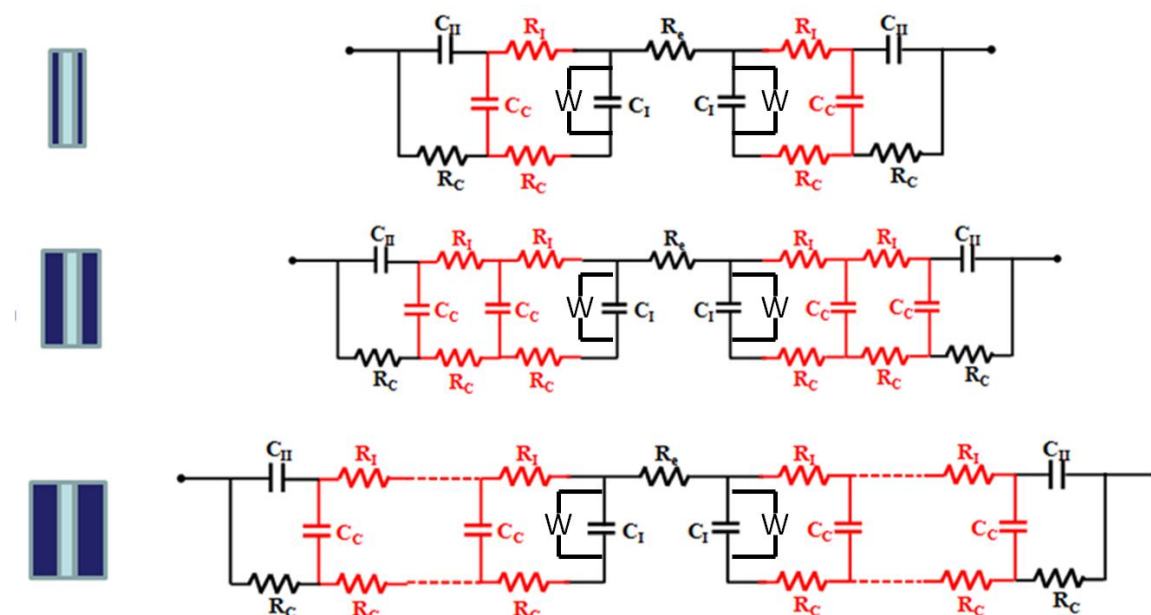


Figure 3-17 Schematic for equivalent circuits with de Levie transmission and Warburg element line for different CNC thickness

Qualitatively, under an applied voltage, excess ions enter (or leave) the CNC layer through the CNC/ionomer interface. Consequently, as indicated by the R-C transmission line model in Figure 3-17, the electric double layer C_I and Warburg diffusion layer W near the CNC/ionomer interface will be charged first and then the excess ions will progressively diffuse into the composite layer to charge the capacitors further away from the interface. Therefore, thick CNC layer intrinsically has a longer ion transport time, and this transport time constant, as the CNC thickness increase, overwhelms the original transport time of the Nafion membrane layer. This explains why thick CNC made with Nafion/RuO₂ (DAP) has a much slower response than

thin CNCs made with PAH/Au (LbL), as introduced in Section 3.1 (Figure 3-4). More equivalent circuit analysis will be presented in Chapter 4.

3.3.2 Electro-mechanical modeling (2-carrier model)

Different from the initial response of the Nafion membrane and IPCNC actuators ($t < 10$ s), which has been intensively discussed in the last section of this chapter, at large time scale ($t > 10$ s), ionic polymer actuators with ionic liquids, which consist of two types of mobile carriers: cations and anions, start to lose their performance and show back relaxations. Presented in Figure 3-18 is the evolution of the bending actuation of the PAH/Au IPCNCs with EMI-Tf under 4 V step voltage. The actuator initially bends towards the anode and as the time progresses, it reverses the actuation direction and bends towards the cathode. This phenomenon completely differs from the ionic polymer actuators with one type of mobile carriers, which only bends towards one direction under step voltage. Figure 3-19 shows the bending actuations of Nafion with two-carrier electrolyte and single-ion electrolyte, which shows that the back relaxation is caused by two carriers in ionic liquids. To understand the long time response of ionic polymer membrane and IPCNC actuators with ionic liquids, an electromechanical model is built and discussed in this section.

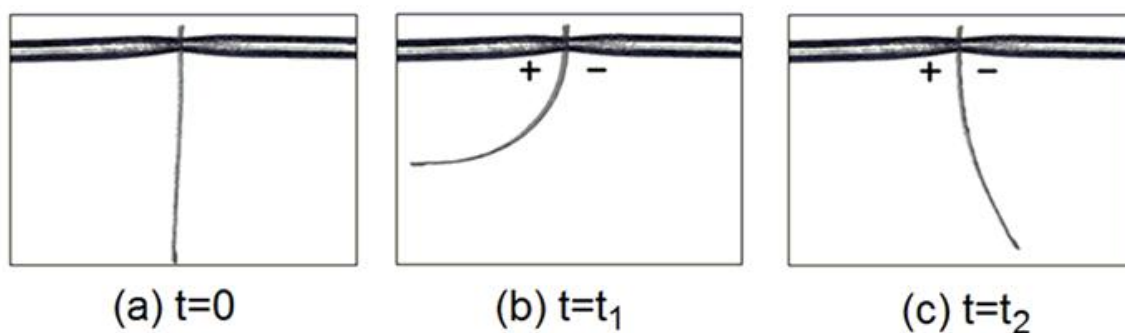


Figure 3-18 Bending actuation recorded at different times ($t_2 > t_1$) for the PAH/Au IPCNCs under 4V step voltage

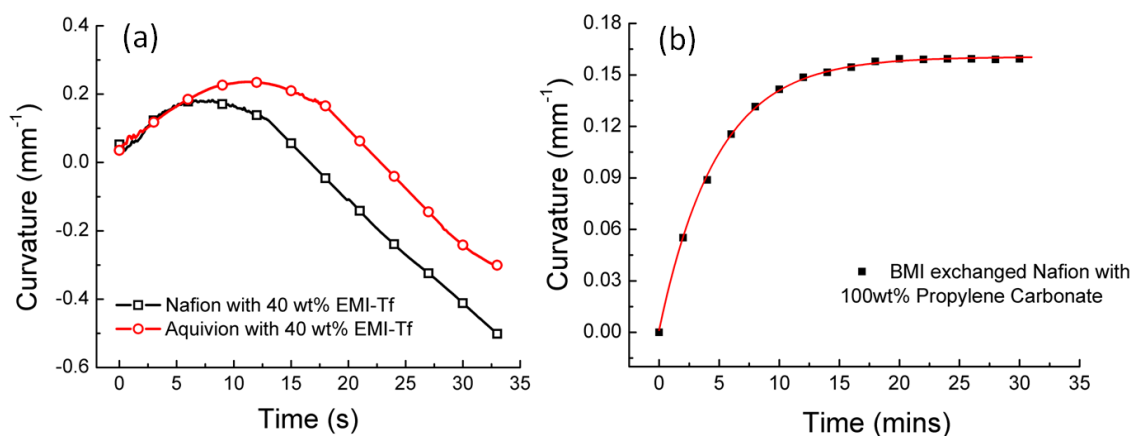


Figure 3-19 Bending actuations of (a) Nafion and Aquivion with ionic liquids EMI-Tf and (b) Nafion with BMI and Propylene Carbonate

From the introduction in Chapter 2 Section 2.3.1.2, the intrinsic strain S_0 generated in the composite electrode (CNC) layer is proportional to the bending curvature κ . It is found that for various IPCNC actuators studied in this section, the cathode expands at first and then the strain decreases (κ becomes small). For the data shown in Figures from 3-21 to 3-23, the strain at cathode finally becomes negative (κ changes sign). The charge density Q vs. time for these IPCNCs is also presented in Figures from 3-20 to 3-23.

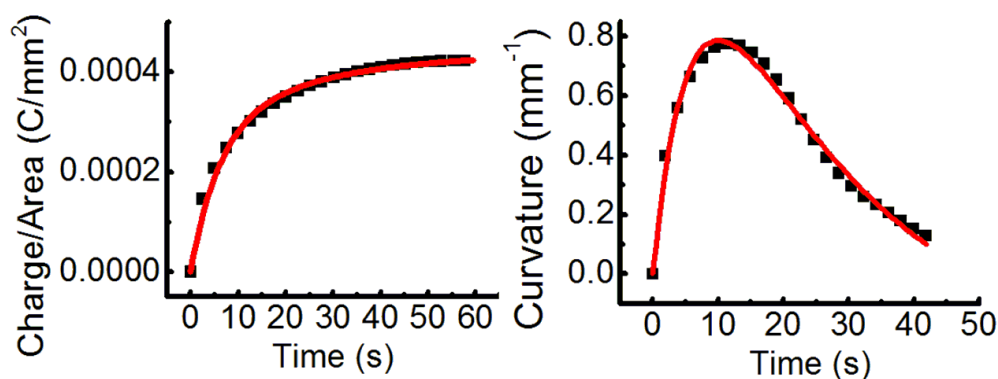


Figure 3-20 Data and fitting of charge and curvature vs. time for Nafion with 3 μm thick Nafion/RuO₂ composite electrodes at each side and EMI-BF₄ IL under 3V step voltage

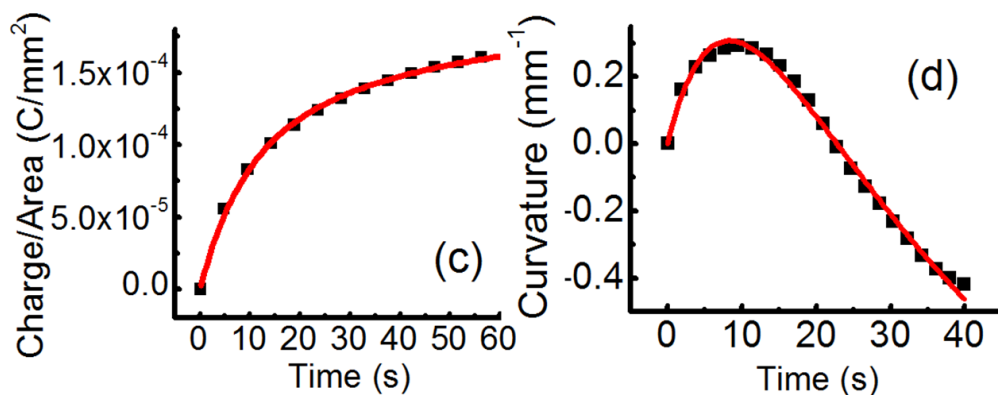


Figure 3-21 Data and fitting of charge and curvature vs. time for Aquivion with 3um Aquivion/RuO₂ composite electrodes and EMI-Tf IL under 3V step voltage

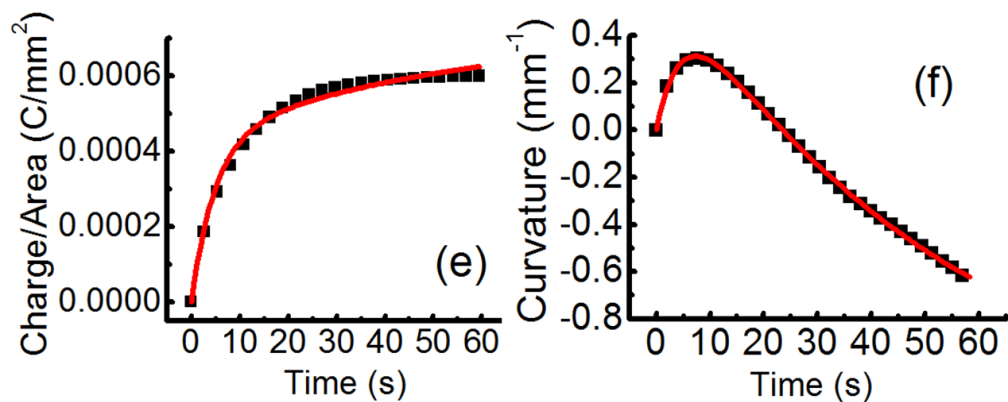


Figure 3-22 Data and fitting of charge and curvature vs. time for Nafion with 180 nm PAH/Au LbL composite electrodes and EMI-Tf IL under 4V step voltage

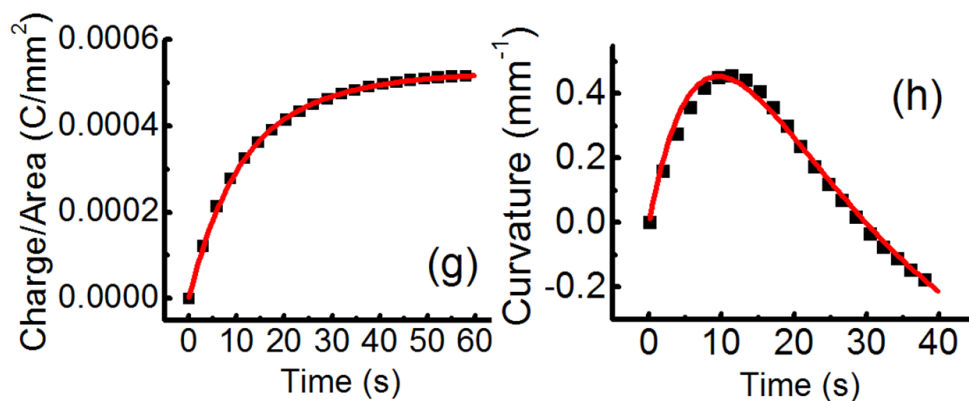


Figure 3-23 Data and fitting of charge and curvature vs. time for curvature for Nafion with 400 nm PAH/CNT LbL composite and EMI-Tf IL under 4V step voltage

The results in Figures from 3-18 to 3-23 can be understood based on a two-carrier model to account for the presence of the mobile cations and anions in the IPCNCs which have different mobilities. Using a simplified R-C equivalent circuit model for each type of ion (cations and anions) in the IPCNCs leads to Figure 3-24, where the two branches represent the ion transport of two types of ions.

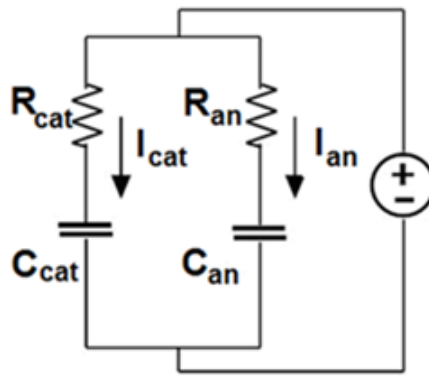


Figure 3-24 Equivalent circuit with two carrier currents

In the figure, the R-C transmission line equivalent circuits used in Section 3.3.1 in each branch are simplified into R_{cat} and C_{cat} or R_{an} and C_{an} , respectively, where the subscripts “cat” and “an” indicate cations and anions. It should be noted that, in this modeling, only the time constant of each branch is crucial to the time domain analysis, and R-C circuit in series is used here for simplicity. Hence, the charge density Q vs. time under a step voltage becomes

$$Q(t) = Q_0^{cat} (1 - e^{-t/\tau_{cat}}) + Q_0^{an} (1 - e^{-t/\tau_{an}}) \quad (3.2)$$

where the time constant τ_{cat} and τ_{an} will depend on the porous electrode morphology as well as the ion mobility ($=RC$ time constant).

The accumulation or depletion of excess ions in the composite electrodes will cause expansion and contraction in the porous electrode regions. As schematically illustrated in Figure

3-25, in contrast to the conduction current in which the oppositely charged mobile ions add together (equation (3.2)), the strains they generate will have opposite signs and hence will cancel each other. Therefore, the curvature, which is proportional to the net strain in the IPCNCs, follows

$$\kappa(t) = \kappa_0^{cat}(1 - e^{-t/\tau_{cat}}) - \kappa_0^{an}(1 - e^{-t/\tau_{an}}) \quad (3.3)$$

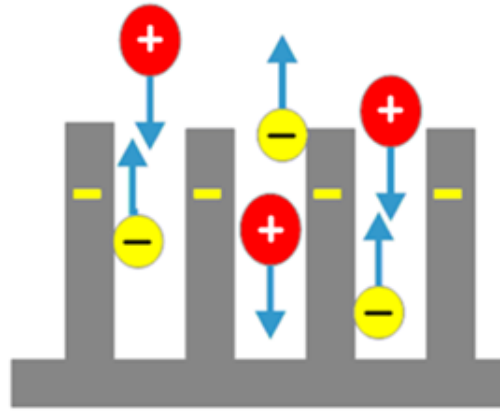


Figure 3-25 Schematic diagram of strain cancellation effect in electrodes

Equations (3.2) and (3.3) are used to fit the experimental data (solid curves in Figures from 3-20 to 3-23) and the fitting parameters are summarized in Table 3-4.

Table 3-4 Summary of fitting parameters for the IPCNCs discussed

	RuO ₂ /Nafion	RuO ₂ /Aquivion	PAH/Au LbL	PAH/CNT LbL
	EMIBF ₄	EMITf	EMITf	EMITf
τ^{cat} (s)	6	7.9	4.83	9
τ^{an} (s)	25	36.3	53	20
Q^{cat} (C/mm ²)	2.82×10^{-4}	8.46×10^{-5}	4.28×10^{-4}	3.17×10^{-4}
Q^{an} (C/mm ²)	1.57×10^{-4}	9.48×10^{-5}	2.91×10^{-4}	2.10×10^{-4}
κ^{cat} (mm ⁻¹)	1.83	1.29	0.74	2.5
κ^{an} (mm ⁻¹)	2.13	2.62	2.04	3.1

The fitting results indicate that τ_{cat} is smaller than τ_{an} . That is, the cations have fast transport speed compared with the anions, which causes the initial bending actuation from the expansion of cathode and contraction of the anode. As time progresses, the anions will generate strain in the opposite direction and eventually cause the IPCNCs to bend in the opposite direction. κ_{cat} and κ_{an} , as well as the ratio of $\kappa_{\text{an}}/\kappa_{\text{cat}}$ depend highly on the electrode morphology and the coupling between the ions and the composite electrodes. $\tau^{\text{an}}/\tau^{\text{cat}}$ for the IPCNCs with Nafion/RuO₂ (=4.16) and Aquivion/RuO₂ (=4.6) are similar. For the IPCNCs with LbL electrode layers, $\tau^{\text{an}}/\tau^{\text{cat}}$ is 10.97 for PAH/Au and 2.22 for PAH/CNT, respectively, which is caused by the difference between gold nanoparticles (Au) and carbon nanotubes (CNT).

Table 3-5 Diffusion coefficients (measured) and electrophoretic mobilities (calculated) from pulsed-gradient NMR for the ILs studied

	EMIBF4		EMITf		EMITf in Nafion ^a	
	EMI ⁺	BF ₄ ⁻	EMI ⁺	Tf ⁻	EMI ⁺	Tf ⁻
D (10 ⁻¹² m ² s ⁻¹)	43.0	33.7	44.0	29.2	3.86	2.73
μ (10 ⁻⁹ m ² V ⁻¹ s ⁻¹)	1.67	1.31	1.71	1.14	0.150	0.106

^a 32 wt% EMITf in Nafion with 2.1 wt% co-existing water. All data are taken at 25 °C.

For comparison, the diffusion coefficient from the NMR data and the mobility deduced from the Einstein relation for neat ILs and the EMI-Tf IL in Nafion are listed in Table 3-5. Notably, the cation (EMI⁺) has higher mobility than that of anions (BF₄⁻ and Tf⁻), which is consistent with the experimental results presented.

However, the ratio of $\mu_{\text{cat}}/\mu_{\text{an}}$ is 1.27 in neat EMI⁺BF₄⁻ and 1.5 in neat EMI⁺Tf⁻, which are much smaller than the ratio of $\tau_{\text{an}}/\tau_{\text{cat}}$ from the ion transport in the IPCNCs. Meanwhile, these ratios also do not match the ion size ratios that are calculated by *ab initio* or other estimations in the literature, which are shown in Table 3-6.[78] According to Stoke's law, smaller ions are expected to move faster than the large ions. These results indicate ion clustering in the ionic

liquids and the crucial role played by the CNC morphology in determining the ion transport in the porous electrodes. Moreover, the large increase of τ_{an} compared with τ_{cat} suggests a possible large effective ion size (ions plus aggregation shells) of the anions in the transport process in these composites electrodes.

Table 3-6. Ion size estimation [78]

	Molecular Dimension	Molecular volume estimated
	calculated by <i>ab initio</i> (Å)	(Å ³)
[EMI ⁺]	7.8 × 5.8 × 3.3	182
[BF ₄ ⁻]	3.1 × 3.1 × 3.1	74
[Tf ⁻]	4.4 × 4.4 × 3.3	142

Furthermore, a comparison of the ratio of $\kappa^{\text{an}}/Q^{\text{an}}$ with $\kappa^{\text{cat}}/Q^{\text{cat}}$ reveals that the anions are more effective in generating strain when they are stored in these porous electrodes. This again suggests that the anions when they are stored in the porous electrodes have much larger aggregation shells, or that they associate more strongly with the ionic electrode matrix, resulting in a larger effective ion size and higher strain generated. The results here demonstrate a simple means to compare the effective ion size of the cation and anion of an IL in electroactive devices.

Besides the above quantitative analysis of the transports of cations and anions, the electromechanical energy efficiency of the samples studied here can be calculated from their curvatures, Young's moduli, thicknesses and charge densities. The equations for these calculations were introduced in Chapter 2 Section 2.2.1.4. The Young's modulus of each layer is listed in Table 3-7. The electromechanical energy efficiency and cation energy efficiency of the four IPCNCs is presented in Figure 3-26.

Table 3-7. Young's modulus of each layer in IPCNCs [78]

	Ionomer (Nafion/Aquivion)	DAP CNC	LbL CNC	Metal (Au)
Young's Modulus (MPa)	50	300	400	20000

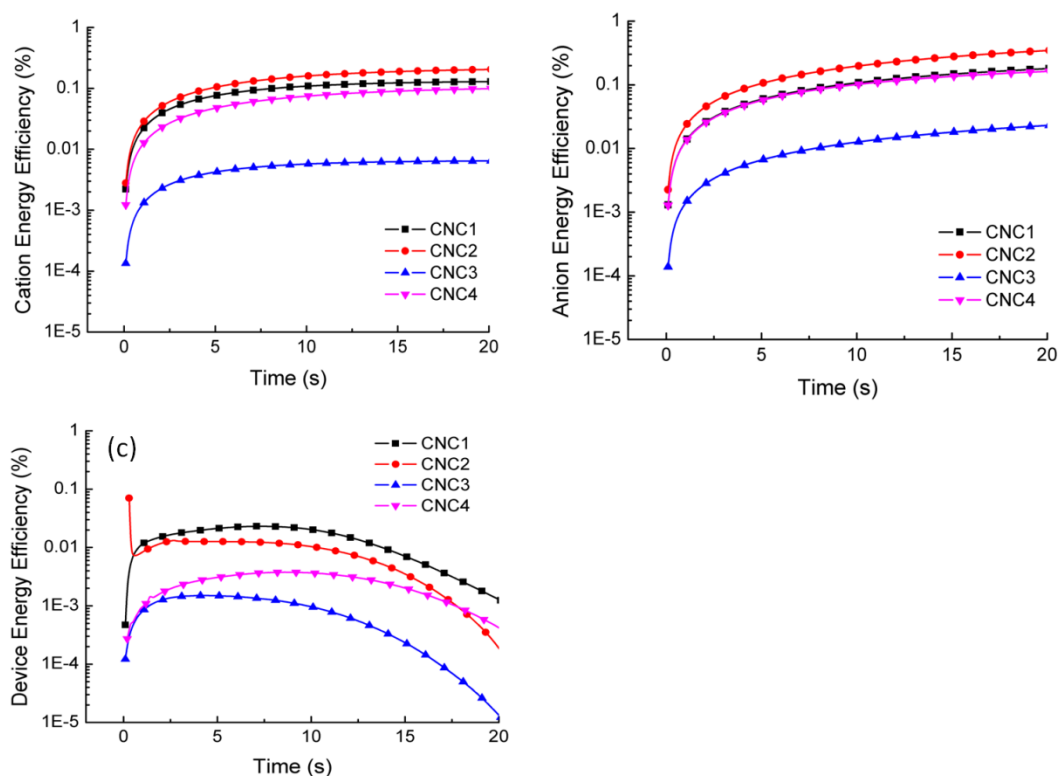


Figure 3-26 Cation, anion and device electromechanical energy efficiency of CNC1: Nafion with 3 μm thick Nafion/ RuO_2 composite electrodes at each side and EMIBF_4 IL under 3V step voltage, CNC2: Aquivion with 3 μm Aquivion/ RuO_2 composite electrodes and EMITf IL under 3V step voltage, CNC3: Nafion with 180 nm PAH/Au LbL composite electrodes and EMITf IL under 4V step voltage, and CNC4: Nafion with 400 nm PAH/CNT LbL composite and EMITf IL under 4V step voltage

As can be seen in Figure 3-26 (c), the energy efficiency of the four IPCNCs with different composition and operating conditions is as low as 0.01%, which is much lower than other types of electromechanical transduction systems, such as electronic EAPs introduced in Chapter 1.[9] One reason of this low efficiency is the cancellation of mechanical response of two

carriers discussed in this section. When the charge consumption increases over time, the opposite mechanical responses of cations and anions lead to a dramatic mechanical energy loss. By comparing the energy efficiency of the device and those of cations and anions (Figure 3-26(a) and (b)), it can be found that the strain cancellation leads to about one order of magnitude decrease in efficiency. Hence, the selection of electrolyte is crucial to the device performance that a large difference between the effective ion sizes of the two carriers is highly desirable. However, even for the single ion (i.e. anion), the energy efficiency is still very low, which may due to the capacitive nature of *i*-EAP actuators.

3.4 Conclusion

In conclusion, this chapter examined and modeled the performance of IPCNC actuators fabricated with nanoparticles by two assembly methods, LbL self-assembly method and direct assembly process. The models reflect a variety of factors which affect the performance of actuators collectively. Deeper understanding of the equation terms would guide the way to better IPCNC designs.

In the part of electrical analysis, equivalent circuits are established to model the complex frequency-dependent impedance and initial response ($t < 10$ s) of IL containing electro-active polymer membrane and IPCNC devices. It is found that the low frequency responses of Nafion membrane actuators and Nafion coated with thin layer-by-layer (LbL) PAH/Au composite actuators indicate Warburg diffusion. Therefore, Warburg impedance is utilized to model the low frequency diffusion behavior of these devices, while the electric double layer capacitance C_{dl} represents the storage of drifting ions under electric field at high frequencies. It is found that C_{dl} for Nafion with 40 wt% EMI-Tf is $7.5 \mu\text{F}/\text{cm}^2$ and increases to $11.4 \mu\text{F}/\text{cm}^2$ with increasing surface area of the LbL composite electrode, while the Warburg coefficient A_w remains nearly the

same for both devices. As a result, the actuation magnitude and speed increase with charges accumulated due to higher C_{dl} , without much increase in the contribution from the slow ion diffusion process. Nafion coated with Nafion/RuO₂ composite actuators could also be analyzed by equivalent circuits. However, due to the complex nature of the thick CNC, a simple equivalent circuit with Warburg element is no longer adequate to model the IPCNCs, therefore, de Levi transmission line is introduced to describe the CNC layer. It is found from the de Levi transmission line model that, thick CNCs lead to a large transport time constant within the CNC layer, so that the IPCNC actuators with thick CNCs are usually slower than those with thin CNCs.

In the electromechanical modeling part, the long time ($t > 10$ s) ion transport and storage of ionic liquids in IPCNC actuators are investigated. Specifically, Section 3.3.2 shows the back relaxation and low electromechanical efficiency of IPCNC actuators at long time scale ($t > 10$ s) are caused by the strain cancellation of two carriers. It is further shown that by combining the time domain electric and electromechanical responses, one can gain quantitative information on transport behavior of the two types of mobile ions in ionic liquids (i.e., cations and anions) in these electroactive devices. By employing a two-carrier model, the total excess ions stored and strains generated by the cations and anions, and their transport times in the nanocomposites can be determined, which all critically depend on the morphologies of the conductor network nanocomposites. The result reveals that anions have a larger effective ion size than cations, and thus dominate the long time response of the ionic polymer actuators. Further discussion of the ion clustering effect will be continued in Chapter 5.

Chapter 4

IPCNC Actuators with Ordered CNC Nanomorphology

4.1 Introduction

Since 1990s, carbon nanotubes (CNTs) have drawn a great attention due to their excellent electrical[79-81], thermal[82-84], and mechanical[85, 86] properties. Among various CNTs forms (e.g. fibers[87-89], yarns[90, 91] and etc.), aligned CNT forests [92-94] process a well controlled morphology that facilitates ion transport, therefore lead to high performance ionic devices, such as batteries [95, 96] and supercapacitors [97, 98]. In this chapter, aligned CNTs with large volume fraction are utilized in the fabrication of IPCNC actuators. Thus, large strain and fast actuation response is achieved.

4.1.1 Introduction to CNT

Carbon nanotubes (CNTs) were first discovered in the black soot product in a CVD process[99]. Since then, tremendous researches were conducted in nanotube synthesis, processing, and potential applications. Because CNTs have the highest tensile strength (10-150GPa) and elastic modulus (1-5 TPa) yet discovered, [85, 86] they became promising structure reinforcing materials in various applications, from everyday items like clothes and sports gear to high-tech equipments such as body armor and space elevators. CNTs also have superior electrical properties, [79-81] for example, by rolling up the graphene sheet along different direction, the electrical conductivity of a CNT can show metallic or semiconducting behavior.

CNTs with single shell are called single wall carbon nanotubes (SWNTs). A single wall carbon nanotube is technically defined as a cylinder made by rolling up sheet of graphene as drawn in Figure 4-1. The diameter of carbon nanotubes usually vary from 0.7 nm to 3 nm, depending on the direction of rolling. In Figure 4-1, the graphene sheet rolling direction is represented by a pair of indices (n, m) . The integers n and m denote the number of unit vectors along two directions in the honeycomb crystal lattice of graphene. If $m = 0$, the nanotubes are called zigzag nanotubes, and if $n = m$, the nanotubes are called armchair nanotubes. Otherwise, they are called chiral. CNTs with more than one shell are called multiwall carbon nanotubes (MWNTs).

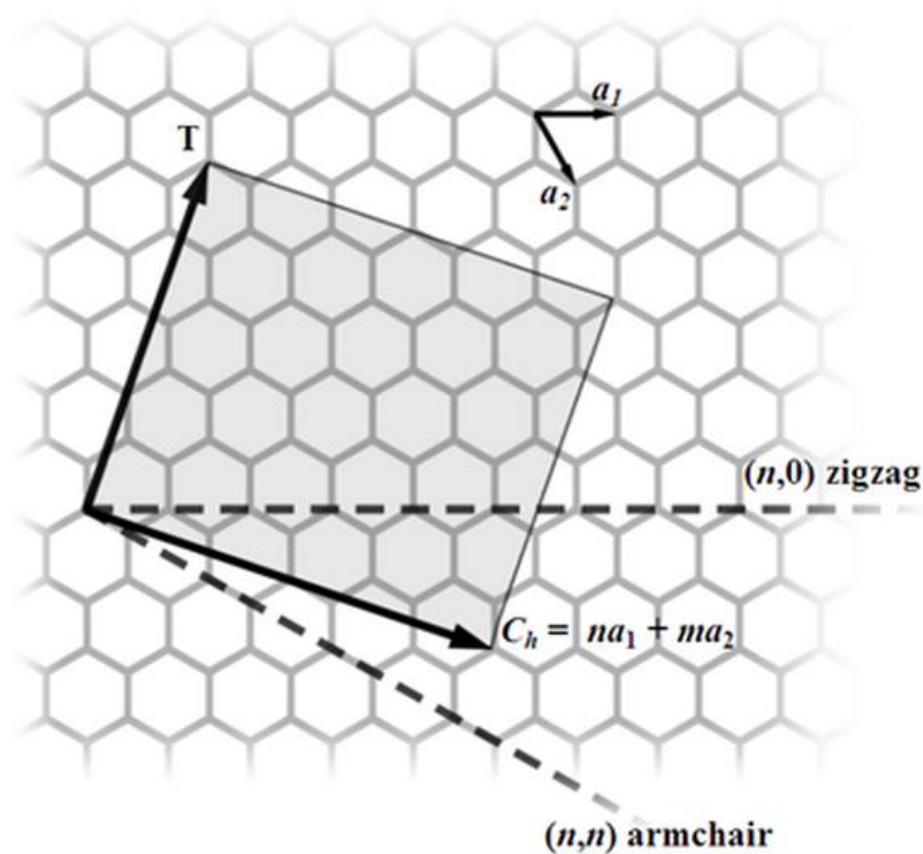


Figure 4-1 Schematic of how to "roll up" a graphene sheet to make the nanotube. T denotes the tube axis, and a_1 and a_2 are the unit vectors of graphene in real space. [100]

4.1.2 Benefits of utilizing VA-CNTs

In energy storage and conversion devices, porous materials with large surface area are of great interest. These porous materials, such as activated carbon, are usually built into disordered structures and the development of these porous materials, before the birth of CNTs and graphene, mainly focused on increasing the electrode surface area by tuning porosity. As introduced in the previous section, CNTs are cylinders of graphene sheets, therefore, they naturally possess large specific surface areas ($>2000 \text{ m}^2/\text{g}$). [101] Since 2002, CNTs started to be utilized in the supercapacitor fabrication, and it was found that the ordered structure of vertically aligned CNT (VA-CNT) forest can lead to superior device performance. [97]

The state-of-the-art SWNT-based supercapacitor is shown in Figure 4-2. Supercapacitor is also called electric double-layer capacitor (EDLC), which shares a similar 3-layer structure with the IPCNC actuator. Almost all the fundamentals of equivalent circuits introduced in Chapter 2 and 3 were initially developed by the EDLC community. On the other hand, an in-depth electrical study of the IPCNCs, which will be presented in Chapter 5, will lead to a better understanding of the EDLCs too. In Figure 4-2, activated carbon, as-grown VA-SWNT, and liquid densified VA-SWNT are fabricated into EDLCs and their performance is compared. 1M solution of Tetraethylammonium tetrafluoroborate (Et_4NBF_4)/propylene carbonate (PC) is used as the electrolyte. Because the ions in the electrolyte must diffuse through the pores within the electrode structure, as shown in Figure 4-2 (c), for activated carbon, electrodes with disordered pores possess higher ionic resistance, so that limit the power output of activated carbon electrodes. For VA-CNTs, the ion accessibility is much improved by the straight ion channels, therefore, EDLCs with VA-MWNT can be operated with a high current (high power), without much decrease in capacitance, as shown in Figure 4-2(e). Furthermore, from the comparison of as-grown and liquid densified VA-SWNT, it is found that densified VA-SWNT has much larger

volumetric capacitance, which means that densified VA-SWNT attracts more ions in unit volume. All these concepts in achieving advanced device properties can be adopted into the design and fabrication of IPCNC actuators.

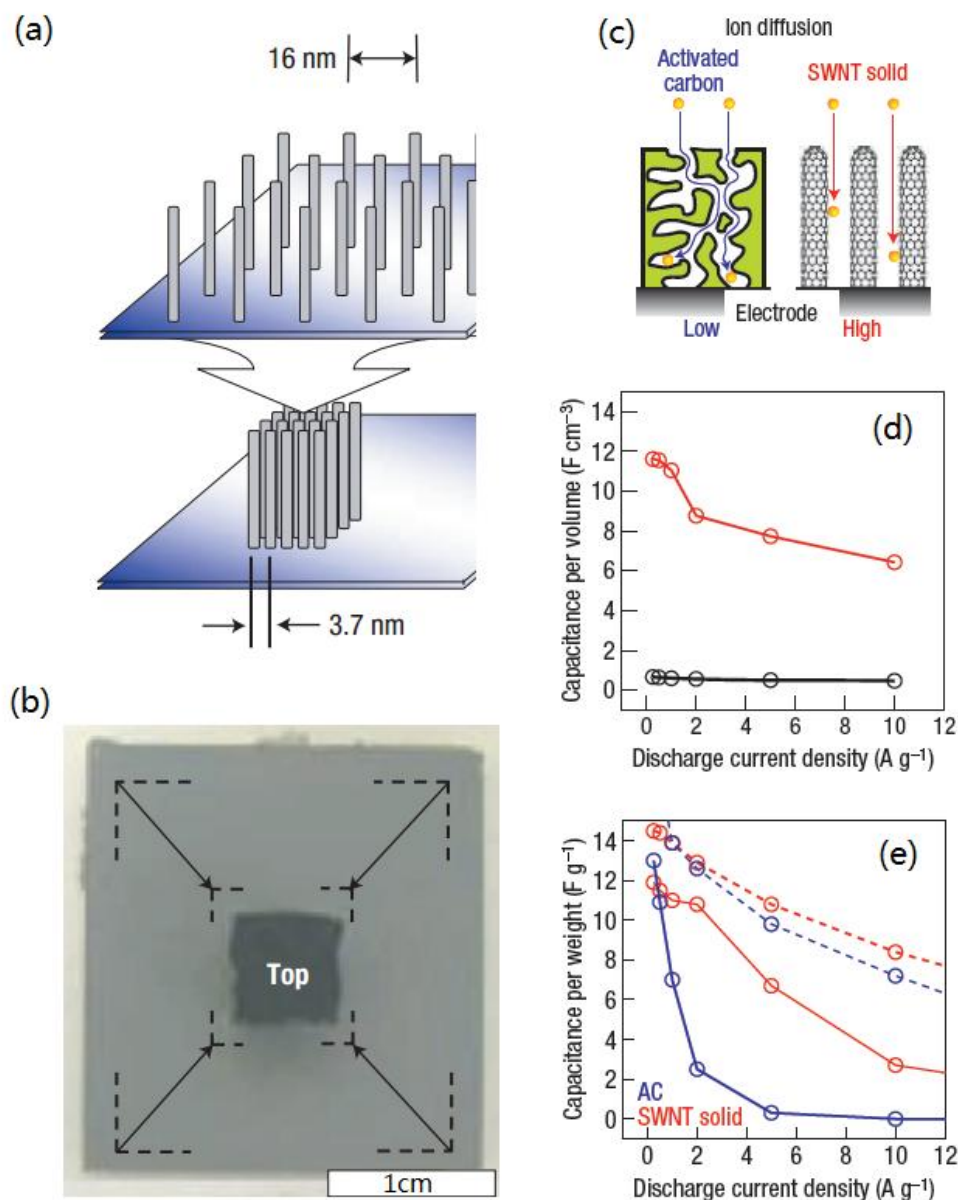


Figure 4-2 (a) Schematic diagram of the collapse of the aligned low-density as-grown forest (above) to the highly densely packed SWNT solid (below). (b) Overlaid pictures illustrating the decrease in lateral dimensions before (grey) and after (black) collapse. (c) Schematic model comparing the ion diffusion for activated carbon and the SWNT solid material. (d) Change in the

capacitance per volume using the SWNT solid sheet (red) and as-grown forest (black). (e) Capacitance versus discharge current density comparing SWNT solid (red) and activated carbon (blue) for 0.1 and 0.5mm electrode thicknesses (dashed and solid lines, respectively).[97]

In this chapter, CNC composites made with Nafion ionomer and high volume fraction VA-CNTs are studied. As can be seen in Figure 4-3, randomly distributed nanoparticles in CNCs create inaccessible areas and torturous ion transport paths, and thus reduce the ion diffusivity. An ordered structure can facilitate ion transport and hence improve the device response time or allows the fabrication of thick CNCs without much increasing the transport time. High electrical conductivity of CNTs also minimizes electrical conduction resistance of the CNCs, while the contact resistance between the conducting nanoparticles leads ineffective charge transfer processes. Moreover, large specific capacitance resulted from densified VA-CNTs are also attractive, since the IPCNC actuators operate based on the volume change due to the ion migration under electrical field.

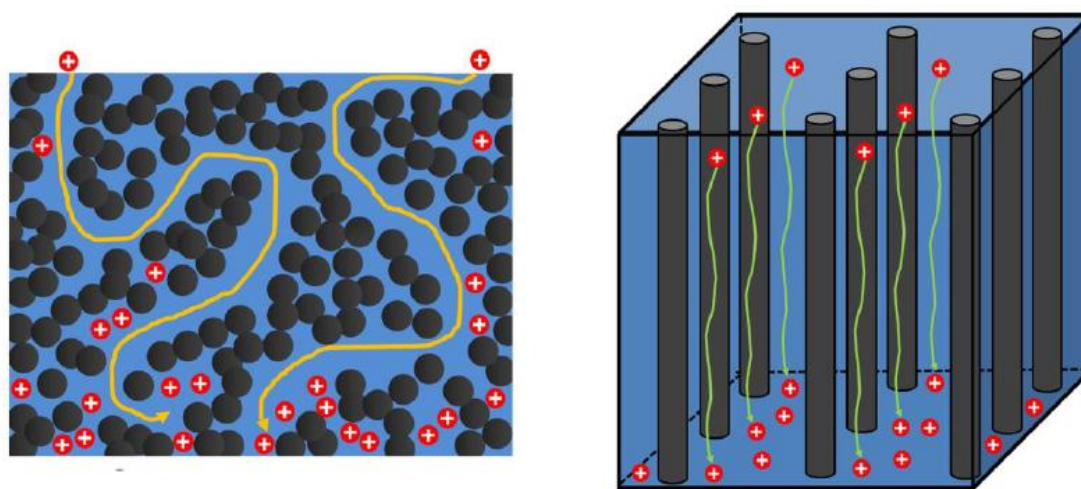


Figure 4-3 (left) Tortuous ion transport paths in nanoparticle/Nafion CNCs, where black dots are conductive nanoparticles. (right) Aligned ion transport channels in VA-CNT/Nafion CNCs.[43]

4.1.2 Anisotropic mechanical properties in VA-CNTs

Besides ionic and electrical benefits stated in the last section, VA-CNTs also lead to large elastic anisotropy in the CNCs. For IPCNC bending actuators, it is highly desirable that the strain is generated only along certain actuation direction, while the strains along all the other directions are diminished. The high elastic modulus and the high volume fraction of the VA-CNTs dramatically reinforce the CNC in the CNT alignment direction compared with that in perpendicular directions.[102, 103] As a result, the strain generated in the bending actuators due to the accumulation or depletion of the excess ions in the CNCs will be predominantly along the directions perpendicular to the CNT alignment direction.

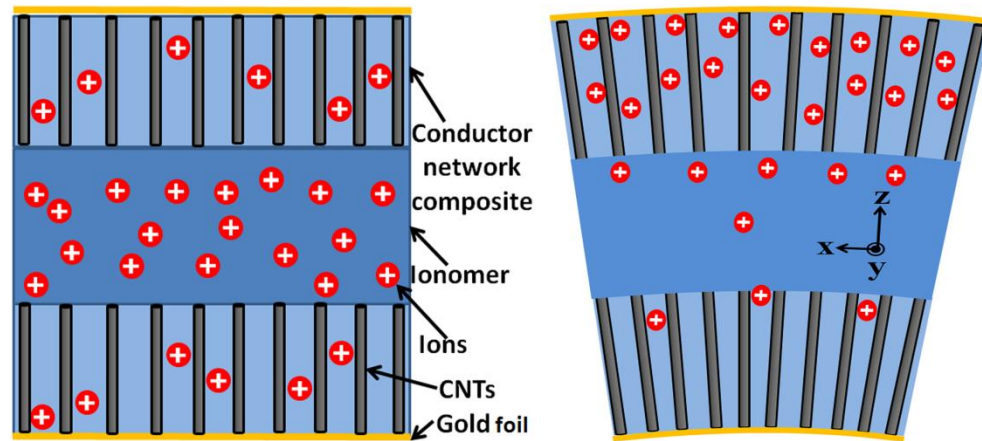


Figure 4-4 Schematic drawing of (a) a CNC/ionomer/CNC three layers bimorph actuator with VA-CNTs in the CNC layers (no voltage applied), (b) a bended actuator with excess ions on cathode side with voltage applied (z axis is in the thickness direction and x axis along length direction, i.e. actuation direction. In the actuator, the mobile ions are assumed to be cations.)[43]

As shown in Figure 4-4, under an electrical field, the volumetric expansion due to the extra ions will be suppressed in the z-direction and therefore enhanced in the desirable x and y directions. Since the volume strain generated by excess ions is $S_v = S_x + S_y + S_z$, a smaller S_z will increase the strain level S_x , and thus improve the actuation magnitude. In contrast, if the

CNCs possess isotropic elastic properties, as in ionomer/nanoparticles CNCs, the strain generated in the CNCs will also be isotropic.

4.2 Actuator Fabrication

4.2.1 CNT forest

VA-CNTs were grown using a modified chemical vapor deposition (CVD) method on silicon substrates using an Fe on alumina catalyst system, [104, 105] as illustrated in Figure 4-5. Typical growth temperature was 750°C, and the average CNT growth rate was 2 $\mu\text{m/s}$.

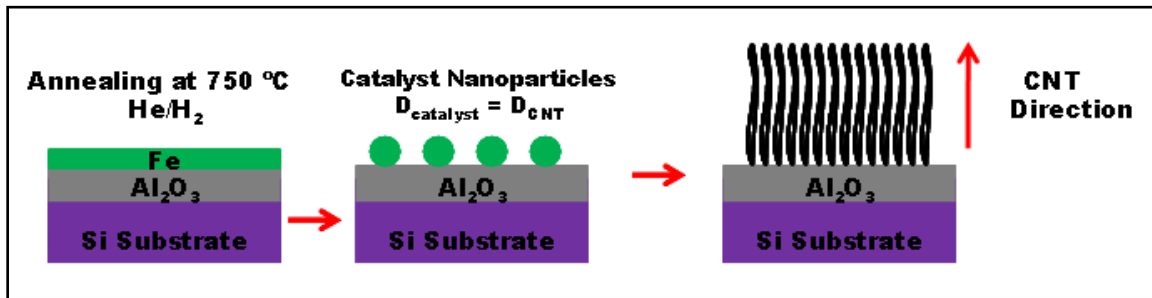


Figure 4-5 Schematic of vertically aligned CNT growth process: pretreatment of catalyst on substrate (metal film de-wetting into nanoclusters), nucleation of CNTs on the catalyst particles, and growth (Courtesy of Hulya Cebeci at MIT)

The resulting aligned CNTs have been characterized previously for alignment, CNT diameter, distribution, and spacing.[106] The as-grown CNTs (referred to as 1 % volume fraction (V_f)) have densities of 10^9 – 10^{10} CNTs/cm². The average diameter of these CNTs is 8 nm (3-5 walls) and the CNT-CNT spacing (center to center) is approximately 80 nm. For high volume fraction CNT fabrication, the CNT array was released from the silicon substrate and then subjected to a mechanical biaxial densification process in two orthogonal directions. By varying the inter-tube distance via densification, variable-density CNT arrays (10 Vf% and 20 Vf%) can

be obtained.[107] The densification process is shown in Figure 4-6, and SEMs of 1 Vf% (as-grown) and 10 Vf% are presented in Figure 4-7.

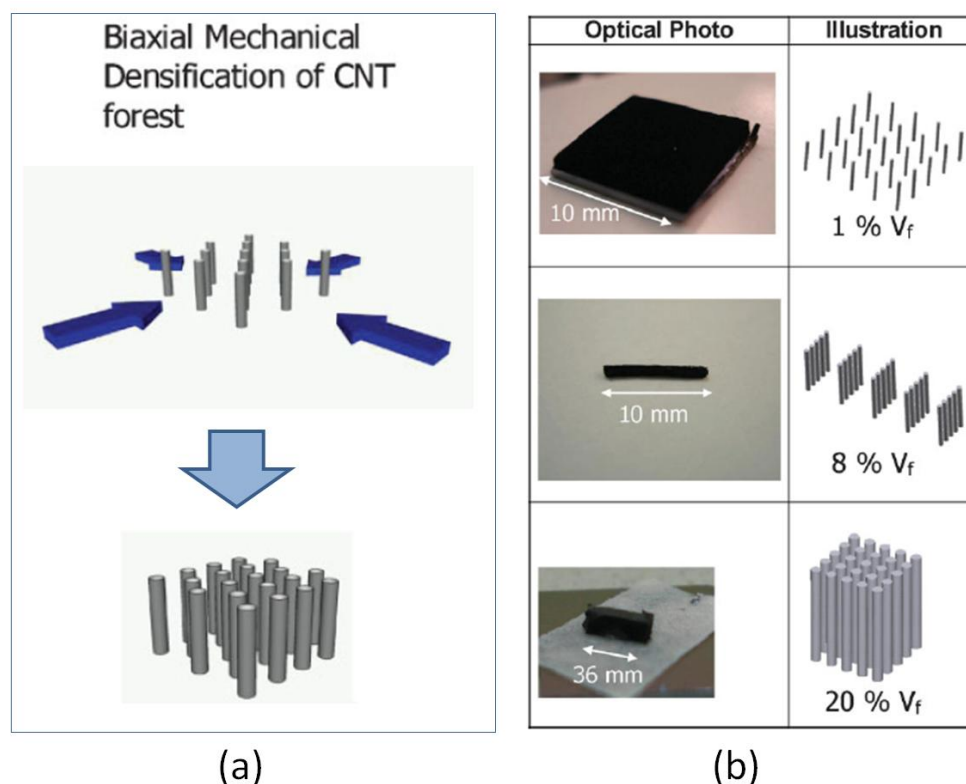


Figure 4-6 (a) schematic of densification of variable volume fraction aligned-CNTs (b) Optical image of aligned CNT volume fraction from mechanical densification of 1mm tall A-CNT forests at 1% (as-grown), 8% (uniaxially densified), and 20% (biaxially densified) volume fraction. [107]

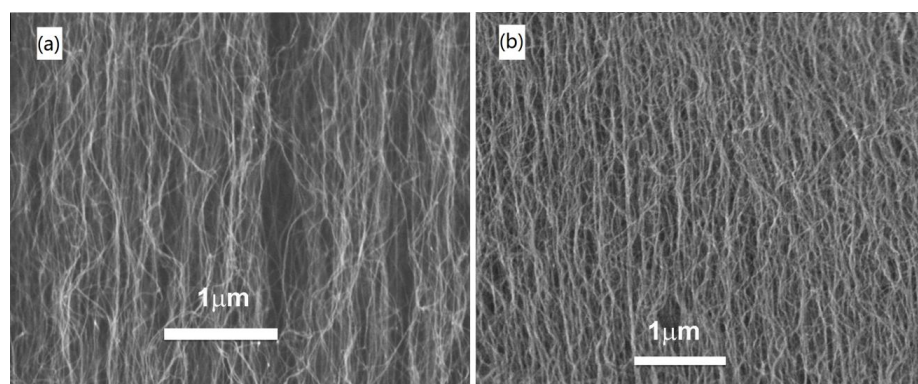


Figure 4-7 SEM images of (e) 1% Vf CNT forest as grown, and (f) 10% Vf CNT forest after densification. [107]

4.2.2 VA-CNT actuator fabrication

In the fabrication process of the VA-CNT forest/Nafion composites, the solvent in water/alcohol based commercial Nafion dispersion (Ion-Power) was first replaced by Dimethylformamide (DMF). The high boiling point (153 °C) of DMF makes it possible to slowly evaporate the solvent when processed at room temperature. A fast evaporation of the solvent will cause collapse of CNT array and/or cracks inside composite as shown in Figure 4-8 (a).

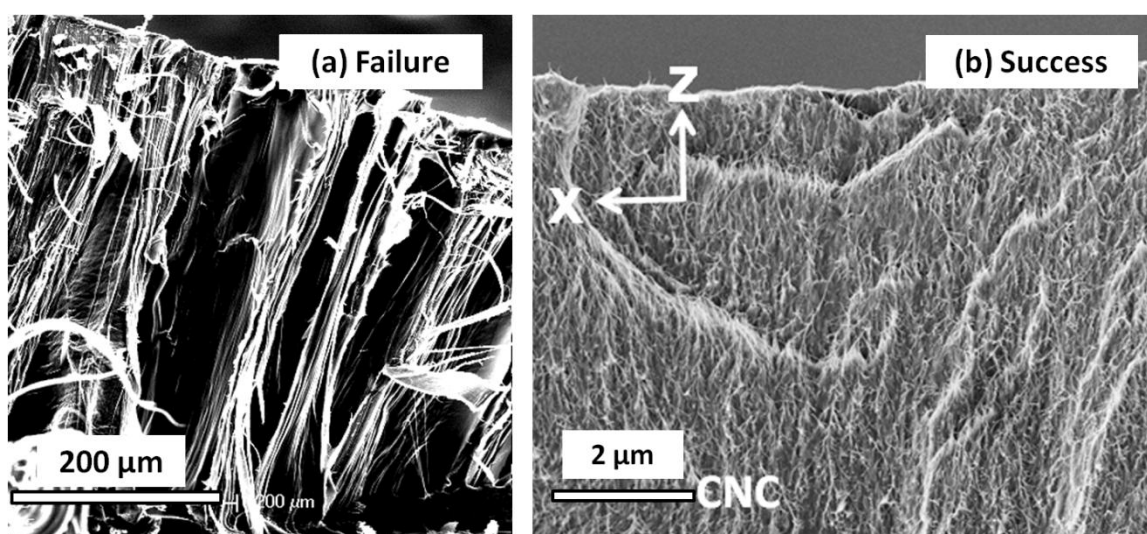


Figure 4-8 SEM images of (a) failure example due to fast solvent evaporation and (b) success example of Nafion/VA-CNT composite with CNT array in thickness (z) direction

In the fabrication of Nafion/VA-CNT composite, Nafion solution was infiltrated into CNT arrays under vacuum for several hours to remove trapped air between nanotubes, which is extremely important to prepare high quality Nafion/VA-CNT composites. After many trials, the entire evaporation process of the high quality CNC finally took about one week. After removing the solvent, the composite was annealed at 130 °C under vacuum for 1 hour to increase the crystallinity of Nafion. The SEMs of Nafion/VA-CNTs composites are displayed in Figure 4-8 (b).

In the actuator fabrication, Nafion/VA-CNT nanocomposites were first embedded in an epoxy. After epoxy cured, the samples were sectioned by a finesse microtome with VA-CNTs perpendicular to the cutting direction. Then, extra epoxy around the Nafion/VA-CNT nanocomposite thin slices was carefully removed with a razor blade. After microtome sectioning, 12 μm thin CNC layers were bonded to a piece of Nafion film by an ultra-thin layer of Nafion dispersion ($<0.1 \mu\text{m}$), which was deposited by ultrasonic spraying. The whole CNC/Nafion/CNC layers were then clamped by two pieces of Kapton films under a pressure. The stacks were dried and annealed at 130 $^{\circ}\text{C}$ to further improve the bonding by increase the crystallinity of the ultra-thin layer of Nafion binder. Ionic liquids EMI-Tf was soaked into the as-made actuator until 40wt% was achieved. Finally, 50 nm thick gold electrodes were mechanically bonded on the two surface of the actuator to increase surface conductivity.

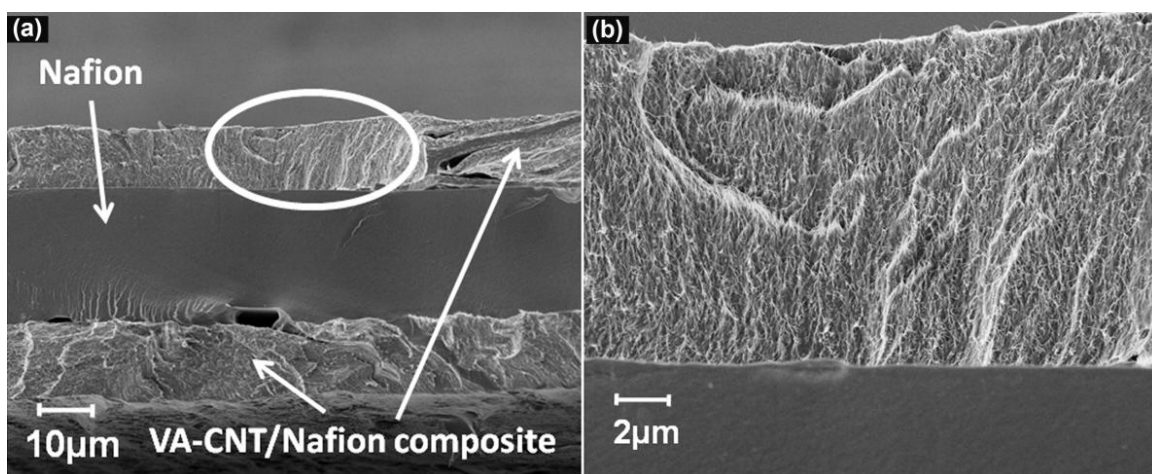


Figure 4-9. SEM images of (a) as-made Nafion/VA-CNT actuator and (b) interface region, showing aligned CNTs in CNC layer.

4.2.3 RuO₂ actuator fabrication

For the comparison purpose, 12 μm thick RuO₂ IPCNCs are fabricated with the directly assembly method. 25 μm thick commercial Nafion film NR-211 from Aldrich was used as the

spacer layer, which has been extensively discussed in Chapter 3. Nafion/RuO₂ composite was fabricated by mixing RuO₂ nanoparticles (from Alfa Aesar with 13-19 nm diameter) with 20 wt% Nafion dispersion from Ion Power. A 1% dispersion of Nafion solution with 40 vol% of RuO₂ nanoparticles (respect to Nafion) was used and the mixture was then sonicated and sprayed onto the two surfaces of Nafion film. After spraying, these films were transferred to vacuum oven to remove the solvent and annealed at 130°C for one hour. 12 μm of Nafion/RuO₂ CNCs was coated to Nafion membrane and compared to 12 μm of Nafion/VA-CNT CNCs in this chapter.

4.3 Results and Discussions

4.3.1 Electrical properties

Table 4-1 List of through plan conductivity of CNT forests, VA-CNT CNC, and RuO₂ CNC

	Through plane conductivity (S/cm)
1 vf% CNT forest	0.5
10 vf% CNT forest	3.6
20 vf% CNT forest	4.5
10 vf% CNT/Nafion composite	2.8
40 vf% RuO ₂ /Nafion composite	1.6

The electrical conductivity of the VA-CNT forest, the Nafion/VA-CNT CNC, and the Nafion/RuO₂ CNC are characterized and compared in Table 4-1. It is found that the conductivity of the VA-CNT forest almost linearly scale up with the densification. After infiltrating Nafion dispersion into the VA-CNT forest, the electrical conductivity of the CNTs maintains, which shows that the fabrication of Nafion/VA-CNTs CNC is successful. Compared to the Nafion/RuO₂

composite, which possesses 40 vol% of conductor in the CNC, Nafion/VA-CNT with only 10 vol% of conductor loading exhibits higher conductivity.

Besides good electronic performance of VA-CNT proved above, the improvement in ionic conductivity is also proved. The ionic conductivity of the CNC layer are usually reflected by the x (Z') intercept of Nyquist plot at high frequency. Nyquist plots of Nafion/VA-CNT actuator and Nafion/RuO₂ actuator with 40 wt% of EMITf uptake are displayed in Figure 4-10, which shows that Nafion/VA-CNT CNC exhibits higher ionic conductivity than that of Nafion/RuO₂ CNC. Further discussion of the impedances of Nafion/VA-CNT and Nafion/RuO₂ IPCNC actuators will be analyzed by equivalent circuit fitting in Section 4.3.4.

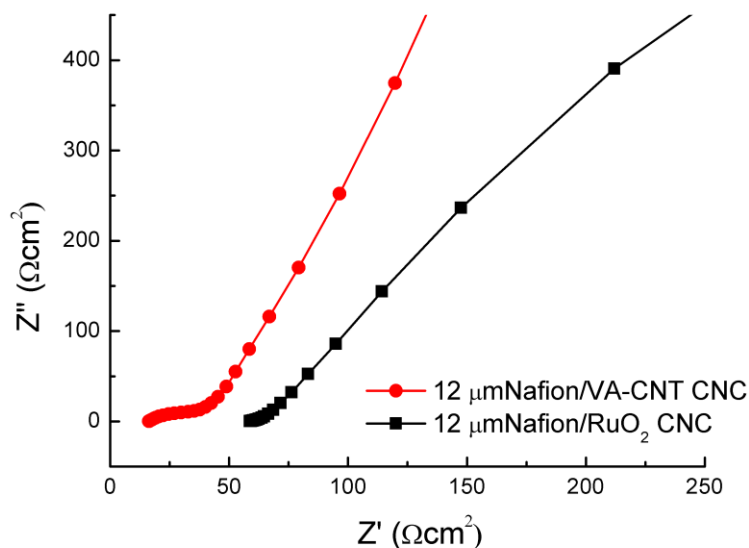


Figure 4-10 Nyquist plots of IPCNCs: Nafion with 12 μm Naifon/VA-CNT CNC and Nafion with 12 μm Naifon/RuO₂ CNC. All IPCNCs contains 40 wt% of EMI-Tf.

4.3.2 Mechanical properties

For the bending actuators investigated in this dissertation, the strains generated near the two electrodes are assumed to have the same magnitude with opposite sign, which has been

introduced in Chapter 2 Section 2.3.1.1 and 2.3.1.2. As a result, the anisotropic strain generation property of the Nafion/VA-CNT nanocomposite cannot be easily characterized. Hence, this unique property was demonstrated by directly measuring the strains generated along and perpendicular to the CNT alignment direction (i.e., the thickness direction or z-direction) of Nafion/VA-CNT composites from the absorption of ionic liquid EMI-Tf. For the comparison purpose, pure Nafion films (Dupont NR-211 and 212) were also fabricated under the same condition and their strains are tested in the same way.

After soaking IL, the CNCs made with VA-CNTs exhibit a very different anisotropic deformation from the Nafion films, as shown in Figure 4-11. The pure Nafion films, upon absorption of EMI-Tf, exhibit a large thickness strain ~22%-25% and a much smaller lateral strain ~8-12%. In contrast, the 10 vol% Nafion/VA-CNT nanocomposites exhibit much smaller thickness strain ~7%, while the lateral strain is increased to 12.1%. These results demonstrate that the high volume fraction VA-CNTs can markedly reduce the strain in the composites along its alignment direction while enhancing the strain in the perpendicular direction.

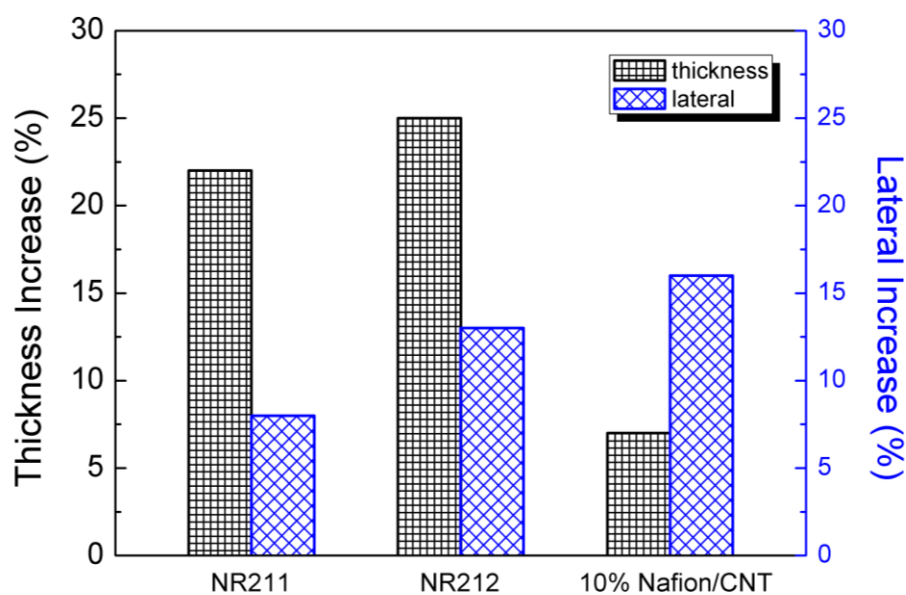


Figure 4-11 Strains generated from the absorption of ILs in the pure Nafion films and Nafion/VA-CNT composite under same conditions.

4.3.3 Bending actuation

Presented in Figure 4-12 are the initial actuation responses of Nafion/VA-CNT and Nafion/RuO₂ composite actuators under 4 volts. As introduced in Chapter 2, in IPCNC actuators, the bending actuation is primarily generated by the strains in the CNC layers. By applying the formula of the bending curvature κ ($=1/R$) and the intrinsic strain S_0 in the CNC layers, which is derived in Chapter 2 Section 2.3.1.2, S_0 can be extracted from the curvature, thickness and elastic modulus of IPCNC. Under an applied voltage of 4 volts, intrinsic strain S_0 is deduced to be 8.2%. Compared with strains generated in the IPCNC actuators with Nafion/RuO₂ nanocomposites (2.1%), the strain level of this new Nafion/VA-CNT actuator developed is much higher.

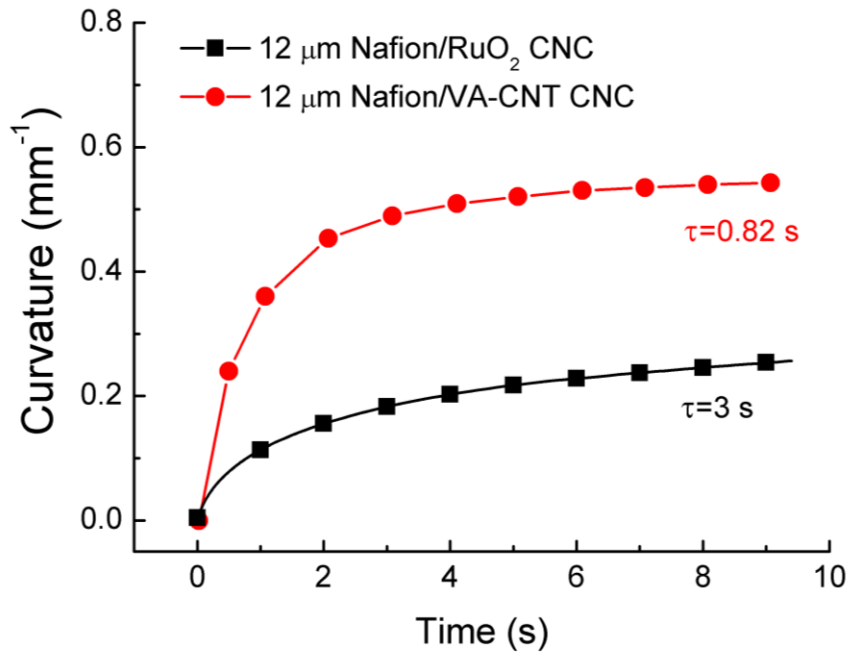


Figure 4-12 Bending curvature of Nafion/VA-CNT and Nafion/RuO₂ composite actuators under 4 volts. Time constants are obtained by fitting the curvature data with exponential functions.

Dynamic performance of this new IPCNC actuator is also assessed to determine the actuation speed by fitting the response of the actuator versus time with the exponential decay function introduced in Chapter 3 Section 3.1,

$$S_0(t) = S_{0\max} (1 - \exp(-t/\tau)) \quad (4.1)$$

The fitting results from Nafion/VA-CNTs and Nafion/RuO₂ composite actuators yield time constants $\tau = 0.82$ s and $\tau = 3.00$ s, respectively. To clearly compare performance of CNCs with different morphologies here, the strain and time constants of Nafion/VA-CNTs and Nafion/RuO₂ IPCNC actuators are displayed in Figure 4-13. It can be found that the anisotropy of the Nafion/VA-CNT composite results in larger strain, and aligned ion channels and good electronic conduction lead to smaller time constant. Further electrical analysis of the both of these actuators will be discussed in next section with equivalent circuits.

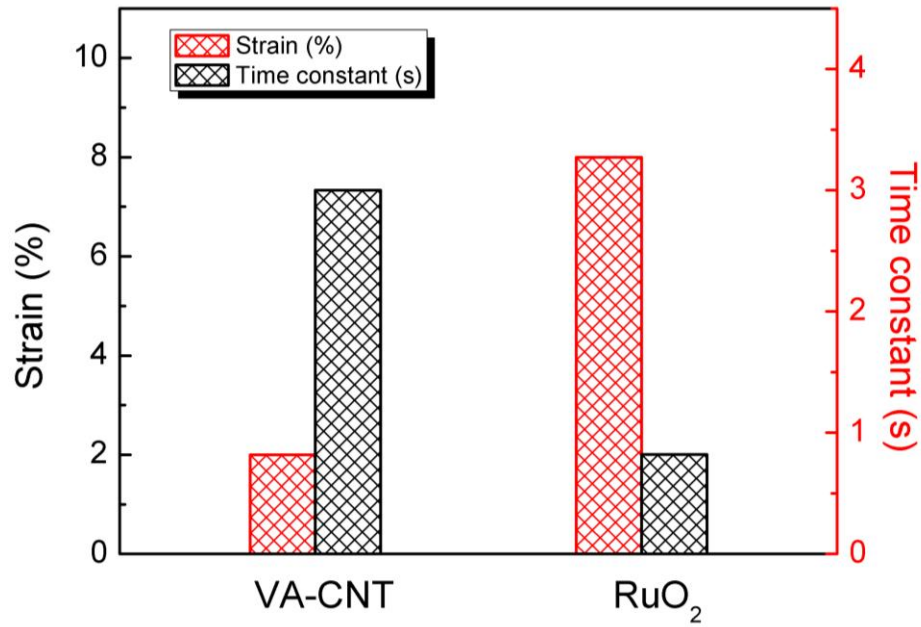


Figure 4-13 Strains and time constants of Nafion with 12 μm Nafion/VA-CNTs and Nafion with 12 μm Nafion/RuO₂ composite actuators. Both actuators have 40 wt% uptake of EMI-Tf as electrolytes.

4.3.4 Impedance modeling and analysis

As previously shown in Chapter 3 Section 3.3.1, equivalent circuits can be built to analyze the electric impedance of IPCNC actuators. Here, the De Levie transmission line model, which was used to describe the transport of ions in porous electrodes in Figure 3-17, are further simplified to model the Nafion/VA-CNT and Nafion/RuO₂ composite actuators.

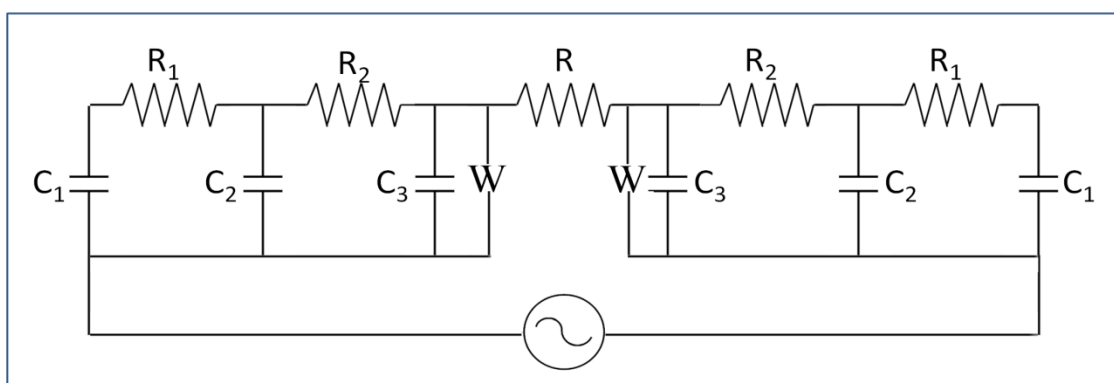


Figure 4-14 Simplified equivalent circuits for IPCNC actuators

As shown in Figure 4-14, to illustrate the physical meaning of circuit components and also to minimize the fitting parameters, the complicated de Levie transmission line model are simplified into a network, which consists of capacitors, resistors, and Warburg elements. This network includes two phases, i.e. the electrical conductor phase and the ionic conductor phase, with resistance within each phase and capacitances between the two phases. C_1 is the interface capacitance between the ionic liquids in the CNC layer and the gold external electrodes; C_2 represents the capacitance between the ionic liquids in the CNC layer and the electrical conductor in the CNC layer; and C_3 is the interface capacitance between the electrical conductor and the ionic liquids in the ionomer layer (Nafion). For the conduction of ionic liquids, three resistances show the ionic resistance; one in the composite layer (R_I), another one on the interface (R_2) and one in the bulk Nafion membrane layer (R). The electronic resistance within the CNCs is

neglected since it is much smaller than ionic resistances. Warburg elements are included to represent the diffusion portion of the electrolyte on the CNC/Nafion interface.

The data and fitting of Nafion/VA-CNT actuator and Nafion RuO₂ actuator are shown in Figure 4-15 and Figure 4-16. Their fitting parameters are listed in Table 4-2 for comparison.

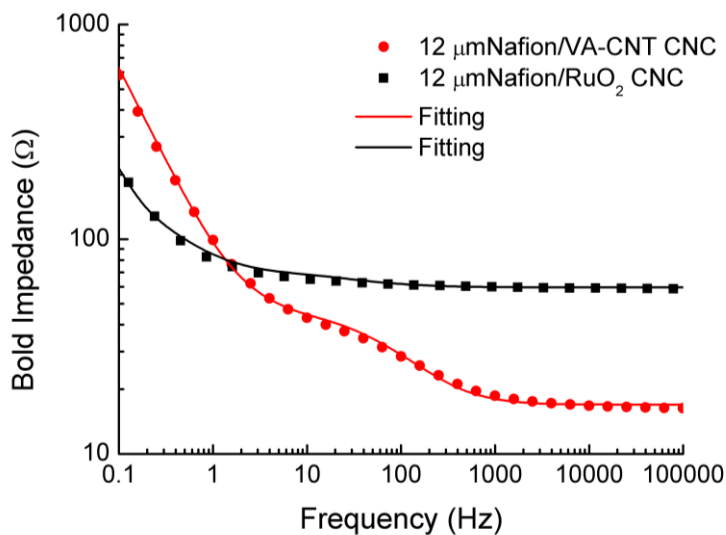


Figure 4-15 Data and fitting of bold impedance

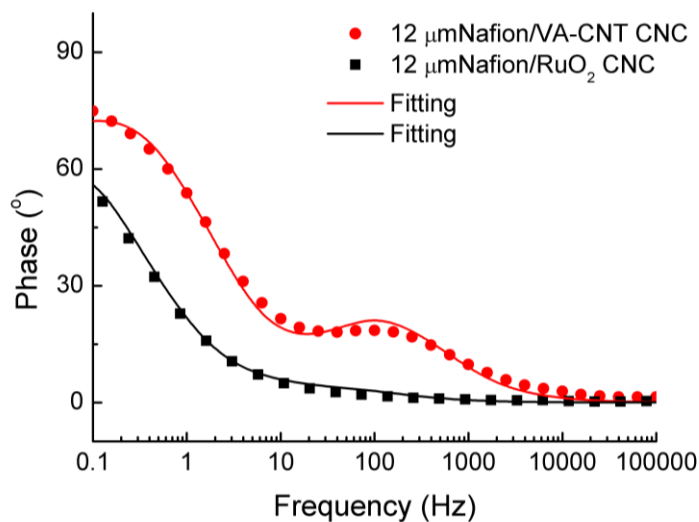


Figure 4-16 Data and fittings of phase

Table 4-2 Fitting parameters for Nafion membrane (from Chapter 3) and IPCNC actuators

Nafion	$C(\mu\text{Fcm}^{-2})$	$R(\Omega\text{cm}^2)$	$A_w(\Omega\text{cm}^2\text{s}^{-1/2})$
	7.5	9.7	10^5
VA-CNT	$C_1(\mu\text{Fcm}^{-2})$	$R_1(\Omega\text{cm}^2)$	
	7.5	13.4	
	$C_2(\mu\text{Fcm}^{-2})$	$R_2(\Omega\text{cm}^2)$	$A_w(\Omega\text{cm}^2\text{s}^{-1/2})$
	3604	12.5	817
RuO ₂	$C_3(\mu\text{Fcm}^{-2})$	$R(\Omega\text{cm}^2)$	
	155	9.5	
	$C_1(\mu\text{Fcm}^{-2})$	$R_1(\Omega\text{cm}^2)$	
	7.5	119.8	
	$C_2(\mu\text{Fcm}^{-2})$	$R_2(\Omega\text{cm}^2)$	$A_w(\Omega\text{cm}^2\text{s}^{-1/2})$
	10889	19.5	196.8
	$C_3(\mu\text{Fcm}^{-2})$	$R(\Omega\text{cm}^2)$	
	723	25.5	

From a direct comparison of the impedance data, it can be seen that RuO₂ CNC possesses a larger capacitance, since the low frequency impedance is dominated by the reciprocal of CNC capacitance. This higher capacitance is caused by larger loading of conductor in the composite, where RuO₂ occupies 40 vol% of the CNC and VA-CNT only occupies 10 vol%. This result is also reflected from the fitting parameters. As displayed in Table 4-2, total capacitance of Nafion/RuO₂ CNC is higher than that of Nafion/VA-CNT CNC. In the meantime, Warburg impedance, which reflects the diffuse ion storage at low frequency, also shows the difference in the conductor loading. When the applied voltage is small ($\sim k_B T/e$), the Warburg coefficient is inversely proportional to the electrode area (Appendix C), [59]

$$A_w = \frac{\alpha}{neA\sqrt{D}} \quad (4.2)$$

where n is the valence, A is the electrode area, α is the coefficient, and D is the diffusion coefficient. Although diffuse charge cannot access all the surface area of the CNC, increased

conductor surface area on the Nafion/CNC interface A still leads to diminished A_w values, where $A_w(\text{RuO}_2) < A_w(\text{VA-CNT}) < A_w(\text{Nafion})$. However, the better charge storage capability does not bring RuO_2 IPCNC actuator a larger bending magnitude than VA-CNT IPCNC actuator. The anisotropic property of VA-CNT CNC, which has been discussed in Section 4.3.2, allows the structure to generate strain in preferred direction, and thus lead to a higher bending magnitude, as shown in Section 4.3.3.

Besides the comparison of charge storage, the impedance data also indicates the response speed of the VA-CNT and RuO_2 CNCs. In Figure 4-15, VA-CNT IPCNC reaches the same phase value (e.g. 45°) at higher frequencies than RuO_2 IPCNC that implies a smaller time constant for VA-CNT CNC. From the fitting parameters, the time constants R_1C_1 and R_2C_2 for RuO_2 CNC are both larger than those of VA-CNT CNC, which implies the ion transport is slower within RuO_2 CNC.

Finally, it is worth to point out that Table 4-2 presents how CNCs affect the IPCNC response by comparing the IPCNC actuators to Nafion membrane actuator. When the large electrode area in the CNC provides 10^2 - 10^4 higher electric double layer capacitance values than the planar Nafion membrane actuator, the Warburg impedance element A_w of the CNC is only about 10-20 times smaller than that of the diffuse charge on planar Nafion/Au interface, suggesting a diminishing contribution of the diffusion process to the charge transport. When the ionic resistance is not too large (i.e. in VA-CNT CNC), the increase in the electric double layer capacitance of the CNC compared with the relatively minor contribution from the slow diffusion process indicates a significantly increased actuation level with relatively fast speed, which have been shown in the previous section.

4.4 Conclusion

In conclusion, aligned carbon nanotubes (VA-CNTs) with ultrahigh volume fraction markedly improve the electromechanical performance of IPCNC actuators. High elastic modulus of the VA-CNTs creates an anisotropic elastic response in the composite electrodes, which suppresses the unwanted strain and markedly enhances the actuation strain ($> 8\%$ strain under 4 V). In the meantime, continuous ion channels and high electrical conduction of the aligned CNTs in the composite electrodes allow fast ion transport, high ionic conductivity, and thus lead to fast device actuation speed ($\tau_0 = 0.82$ s).

To further understand the relation between the ion transport and the actuator performance, equivalent circuits are built to model the electric impedance of the VA-CNT actuators. The fitting results show that in the VA-CNT actuators, the charge diffusion process (slow process) is comparably less significant than the electric double layer formation (fast process). Hence, IPCNC actuator with large strain and fast response has been achieved by properly controlling the nano-morphology of the CNCs to enhance the compact layer formation and suppress the diffuse layer formation.

Chapter 5

Ion Distribution in Ionic Polymer Membrane Actuators

5.1 Introduction

As introduced in Chapter 1, qualitatively, the bending actuation of a typical ionic polymer membrane actuator (shown in Figure 5-1(a)) results from the redistribution of ions with different sizes near the electrodes, as illustrated in Figure 5-1(b). In general, this redistribution process is a result of ion drift and diffusion that have been intensively discussed in Chapter 3. Upon the application of a voltage, the drift current causes a fast increase in charge within short time ($t < \text{ms}$) that builds up an electric double layer; however, when compared to the diffuse layer charge at later time ($t \sim 1\text{-}10\text{s}$), which is closely related to the time domain when actuation occurs, it is not substantial.[58, 108]. Diffuse layer ions in different sizes swell the electrode regions and cause imbalanced expansion and contraction of the regions that leads to the bending of the actuator.

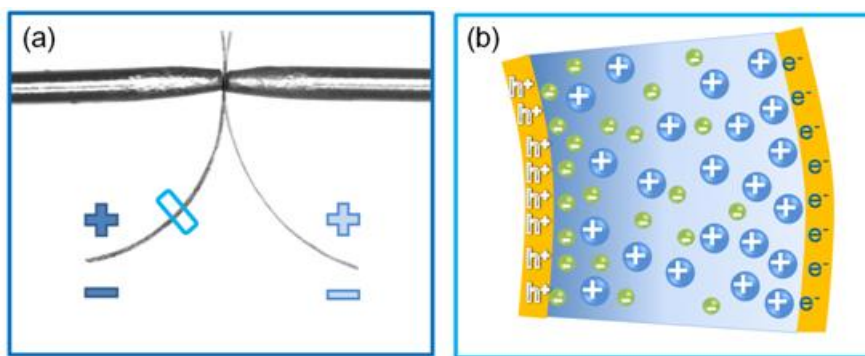


Figure 5-1 (a) An ionic polymer bending actuator under electric signal and (b) schematic of actuation mechanism.

Practically, in Chapter 3, diffuse layer charge dynamics were probed by Electrochemical Impedance Spectroscopy (EIS) and modeled as a Constant Phase Element (CPE), such as Warburg impedance. [73-75] But due to the un-defined nature of the capacitance measured at a single frequency from EIS, it is hard to obtain explicit information of the diffuse layer formation from CPE. Hence, to further explore the physical nature of the actuation mechanism, the attention is drawn to current models and theories of ionic liquids under electric field, which intrinsically can be modeled the same as electric double layer capacitors (EDLCs).

Poisson-Nernst-Planck (PNP) equations, as shown in Chapter 2 Section 2.3.2.4, are the governing equations for the charge dynamics of ionic systems in a simple configuration that electrolytes are placed in between two parallel planar electrodes. Its stationary solution gives Poisson-Boltzmann (PB) equation, which is the mathematical base for the classic Gouy–Chapman-Stern (GCS) double layer theory, which has been introduced in Chapter 2 Section 2.3.2.4.[57] PNP and PB equations are widely used by the EDLC community to describe the electric double layer and diffuse layer of various types of electrolytes, including ionic liquids. For example, recent theories (by Bazant et al.) modified PNP equations and successfully explained the electric double layer behavior of ionic liquids on a slightly charged surface.[109, 110]

However, different from dilute solutions, ionic liquids possess ultrahigh ion concentration ($\sim 3\text{-}7\text{M}$), which could not be fully described by PNP equations and PNP deduced EDLC models. Under small external field, ionic liquids fall into their linear response regime, therefore, adoption of PNP equations is reasonable.[109, 111] But for ionic liquids under high field (e.g. $100k_B T/e$), which is the voltage most EDLCs and *i*-EAP actuators operate, the validity of PNP based theories is questionable. [112] To explore the actuation mechanism and to assist the development of a physical model for the charge transport of ionic liquids under high field, it is crucial to have direct experimental information on the diffuse layer characterization of ionic liquids.

In this chapter, the mysterious diffuse ion storage mechanism of ionic liquids in ionic polymer actuators is investigated by performing a direct measurement of the ion distribution. As introduced in Chapter 2 Section 2.2.4, ToF-SIMS, which recently became a powerful tool in imaging of biomaterials, particularly tissue samples [45, 46] and single biological cells [47-49], was utilized in energy storage/conversion device characterization for the first time. Since ToF-SIMS with cluster ion beam allows etching the organic materials without damage their chemical integrity, the depth profile of the ion concentration along the film thickness direction can be probed directly, [49, 50] which makes it possible to study the electrode-electrolyte interaction in ionic polymer actuators. In this Chapter, we bombard ionic polymer actuators, of which ions are frozen at liquid nitrogen temperature, with C_{60}^+ cluster ions to extract the ion concentration information. The operation mechanism of ToF-SIMS in this process is illustrated schematically in Figure 5-2. An ionic liquid electrolyte 1-butyl-2,3-dimethylimidazolium chloride (BMMI-Cl) is used in this chapter.

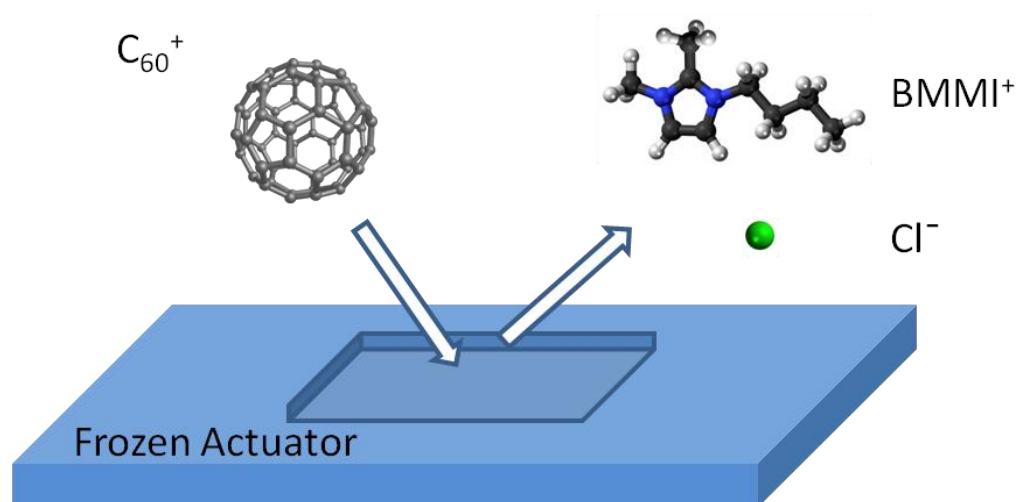


Figure 5-2 Operation mechanism of ToF-SIMS in this dissertation

5.2 Characterization of *i*-EAP Membrane Actuators

5.2.1 Sample preparation and characterization methods

Aquivion membrane with 45wt% uptake of high temperature ionic liquid BMMI-Cl with melting point 99 °C served in the dissertation and is compared that with 45 wt% uptake of EMI-Tf in the next section. High melting point of BMMI-Cl allows large temperature difference between actuator operation temperature (105 °C) and the sample frozen and handling temperature, which is -78.5 °C that cooled with dry ice. Meanwhile, it also ensures the vapor pressure of the solid state sample in ultra-high vacuum chamber is negligible, where high vacuum level is required for ToF-SIMS operation.

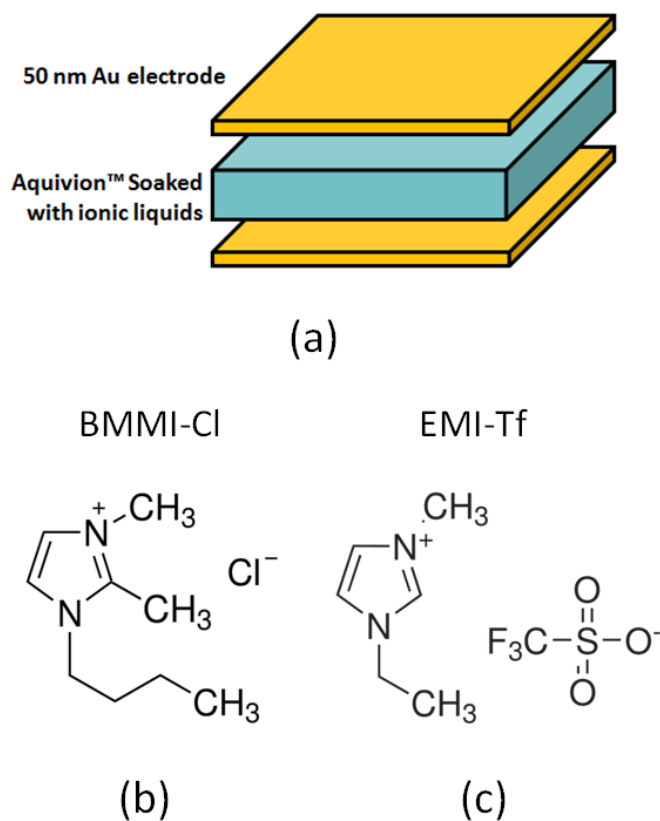


Figure 5-3 (a) Schematic of device configuration and (b) molecular structure of BMMI-Cl and (c) EMI-Tf studied.

Figure 5-3 shows the schematic of an ionic polymer membrane actuator and the chemical formula of the ionic liquids served in this study. Aquivion ionomer membrane (EW790, Solvay Solexis), BMMI-Cl (Aldrich) and EMI-Tf (Aldrich) were dried in vacuum at 80 °C to remove moisture before processing. Aquivion membranes swollen with 45wt% EMI-Tf were prepared by soaking the Aquivion membranes in EMI-Tf at 60 °C. Aquivion membranes swollen with 45wt% BMMI-Cl were prepared by soaking the Aquivion membranes in BMMI-Cl : Ethanol 1:1 solution at 60 °C. The films are then dried again in vacuum oven at 60 °C to remove ethanol. 50nm thick of gold foils (L.A. Gold Leaf) were hot-pressed on both sides of the membranes as electrodes. The uptake of ionic liquids within Aquivion membrane was calculated by measuring the weight gain after swelling. Density of the ionic liquid is calculated by weighing the ionic liquids and measuring the volume with a graduated cylinder. Roughness of the sample surface is measured by Zygo NewView™ 7300 on an area of 140 μm \times 110 μm .

The electrical measurement was carried out in a sealed box with desiccant inside to prevent the absorption of moisture. The box was then placed in an environmental chamber (Tenney Versa Tenn III) for temperature control, and the electrical characteristics were measured by a potentiostat (Princeton Applied Research 2273). The electromechanical response was recorded by using a probe station (Cascade Microtech M150) equipped with a Leica microscope and a CCD camera (Pulnix 6740CL). High temperature actuation was tested by placing sample and sample holder in a heat block (VWR) underneath the Leica microscope and the CCD camera.

5.2.2 ToF-SIMS

To collect the ion concentration data by ToF-SIMS, the actuator was firstly operated under 2.5V bias at 105 \pm 5 °C for 5 minutes, till the actuation reaches steady state. Then the sample box and actuator were transferred into an isothermal bag and fast frozen with dry ice. The

temperature was measured with an infrared thermal meter and stabilized at -40°C in 20~30 minutes. Then the actuator $2\text{mm}\times 8\text{mm}$ was taken out of the sample box with a plastic tweezers and placed on dry ice to section into two $2\text{ mm} \times 2\text{ mm}$ pieces. Gold external electrodes were then carefully peeled off with Scotch tape from sample surfaces and the samples are mounted onto the sample holder for ToF-SIMS.

The depth profile experiments were performed in a ToF-SIMS instrument, which has been described in Chapter 2 Section 2.2.4. [31] The sample stage of ToF-SIMS can be cooled to 100 K. After the actuator sample was loaded into the vacuum chamber of SIMS, it was cooled by liquid nitrogen and all depth profile experiments were run at liquid nitrogen temperature. A 40-keV C_{60}^{+} source (IOG 40-60, Ionoptika; Southampton, U.K.) is mounted to the instrument at an angle of 40° with respect to the surface normal. Under typical conditions, The kinetic energy of the singly charged C_{60}^{+} primary ion beam is 40 keV and the beam current is 200~300 pA with a beam size of $\sim 10\text{ }\mu\text{m}$. The mass spectrometer was operated in a delayed extraction mode with 50 ns delay time between the primary ion pulse and the secondary ion extraction pulse. Charge compensation was found to be unnecessary due to a charge balance between primary and secondary ion currents. For depth profiling, the C_{60}^{+} ion beam was operated in DC mode to erode through the film at an area of $340\text{ }\mu\text{m} \times 440\text{ }\mu\text{m}$. Between erosion cycles, SIMS images were acquired from the same area using the pulsed C_{60}^{+} projectile beam with a total ion fluence below 10^{11} cm^{-2} . A digital raster scheme with 256×256 pixels was employed during both the erosion and data acquisition cycles, which corresponds to a pixel step size (1-2 μm) well below the beam width. The ToF mass spectra were retrospectively extracted from various pixel areas of the image data in order to investigate crater edge effects and determine the optimum gating area as described elsewhere. [113] No edge effects were observed at the central area of 192×192 pixels inside the sputtered region, therefore mass spectra from these areas were used for depth profile analysis. Typical schematic of a ToF-SIMS instrument was provided in Chapter 2 Section 2.2.4.

Eroded crater depths were characterized by KLA Tencor 16+ profilometer. The etching rate in this chapter was calculated from the etching depths and etching times.

5.3 Results and Discussions

5.3.1 Electrical and electromechanical characterizations

Shown in Figure 5-4 (a) is the normalized Nyquist plot of two ionic polymer membrane actuators, Aquivion with BMMI-Cl and Aquivion with EMI-Tf. $Z'(\Omega)$ and $Z''(\Omega)$ have been normalized by sample size for comparison purpose. The thicknesses of both samples are $\sim 27 \pm 2 \mu\text{m}$. At 25 °C, Aquivion with BMMI-Cl, which is a foggy film from the crystallization of BMMI-Cl, stretches to right up corner of the Nyquist plot, due to its ~ 2 orders of magnitude lower conductivity than that of the membrane with EMI-Tf. It indicates that at room temperature, which is far below the melting point of BMMI-Cl, the motion of BMMI^+ and Cl^- ions is restricted. After heating to 105 °C to melt the electrolyte, the electrical performance of BMMI-Cl becomes comparable to EMI-Tf, due to the activation of mobile ions.

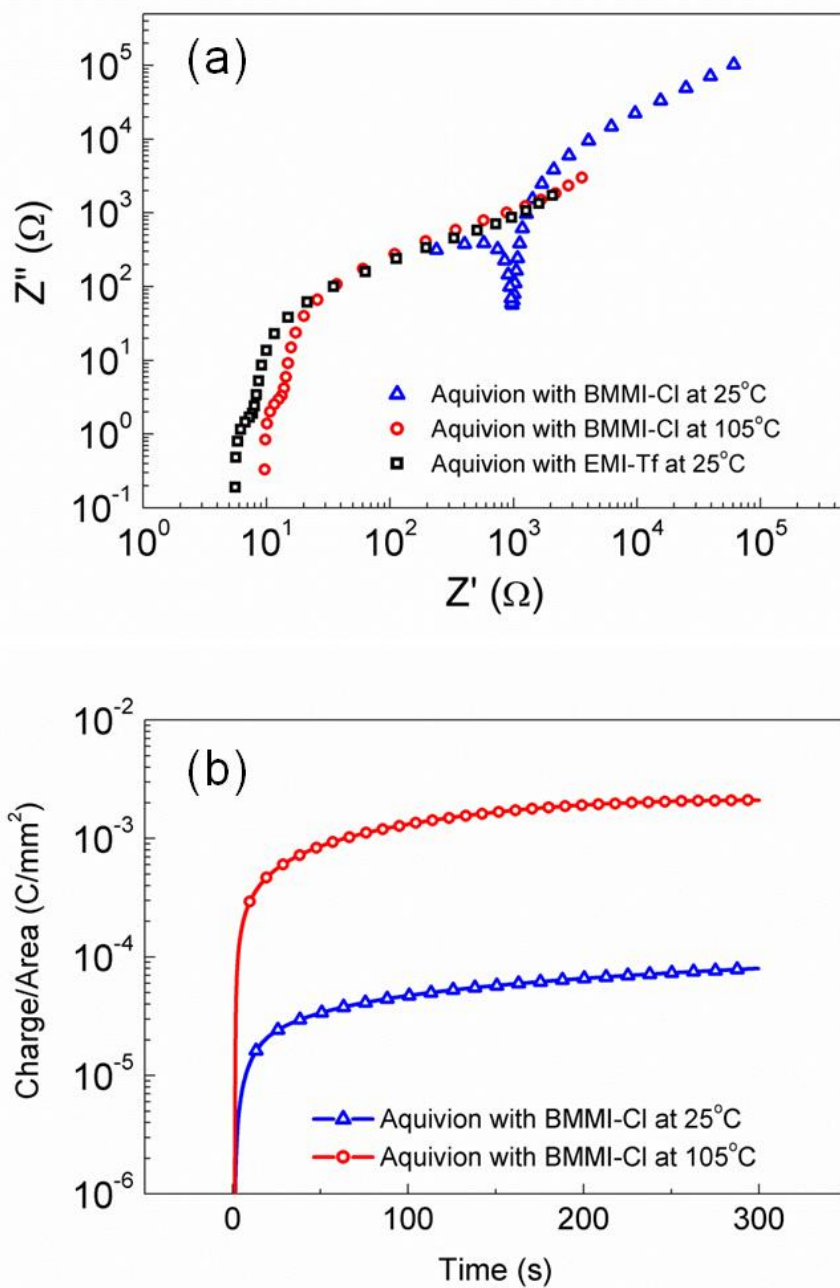


Figure 5-4 (a) Nyquist Plot of Aquivion with BMMI-Cl at 25 °C and 105 °C, compared to Aquivion with EMI-Tf at 25 °C. (b) Charge versus time of Aquivion with BMMI-Cl at 25 °C and 105 °C under 2.5V

Figure 5-4 (b) displays the charges under a higher voltage 2.5 V (Compare to the Nyquist plot that is obtained from impedance spectra @ 25mV) at 25 °C and at 105 °C. It indicates that by freezing the samples at low temperature after applying high electrical field, ions cannot rapidly move back to neutral state. The electrical testing and operation voltage (2.5V) of the actuator was determined by linear sweep voltammetry, as displayed in Figure 5-5, which shows the onset of the red-ox reaction of the electrolytes is about 3V. Usually, for an applied voltage equal or slightly larger than the electrochemical window, one could not observe significant change in the actuation and the reaction slowly affects the bending magnitude over thousands of cycles. However, the reduction in actuator lifetime becomes notable that the actuator dies within a few minutes, when the voltage is with a couple of volts higher (such as 4V) than the electrochemical window.

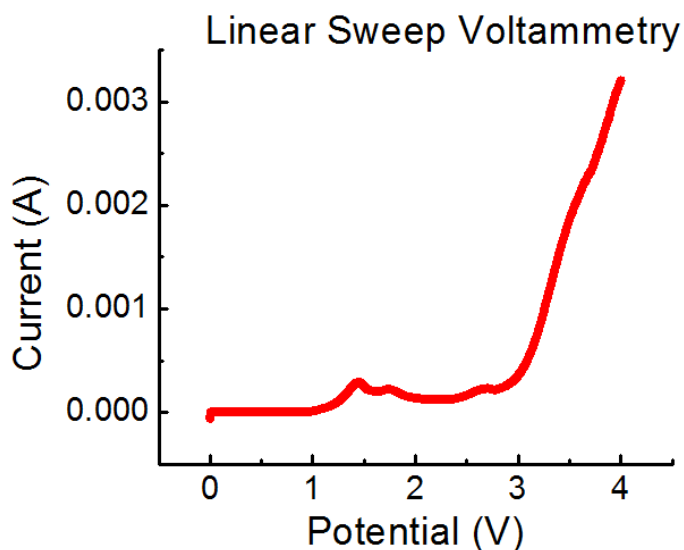


Figure 5-5 Linear Sweep Voltammetry of Aquivion with BMMI-Cl at 105 °C under AC stimulus

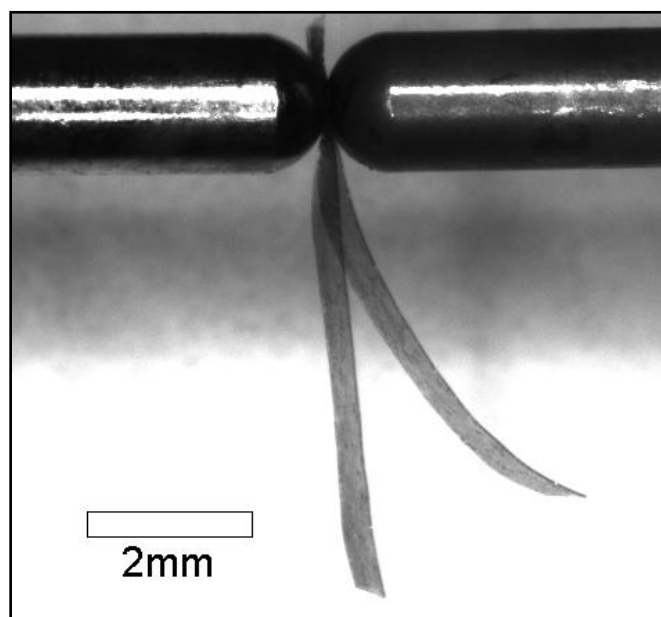


Figure 5-6 Image of bending magnitude of Aquivion with BMMI-Cl at 105 °C under AC stimulus

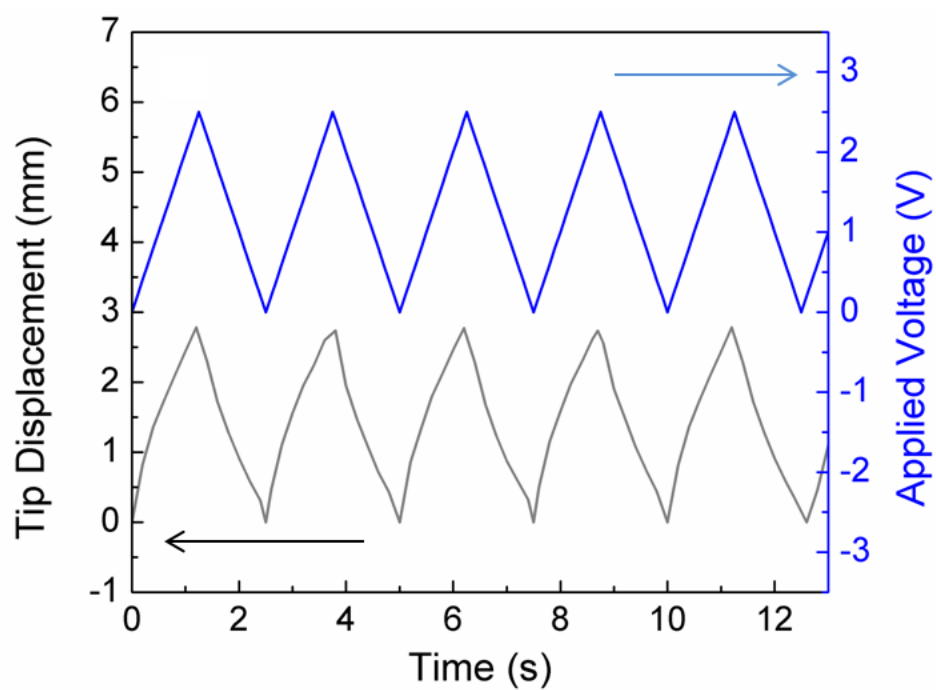


Figure 5-7 Time-resolved actuation of Aquivion with BMMI-Cl at 105 °C under AC stimulus

Figure 5-6 and 5-7 show the tip displacement of a 1 mm wide 6 mm long actuator under 2.5V 0.2Hz at 105 °C. It has a corresponding bending curvature of 0.4 mm^{-1} , that is comparable to the maximum bending magnitude of the room temperature actuators that made with bare Aquivion membrane and EMI-Tf, as shown previously in Chapter 3 Section 3.1 (Figure 3-1). [58]

5.3.2 Secondary ion mass spectroscopy (SIMS) spectra

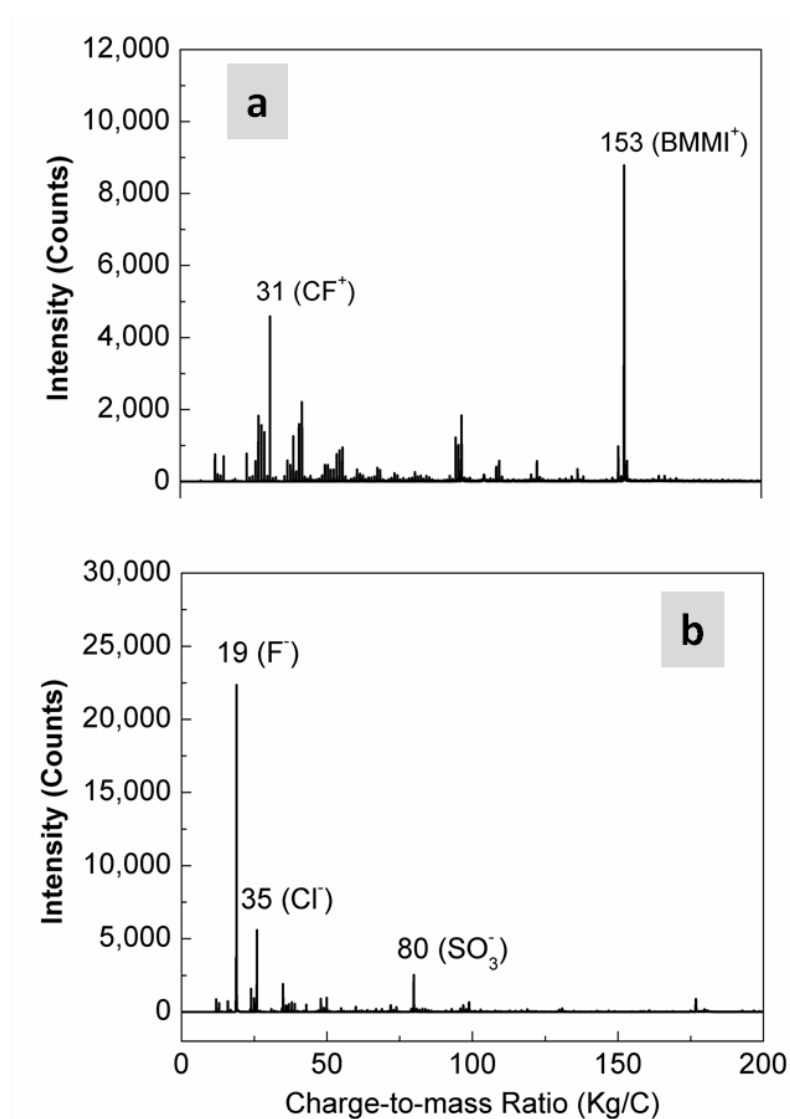


Figure 5-8 Mass spectra of (a) positive ions and (b) negative ions

Samples charged at 105 °C in Figure 5-6 were frozen and then depth profiled by ToF-SIMS with C_{60}^+ ions at liquid nitrogen temperature. Figure 5-8 (a) and (b) display the mass spectra of positive ions and negative ions.

From the mass-to-charge ratio in Figure 5-8 (a), 31 is recognized as polymer fragment CF^+ , and 153 is the molecular ion of cation $BMMI^+$. Besides anion Cl^- (19), polymer fragments F^- (19) and SO_3^- (80) were labeled in Figure 5-8(b) too. F^- (19) and CF^+ (31) come from the Teflon backbone of Aquivion, while SO_3^- (80) is on the side group of the polymer. The integrity of $BMMI^+$ is able to be preserved during C_{60}^+ sputtering. Peaks of interest, $BMMI^+$ (153) and Cl^- (19), were tracked for depth profile. Sputtering time was converted into depth by measuring the depth of the craters and calculating the sputtering rate. An average sputtering rate $1.48 \pm 0.15 \text{ nm/s}$ was obtained from Table 5-1.

Table 5-1 Sputter rate calculated from multiple sputtering craters

Sample #	Sputter Time (s)	Depth (um)	Sputter Rate (nm/s)
dp0	1080	1.6	1.48
dp1	4740	6.41	1.35
dp2	3540	4.63	1.31
dp3	3750	6.58	1.75
dp4	4950	7.49	1.51

5.3.3 Depth profile

Control data of Aquivion with 45 wt% $BMMI-Cl$ is presented in Figure 5-9. It could be seen that without voltage bias, the counts of both the ions and polymer fragment do not change with depth. It is notable that the first data point in each data set, which represents the surface condition of the film, differs from the signal from the bulk.

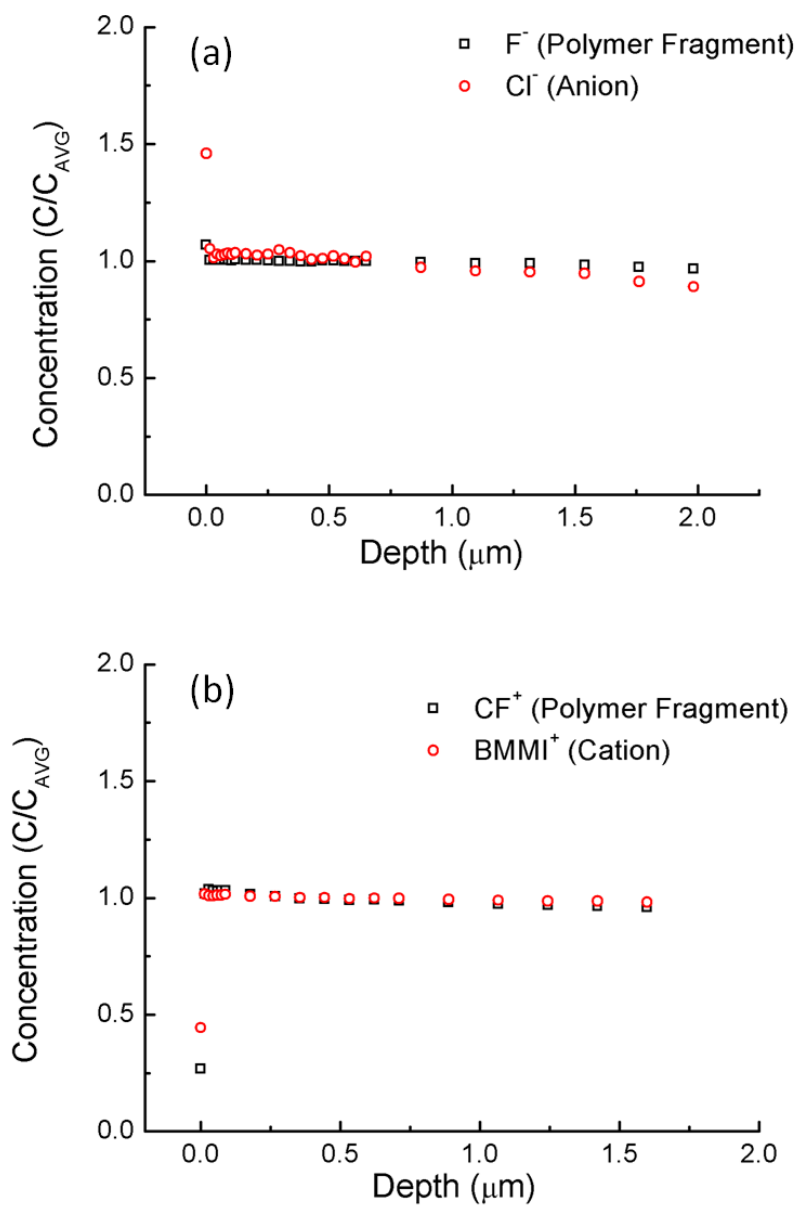


Figure 5-9 Control signal of Aquivion with 45 wt% BMMI-Cl ionic liquids (a) F⁻ and Cl⁻ (b) CF⁺ and BMMI⁺ without electrical bias

Under electrical field, the ions migrate and accumulate near the electrodes. The charge on the actuator slowly saturated after charging at 2.5V for 5 min due to the screening of electric field by the ions near the electrodes, which are a compact layer and a diffuse layer. In this case, the bulk of the ions in the middle of the membrane remain un-polarized. Figure 5-10 (a) and (b) are

depth profiles of the relative concentration of the cations and anions, with respect to the counts from plateau region in the center of the membrane.

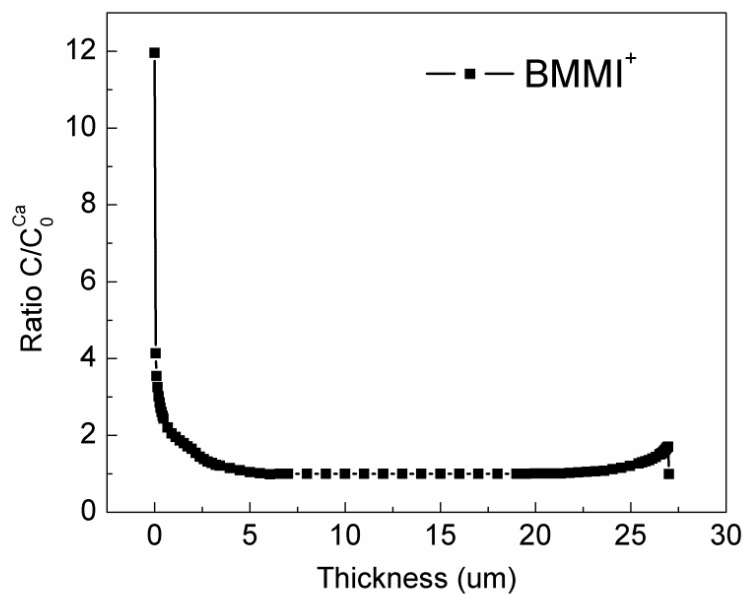


Figure 5-10. Cation distribution normalized by its middle region Counts (thickness is 0 μm at cathode; thickness is 27 μm at anode)

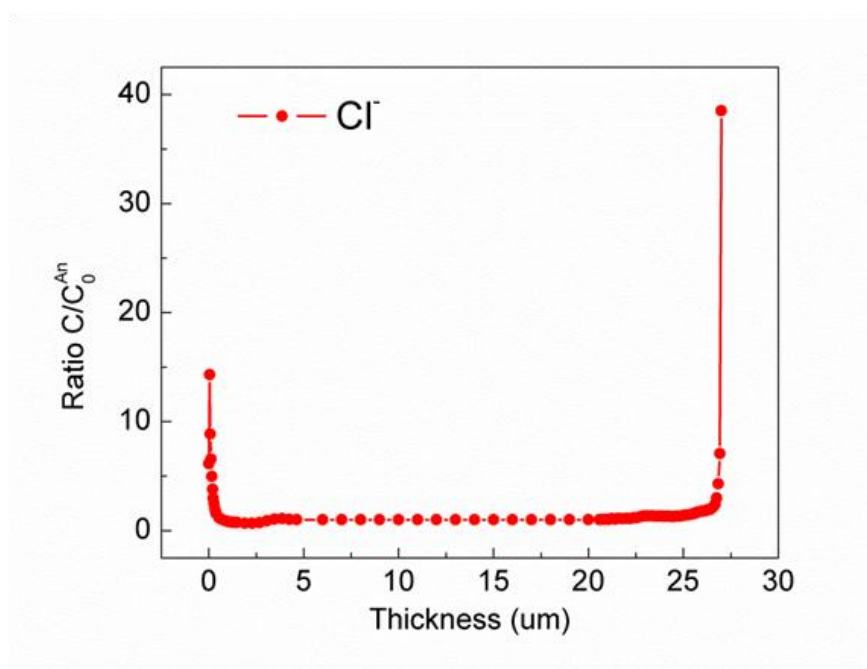


Figure 5-11. Anion distribution normalized by its middle region counts (thickness is 0 μm at cathode; thickness is 27 μm at anode)

The intensity of the polymer fragments (F^- and CF^+) were normalized to their averages and presented in Figure 5-12, which shows the surface roughness 167nm from Table 5-2 does not accredit for the features in Figure 5-11 (a) and (b). However, since the first points of CF^+ are far below 1, they indicate all the first points on the polymer/gold interface might be questionable due to the complexity of the interface, while the rest of the ion distribution is effectively preserved by the polymer matrix confinement.

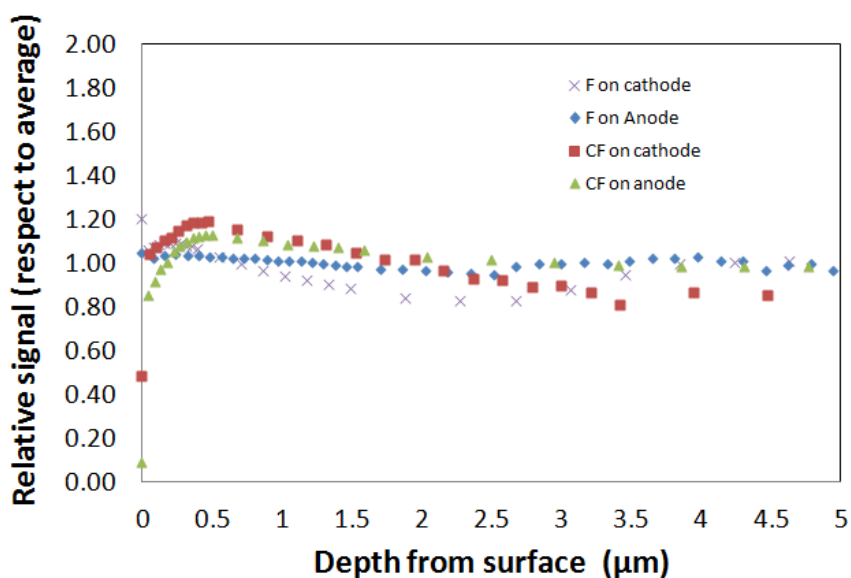


Figure 5-12. Depth profile of polymer fragments under charged condition (2.5V)

Table 5-2 Roughness test results of Aquivion membrane with 45 wt% of BMMI-Cl

Average roughness (Ra)	
Run 1	142nm
Run 2	186nm
Run 3	172nm

5.3.3.1 Ion aggregation

The increases of cations in anode and anions in cathode could be explained primarily by the strong Columb short-range correlation that exists between cations and anions. In devices operating with ionic liquids, the applied electric field reaches maximum upon the onset of voltage bias, and then decreases with the screening takes place over time. The maximum electric field could be calculated by the following equation,

$$E_{\max} = \frac{V}{\epsilon d} \quad (5.1)$$

where V is the applied voltage, ϵ is the dielectric constant of the membrane, and d is the film thickness. It gives $9.3 \times 10^{-3} \text{ V}/\mu\text{m}$ by estimating the dielectric constant of ionomer soaked with ionic liquids at 10.[58]

The local electric field between cation and anion can also be calculated from the diameter of cation and anion and an estimation of the dielectric constant of the neat ionic liquid at 15 by the following formula,

$$E = \frac{e}{4\pi\epsilon r^2} \quad (5.2)$$

where e is the elementary charge, ϵ is the macroscopic dielectric constant of neat ionic liquids, and r is the sum of the cation and anion radius. This electric field for BMMI-Cl is as large as $69 \text{ V}/\mu\text{m}$. [58, 114] It can be easily seen that the local electric field between ions turns out about 4 orders of magnitude higher than the maximum electric field that applied by voltage bias.

Macroscopically, one might consider the ions “clusters” in transport and storage as reported in former device studies.[108, 115] The Bjerrum length L_B , which is the ion separation length when the electrostatic interaction is comparable to the thermal energy, can be calculated from the following equation,

$$L_B = \frac{e^2}{4\pi\epsilon k_B T} \quad (5.3)$$

where e is the elementary charge, ϵ is the dielectric constant of the neat ionic liquids, k_B is the Boltzmann constant, and T is temperature. L_B is calculated as 3.7nm for BMMI-Cl. This length scale is much larger than the ion sizes (<1nm), hence lead to the intense aggregation of ions.

Microscopically, recent theoretic simulations of ionic liquids (by Bazant et al.), as introduced earlier in this chapter, [109, 116] could be used to conceptually explain the phenomena, as displayed in Figure 5-13. Since these approaches modified PNP equations to include the steric effect and the long range Columb ion correlation (mean field theory), they successfully show the accumulation of both cation and anion near the anode (charge inversion).

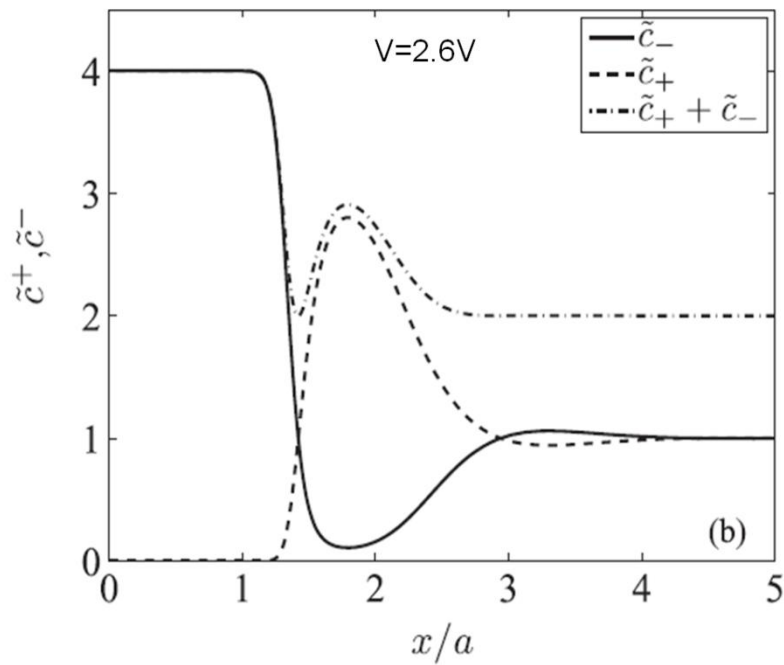


Figure 5-13 Voltage-dependent double-layer structure predicted by Bazant et al. Dimensionless cation (solid curve) and anion (dashed curve) concentrations and mass density (dash-dotted curve) at high voltage, $\tilde{V} = eV / kT$. ($V=2.6V$ when $\tilde{V}=100$) Position x is measured from the distance of closest approach and scaled to the ion diameter $a=10\text{\AA}$. Model parameters $\gamma=0.5$, which is the ratio of the bulk ion density to the maximum possible density, electrostatic correlation length $\delta_c = l_c / \lambda_D = 10$, and $\epsilon = 5\epsilon_0$ are those fitting ion profiles in simulations [109]

However, these approaches applied the mean field theory so that they do not fully reflect the high field response and all the features of ILs (e.g. chemical potential). PNP equations are “mean-field approximations”, which describe how discrete ions are affected by the mean concentrations, potential and dielectric constants. Each ion migrates in the mean electric field, which is produced by the mean charge density, not by the discrete, fluctuating charges in the ionic system, particularly, not by their neighbor ions. Therefore, PNP equations physically cannot describe ionic liquids, where each ion is strongly affected by its neighbors. Only under low electric field, where ionic liquids possess linear dielectric response, PNP can be adopted.[58]

Hence, as mentioned in Chapter 2 section 2.3.2.2, the traditional understanding of the electric double layer, such as Gouy-Chapman-Stern (GCS) model and current PNP based theories, may not be valid for high field and our experimental results here show that it is indeed the case. By comparing Figure 5-10 and 5-11, the semi-quantitative information of the ion accumulation (mainly diffuse layer) thickness can be obtained from the etching depth to reach the plateau C_0^{Ca} region and the plateau C_0^{An} region, where the value of BMMI^+ is about 6 μm and that of Cl^- is about 0.5 μm . But in current PNP based theories, the total ion accumulation layer is only on the nanometer scale.[57] As shown in Figure 5-13, the ion diameter a is assumed as 10Å, and under 2.6V the ions are only packed in a $3a$ -thick layer.

Electrically, previous experimental studies of ionic liquids by Lin and Zhang suggested that, the charges accumulated due to ion drifting ($t < \text{ms}$) are much smaller than those from ion diffusion ($t > \text{ms}$), as displayed in Figure 5-14.[58] For an ionic system that contains 40wt% of ionic liquids, PNP based theories are found valid at short time scale, where drifting ions form a screening layer with a Debye length $\sim 1\text{nm}$ and can be regarded as small perturbation to the entire system.[58] At high voltage and large time scale (e.g. $V=2\text{V}$), the total capacitance rapidly grows with time, indicating the dominance of diffuse ions and the formation of a thick diffuse ion layer, which is in agreement with the observations in Figure 5-10 and 5-11.

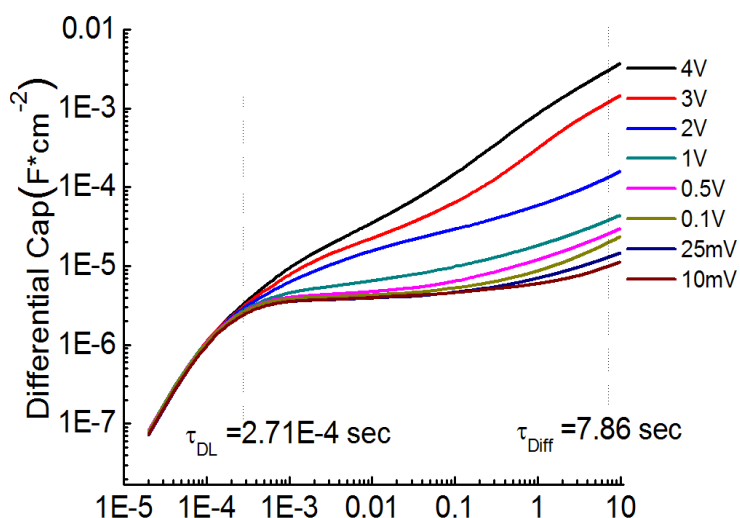


Figure 5-14 Capacitance of Aquivion with 40 wt% EMI-Tf at different voltage and different time scale. (unpublished data from MURI ILEAD presentation by Zhang and Colby)

Mechanically, nanometer thick ion accumulation layer cannot drive the significant bending of 27 μm thick film. Despite the other possible reasons that may contribute to this difference, our experimental results suggest the gap between current theories and the complex electric behavior of ionic liquids, which can be regarded as one type of concentrated electrolytes.[117, 118]

Therefore, based on the experimental observations stated above, a picture of the ion distribution under electric bias in this dissertation is illustrated in Figure 5-15.

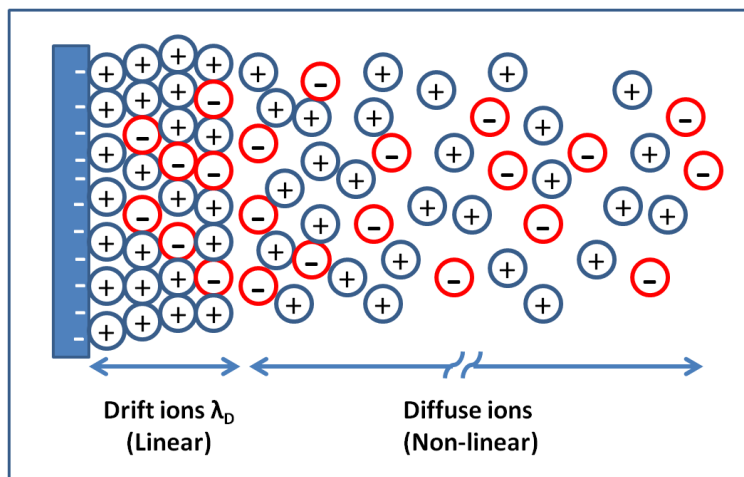


Figure 5-15 Schematic diagram of ion distribution in ILs near a charged planar surface.

This picture represents the experimental observations that are displayed in Figure 5-10, 5-11 and 5-14, where drift ions linearly respond to the external field and the diffuse ions non-linearly respond to the external field. When the perturbation to the ion concentration is small (short time scale), the ionic liquids can be considered to follow GCS model. In this case, we adopt the traditional electric double layer theory and name the linear charge response as “electric double layer” for convenience in previous chapters. However, in most of the cases, even when small voltage is applied, diffuse ion cannot be ignored (corresponding to Warburg impedance in AC characterization). Particularly, under high external field and at long time scale, diffuse ions dominate the total capacitance and the ion accumulation depth.

Certainly, ionomer matrix, which possesses a lower dielectric constant and occupies more than 50% volume, may affect the ion transport and storage of ionic liquids. But since ionic liquids are exclusively confined in the ion channels of the ionomer matrix, [30, 119] the fundamentals of pure ionic liquids should be physically valid for *i*-EAP actuators, and the resulted dimensions should be in the same order of magnitude. In order to capture the physical behavior of ionic liquids under high field in ionic devices, future theory research need to further improve the governing equations of the ionic system [64] and include more detailed microscopic information of ionic liquids, such as short range ion correlation, ion size,[120] and shape.

Furthermore, as illustrated in Figure 5-16, tail aggregation of cations in the ionic liquids, which was previously reported by molecular dynamics (MD) simulation,[121-124] wide-angle X-ray scattering, [125, 126] and small angle neutron scattering measurements,[127] may also contribute to the cluster formation.

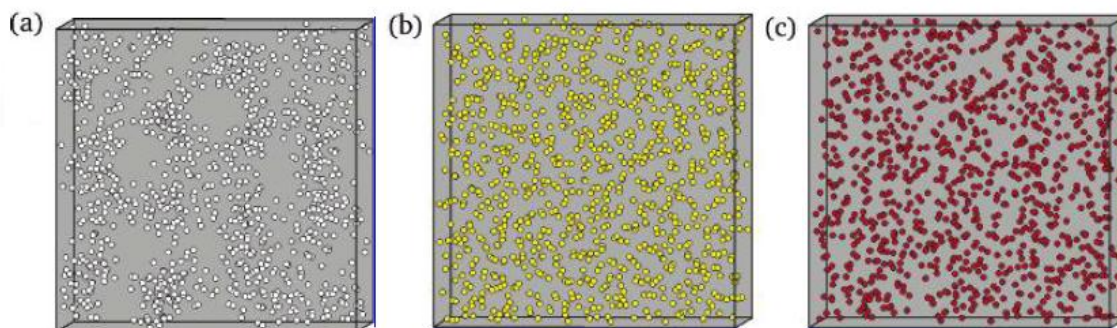


Figure 5-16 One snapshot of BMI-NO₃ with 1000 ion pairs at T=700 K with (a) tail groups only, (b) head groups only, and (c) anions only.[123]

It could be inferred that various ion clusters resulted from Coulomb short-range force and cation structure dramatically affect the transport and storage of ions in ionic liquid base devices.

5.3.3.2 Asymmetry of ions

Besides the observation of ion clustering, another important finding that needs to be addressed is the asymmetry of cations and anions.

From Figure 5-10 and 5-11, the ratio of diffuse layer thicknesses of cations and anions is about 12, which indicates that Cl⁻ ions compacted denser near the surface while the BMMI⁺ ions spread into certain depth due to their comparably larger size. Although ions tend to aggregate near the electrodes, the overall diffuse layer thickness of each type of ions is still strongly influenced by its ion size, where the volume of BMMI⁺ is 17 times of the volume of Cl⁻. This difference leads to imbalance of volume change near the electrodes, and actuation.

Moreover, by assuming H⁺ on the sulfonic acid side group in Aquivion is completely replaced by BMMI⁺, the ratio between the number of BMMI⁺ and Cl⁻ in the system could be estimated to link the relative concentration of the BMMI⁺ and Cl⁻.

For the pure ionic liquid, the volume (0.439nm^3) of each ion pair could be calculated from the density (0.716g/cc) and the molecular weight (188.70g/mol) of the ionic liquids. Since the size of Cl^- is well known as 181pm , from the volume of ion pair and the volume of Cl^- , the volume of BMMI^+ and the number of ions in unit volume can be calculated. The volume of BMMI^+ and Cl^- are 0.414nm^3 and 0.025nm^3 , respectively. It is also known that the Equivalent Weight (EW) of Aquivion, BMMI^+ , Cl^- are 790g/mol , 153.24g/mol , and 35.45g/mol , respectively. Assume H^+ on the side chains in Aquivion are completely replaced by BMMI^+ , weight of cation to replace H^+ is $1/790\text{g/mol} \times 153.24\text{g/mol} = 19.4\text{wt}\%$. Therefore, the amount of Cl^- is $(45\text{ wt}\% - 19.4\text{ wt}\%) / 188.69\text{ g/mol} = 1.36 \times 10^{-3}\text{mol/g}$ and the amount of BMMI^+ is $2.62 \times 10^{-3}\text{mol/g}$. The ratio between numbers of BMMI^+ and Cl^- in the system is 1.93.

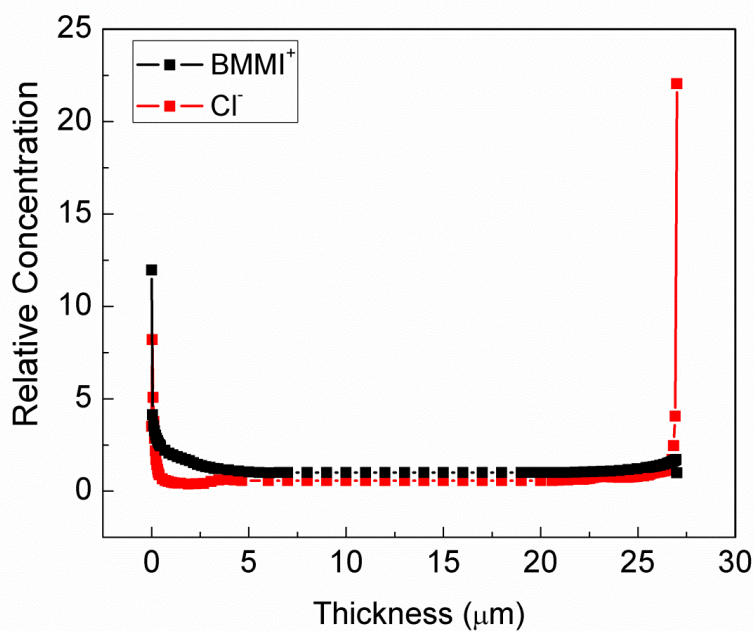


Figure 5-17 Estimation of relative ion concentration

Shown in Figure 5-17 is the estimation of relative ion concentration. It is interesting that the ion aggregation is more severe near the cathode than that of the anode, which might be caused by an underlying mechanism that small Cl^- may hop around the BMMI^+ ions or their “tail

aggregations” in its transport path, which causes effectively peeling off the BMMI^+ ions near the anode.

5.5 Conclusion

In summary, direct observations of the steady state ion distribution in an ionic polymer membrane actuator are conducted by employing Time-of-Flight Secondary Ion Mass Spectrometry (ToF-SIMS). Depth profiles of the cations and anions in charged Aquivion/BMMI-Cl actuator are obtained by ToF-SIMS at liquid nitrogen temperature.

Experimental results reveal that, due to a strong ion-ion Coulomb correlation and potential tail aggregation of cations, BMMI^+ and Cl^- accumulate near both cathodes and anodes. Their accumulation depths of reach 6 μm and 0.5 μm , respectively, which are primarily contributed by diffuse layer ions. This 12 times difference in thickness, together with asymmetric clustering near two electrodes, are mainly due to the size difference between cation and anion, which is the origin of strain in actuators. With the huge effective ion size difference in this ionic liquid, back relaxation was not observed. Since the ion distribution cannot be fully explained by current theories, which were originally built for dilute solutions, hence raises the demand of theory improvement. To summarize the experimental observations in this chapter and in references, a schematic diagram is presented to illustrate the layers of drift ions and diffuse ions, where drift ions and diffuse ion respond to external field linearly and non-linearly, respectively.

Chapter 6

Polymer in Ionic Polymer Actuators

6.1 Introduction

Since the polymer matrix in ionic polymer actuators play an important role in the electromechanical coupling process, the selection of polymer materials is crucial to the device performance. In this chapter, polymer matrices are intensively studied for improving the electromechanical energy efficiency of ionic polymer actuators.

Nafion, which is a perfluorosulfonic acid ionomer membrane, exhibits high ionic conductivity, good mechanical strength, and high chemical resistance and therefore has been widely used as a benchmark material in fabricating IPCNC actuators. As shown in Figure 6-1(a), the molecular structure of Nafion consists of polytetrafluoroethylene (PTFE) backbones, which serve as the high elastic modulus phase, and a double ether perfluoro side chains terminating in a sulfonic acid group. These sulfonic acid groups form a separated cluster phase with a lower glass transition temperature (T_g) than that of the backbone. With the presence of electrolytes, such as a polar solvent or a hydrophilic ionic liquid, the electrolyte molecules are exclusively contained in the clustered network, i.e. the ionic channels that are displayed in Figure 6-1(b).[30, 31, 119, 128] Although the ion channels are plasticized by the electrolyte molecules,[30, 128, 129] which facilitate fast ion transport, their effect on the mechanical coupling between stored excess ions near electrodes and the polymer backbone (high modulus phase) may be negative.

In principle, under an electric field, the accumulation or depletion of ions with different sizes causes volume changes near electrodes, and consequently generate actuation. As illustrated

in Figure 6-2, the flexible side chains of perfluorosulfonate ionomers may act as soft buffer layers between the PTFE backbones and the excess ions near the electrodes which damp the strain generated in the backbone by the excess ions. Because these flexible side chains are elastically much softer than the backbones, with the presence of large ion molecules, segmental motions of side chains within the backbone framework were observed by dynamic mechanical response,[30, 130] which is a sign of an ineffective electromechanical transduction. An effective elastic coupling of the stored ions with the high modulus phase of the polymer matrices is desired in achieving a high electromechanical transduction efficiency.

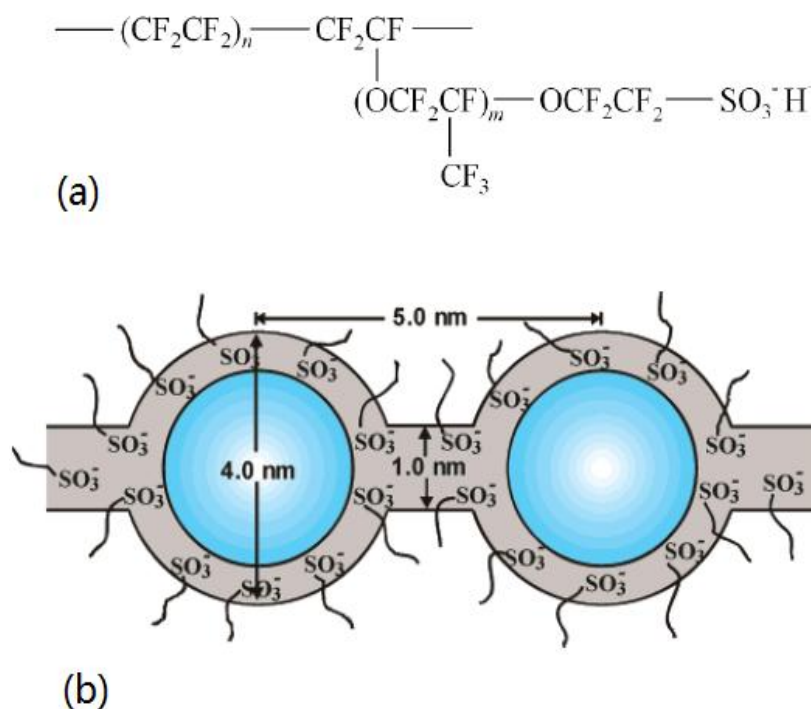


Figure 6-1 (a) The molecular structure of Nafion; (b) the cluster network morphology model by Gierke et al;[31]

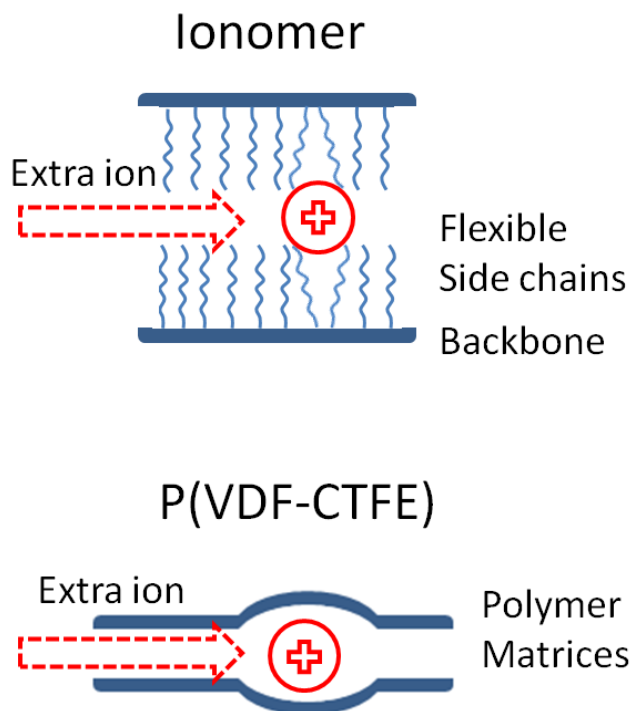


Figure 6-2 Schematics of perfluorosulfonate ionomers and P(VDF-CTFE) with an extra ion.

In this chapter, we investigate PVDF based polymer matrices, which do not have side groups in structures, such as fluoropolymer Poly[(vinylidene difluoride)-co-(chlorotrifluoroethylene)] (P(VDF-CTFE)) and poly(vinylidene fluoride-trifluoroethylene-chlorofluoroethylene) (P(VDF-TrFE-CFE)), for ionic polymer actuators. P(VDF-CTFE) and (P(VDF-TrFE-CFE) are known as ferroelectric EAPs that can be operated under high voltage.[131, 132] Since Poly(methyl methacrylate) (PMMA) has a Young's modulus as high as ~3GPa,[133] blending it with P(VDF-CTFE) will increase the stiffness of the polymer. Therefore, besides P(VDF-CTFE) and (P(VDF-TrFE-CFE), the cross-linked P(VDF-CTFE)/PMMA blends are also studied and compared with those of the perfluorosulfonate ionomers. Figure 6-3 shows the schematic of an ionic polymer membrane actuator with planar electrodes used in this study, which is a simple configuration that has a well controlled device structure and allows in-depth polymer material analysis.

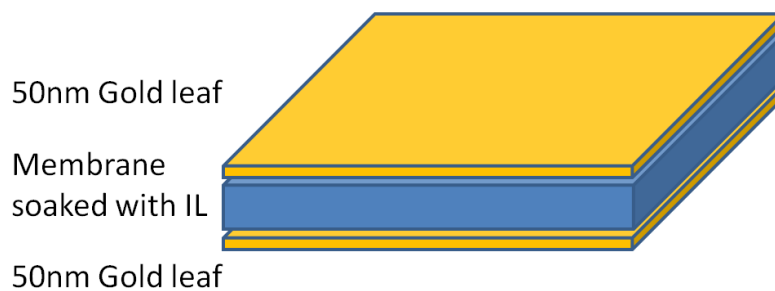


Figure 6-3 Composition of ionic polymer membrane actuator

Figure 6-4(a), (b) and (c) are the chemical formula of the polymers used in this study. All the ionic polymer membrane actuators in this study are 1 mm wide, 8mm long and 31-33 μm thick. The electrical, mechanical and electromechanical transduction properties of the ionic liquid containing membrane actuators made with the aforementioned polymers are investigated.

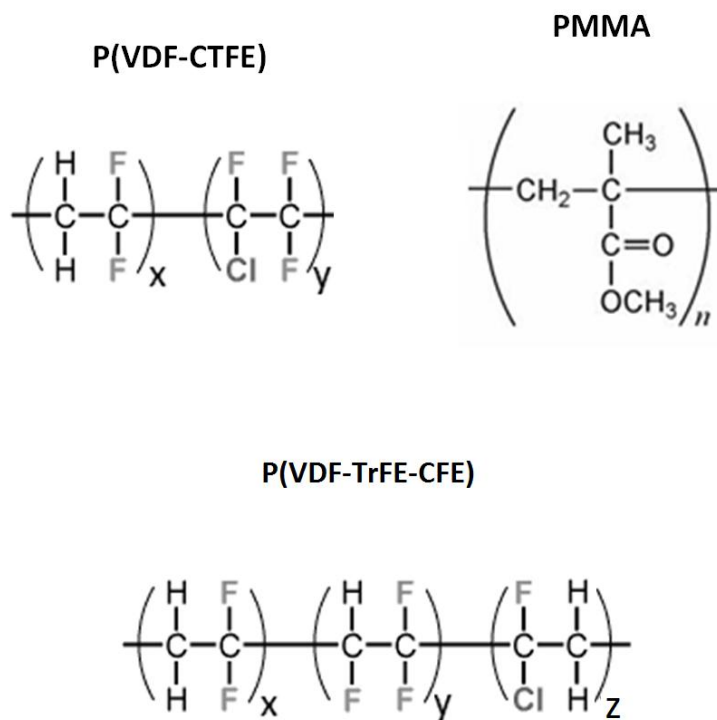


Figure 6-4 Chemical formula of (a) P(VDF-CTFE), (b) PMMA, and (c) P(VDF-TrFE-CFE)

6.2 Polymer Materials Fabrication

6.2.1 P(VDF-CTFE)

The preparation of the P(VDF-CTFE) films were carried out by means of solution-cast and followed by melt molding. P(VDF-CTFE) powder (Solvay Solexis, 31508) were first dissolved in Acetone under 50 °C. Once powders completely dissolved and the solution cooled back to room temperature, the solutions were then casted onto Teflon sheets that were laid flatly in a vented oven. After the solutions dried, the as-made films together with the Teflon sheets were transferred into a vacuum oven and dried overnight to remove the Acetone residue. Each film was then sandwiched by two Teflon sheets, hot-pressed under 2000~3000N at 240 °C for two hours, and followed by a water cooling process. The as-made samples are referred to as “P(VDF-CTFE)”.

6.2.2 Crosslinked P(VDF-CTFE)/PMMA

Similar to the fabrication of P(VDF-CTFE) films, mixtures of P(VDF-CTFE) powder (80 wt%) and PMMA powder (Aldrich, 182230) (20wt%) were first dissolved in Acetone under 50 °C. Once powders completely dissolved and the solution cooled back to room temperature, the solutions were then casted onto Teflon sheets that were laid flatly in a vented oven. After the solutions dried, the as-made films together with the Teflon sheets were transferred into a vacuum oven and dried overnight to remove the Acetone residue. Each film was then sandwiched by two Teflon sheets, hot-pressed under 2000~3000N at 240 °C for two hours, and followed by a water cooling process. The as-made samples are referred to as “P(VDF-CTFE)/PMMA blends”. To fabricate slightly crosslinked P(VDF-CTFE)/PMMA material with higher modulus, 2wt% of

initiator 2,3-dimethyl-2,3-diphenylbutane (Bicumene) was added into the solution before casting and followed by the same process. The as-made sample is referred to as “P(VDF-CTFE)/PMMA”.

6.2.3 Crosslinked P(VDF-TrFE-CFE) terpolymer

P(VDF-CTFE-CFE) powders were synthesized by Piezotech S.A.S., France, of which the molar ratio of VDF/TrFE/CFE is 65.3/27.4/7.3. The powders were first dissolved in Acetone under 50 °C. Once powders completely dissolved and the solution cooled back to room temperature, 2wt% of initiator 2,3-dimethyl-2,3-diphenylbutane (Bicumene) and 2wt% of 1,3,5-Triallyl-1,3,5-triazine-2,4,6(1H,3H,5H)-trione (TAIC) were added into the solution. Bicumene is an initiator and TAIC is a crosslink agent. Different from P(VDF-CTFE) and P(VDF-CTFE)/PMMA, pure P(VDF-TrFE-CFE) films with low crosslink density dissolves in ionic liquids electrolyte, therefore, a crosslink agent TAIC is introduced into the process to increase the crosslink density of the film. The solutions were then casted onto Teflon sheets that were laid flatly in a vented oven. After the solutions dried, the as-made films together with the Teflon sheets were transferred into a vacuum oven and dried overnight to remove the Acetone residue. Then the film was sandwiched by two Teflon sheets, hot-pressed under 2000~3000N at 240 °C for two hours, and followed by a water cooling process. The as-made samples are referred to as “P(VDF-TrFE-CFE)”. To calculate the gel content of P(VDF-TrFE-CFE), the weight of the film was measured before and after Acetone rinse. The Acetone rinse was done by soaking the polymer film in Acetone at 70 °C for two hours, completely removing Acetone and then drying the film with vacuum.

6.2.4 CNCs with P(VDF-CTFE)/PMMA and RuO₂ nanoparticles

Mixtures of P(VDF-CTFE) powder (80 wt%) and PMMA powder (Aldrich, 182230) (20wt%) were first dissolved in Acetone under 50 °C. Once powders completely dissolved and the solution cooled back to room temperature, a water dispersion of RuO₂ nanoparticles (40 vol% respect to Nafion) and 2wt% of initiator 2,3-dimethyl-2,3-diphenylbutane (Bicumene) was added into the solution. The mixture was then sonicated and sprayed onto the two surfaces of a P(VDF-CTFE)/PMMA membrane until the CNC thickness reaches 3 µm. After spraying, the film was dried in vacuum oven overnight to remove the Acetone and water residue. Finally, the film was sandwiched by two Teflon sheets, hot-pressed under 300N at 240 °C for two hours, and followed by a water cooling process.

6.2.5 Actuator fabrication and characterization

Membranes of P(VDF-CTFE), crosslinked P(VDF-CTFE)/PMMA, Nafion (Dupont, 211), Aquivion (Solvay Solexis, 7903), P(VDF-CTFE)/PMMA IPCNC, and ionic liquid EMI-Tf (Aldrich) were dried in vacuum at 80 °C to remove moisture before processing. Polymer membranes swollen with 40wt% EMI-Tf were prepared by soaking the membranes in EMI-Tf at 60 °C on a VWR hotplate. The uptake of ionic liquids within membranes was calculated by measuring the weight gain after swelling. 50 nm thick gold foils (L.A. Gold Leaf) were then hot-pressed at 90 °C on both sides of the membranes as electrodes. The final pure ionic polymer membrane actuators had a thickness 31-33 µm and the P(VDF-CTFE)/PMMA IPCNC has a total thickness of 38 µm.

The storage moduli of the membranes were measured by dynamic mechanical analyzer (TA DMA 2980 Dynamic Mechanical Analyzer) and the heat flow characteristics of the samples

were measured by differential scanning calorimetry (TA DSC Q100). The electrical measurement was carried out in a sealed box with desiccant inside to prevent the absorption of moisture and the electrical characteristics were measured by a potentiostat (Princeton Applied Research 2273). The electromechanical response was recorded by using a probe station (Cascade Microtech M150) equipped with a Leica microscope and a CCD camera (Pulnix 6740CL).

6.3 Results and Discussions

6.3.1 Mechanical properties

Table 6-1 Moduli of polymers without and with 40 wt% of EMI-Tf uptake

Polymer Composition	Young's Modulus at 25 °C (MPa)	
	Membrane with 40 wt%	
	Neat membrane	EMITf
Nafion	550	50
Aquivion	410	50
P(VDF-CTFE)	480	70
P(VDF-CTFE)/PMMA blends *	880	110
Crosslinked P(VDF-CTFE)/PMMA	1100	150
P(VDF-TrFE-CFE) *	175	N/A
Crosslinked P(VDF-TrFE-CFE)	470	50

* not characterized for actuator performance.

The moduli of the polymer membranes with and without EMI-Tf are summarized in Table 6-1. It is found that Nafion, Aquivion and P(VDF-CTFE) dry membranes have similar moduli, and by blending PMMA with P(VDF-CTFE), the young's modulus of the membrane is almost doubled from pure P(VDF-CTFE). To further increase the elastic modulus, 2wt% of an initiator (Bicumene) was added to P(VDF-CTFE)/PMMA blends in the fabrication process to

create crosslinks in the blends. After melting molding into a film at 240°C, the modulus of the P(VDF-CTFE)/PMMA film is increased 25% compared to the pure blend which is an indication of some degree of crosslinking in the blends. Pure P(VDF-TrFE-CFE) has a very low Young's modulus and dissolves in ionic liquids. To improve its Young's modulus and chemical stability, both 2wt% of an initiator (Bicumene) and 2wt% of a crosslink agent (TAIC) were added to P(VDF-TrFE-CFE) in the fabrication process to create crosslinks in the polymer. After melting molding into a film at 240 °C, the modulus of the P(VDF-TrFE-CFE) film is increased ~150% compared to the pure polymer film, which shows a high crosslink density. This finding agrees with the high gel content value of the crosslinking 63.5%. Different from pure P(VDF-TrFE-CFE), after crosslinking, this polymer membrane no longer dissolves in ionic liquid electrolytes.

Using differential scanning calorimetry (DSC) and dynamic mechanical analysis (DMA), further investigation is conducted to evaluate the crosslinking on the properties of the membranes and presented. The thermograms of P(VDF-CTFE)/PMMA blends with and without initiator are compared to those of pure polymers in Figure 6-5. The data reveals that the films with initiator exhibit higher transition as well as decomposition temperatures than those of blend without initiator. As an examples, the DSC curve in Figure 6-6 shows that the major decomposition peak of PMMA (~320°C) in the crosslinked sample shifted to higher temperature (~400°C).[134] The thermograms and DSC curve of P(VDF-TrFE-CFE) with and without crosslinking are compared in Figure 6-7 and 6-8. The modulus of P(VDF-TrFE-CFE) significantly increases with crosslinking that indicates a high crosslinking density in the film. The melting temperature of P(VDF-TrFE-CFE) decreases with crosslinking due to decrease in crystallinity.

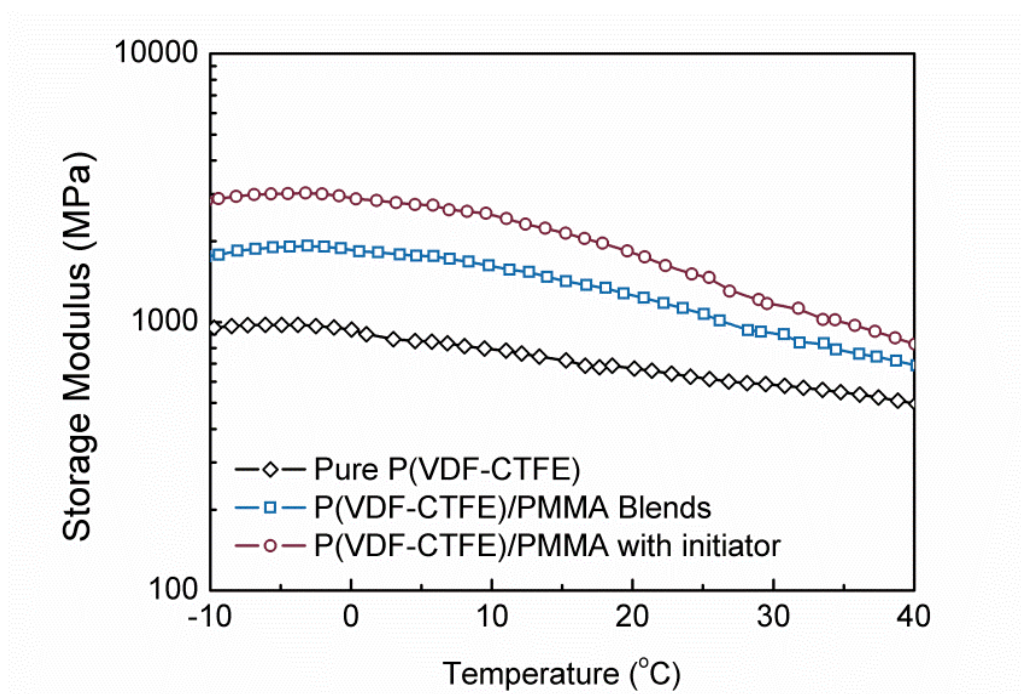


Figure 6-5 DMA curve of P(VDF-CTFE), P(VDF-CTFE)/PMMA blends (without initiator), and P(VDF-CTFE)/PMMA with initiator

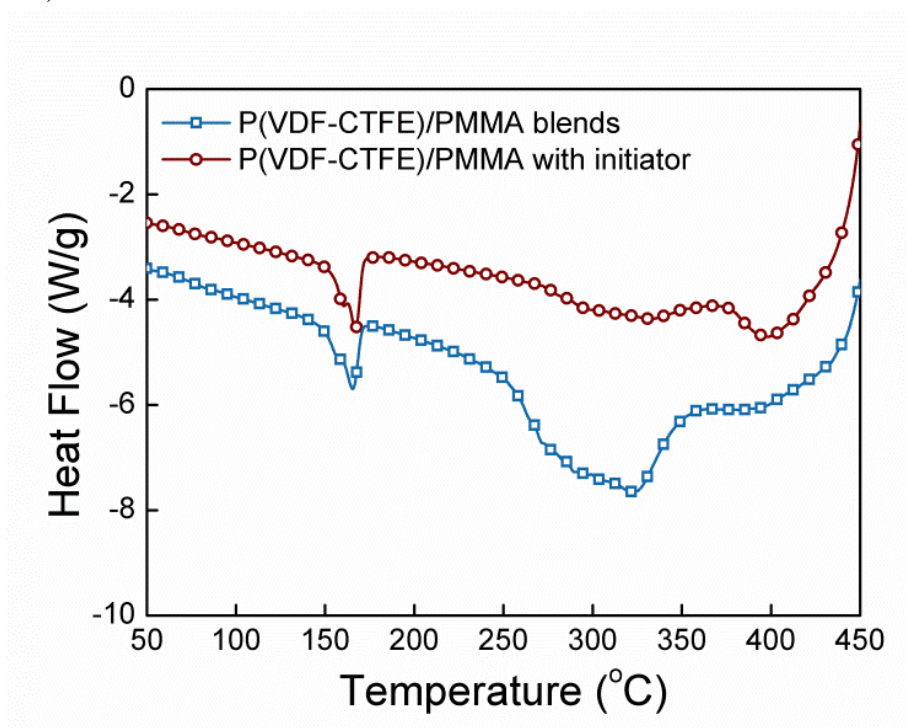


Figure 6-6 DSC curve of P(VDF-CTFE)/PMMA blends (without initiator) and P(VDF-CTFE)/PMMA with initiator

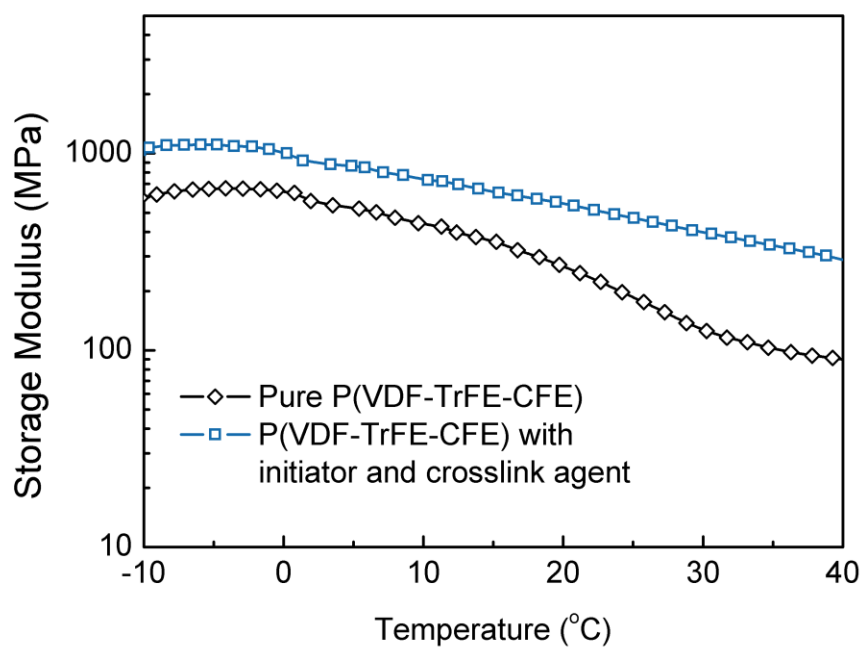


Figure 6-7 DMA curve of P(VDF-TrFE-CFE) without and with initiator and crosslink agent

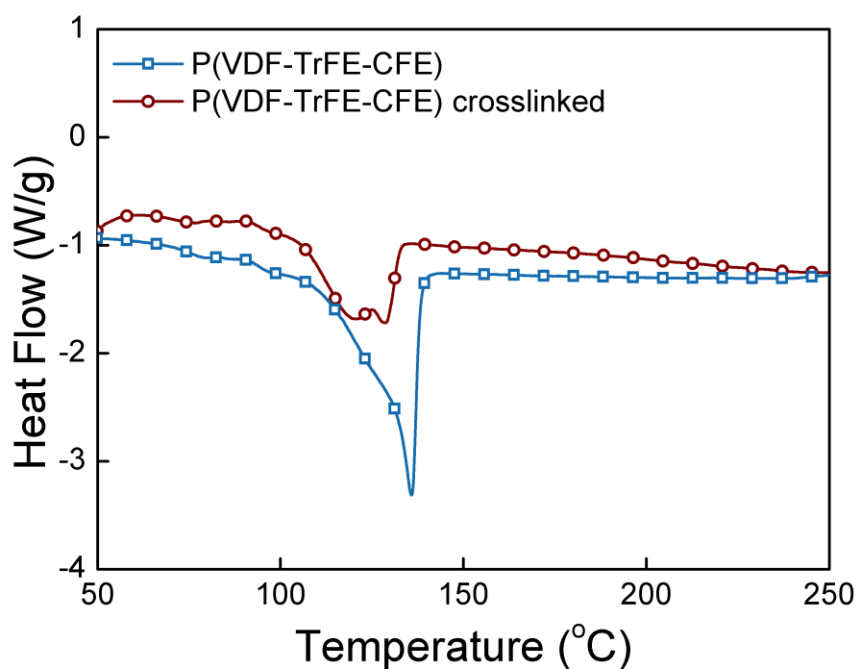


Figure 6-8 DSC curve of P(VDF-TrFE-CFE) without and with initiator and crosslink agent

Nafion and Aquivion are perfluorosulfonate ionomers that share the similar nano-structure, in which Aquivion has a shorter side chain length than Nafion does.[58, 135, 136] As shown in Table 6-1, after swelling with 40 wt% of EMI-Tf, the moduli of Nafion and Aquivion membranes reduced significantly, from more than 400MPa to 50MPa due to the plasticizing effect of the ionic liquid molecules. Analogously, with 40 wt% EMI-Tf, the moduli of PVDF based materials are also reduced. However, with the same amount of IL uptake, the moduli of all these PVDF based membranes are still higher than or equal to that of Nafion and Aquivion.

Actuator performance from three new materials, P(VDF-CTFE), crosslinked P(VDF-CTFE)/PMMA and crosslinked P(VDF-TrFE-CFE), is characterized and compared with that from the tradition ionomers, namely Nafion and Aquivion. The blend of P(VDF-CTFE) and PMMA without crosslinking is characterized for the purpose of investigating the crosslinking density, and thus is not further studied for the electromechanical responses.

6.3.2 Electrical properties

The frequency-dependent conductivity of five ionic polymer membrane actuators is presented in Figure 6-9, where the plateau region at high frequencies corresponds to the dc conductivity σ_0 of the material system. With 40 wt% uptake of EMI-Tf, Nafion and Aquivion exhibit a relatively higher σ_0 (1.9×10^{-4} S/cm and 1.3×10^{-4} S/cm, respectively), which is due to the percolated ion channels and presence of flexible side chains, than those of P(VDF-CTFE) (1.4×10^{-5} S/cm), P(VDF-CTFE)/PMMA (0.7×10^{-4} S/cm), and P(VDF-TrFE-CFE) (2.5×10^{-5} S/cm). Interestingly, the data also show that adding PMMA not only increases the elastic modulus but also improves the ionic conductivity. This implies that the presence of PMMA provides some degree of “ion channels” which facilitate the ion transport. It is well known that PMMA is

miscible with P(VDF-CTFE) in amorphous phase which may create nano-inter-phase regions between the two polymers, facilitating ion transport.[137]

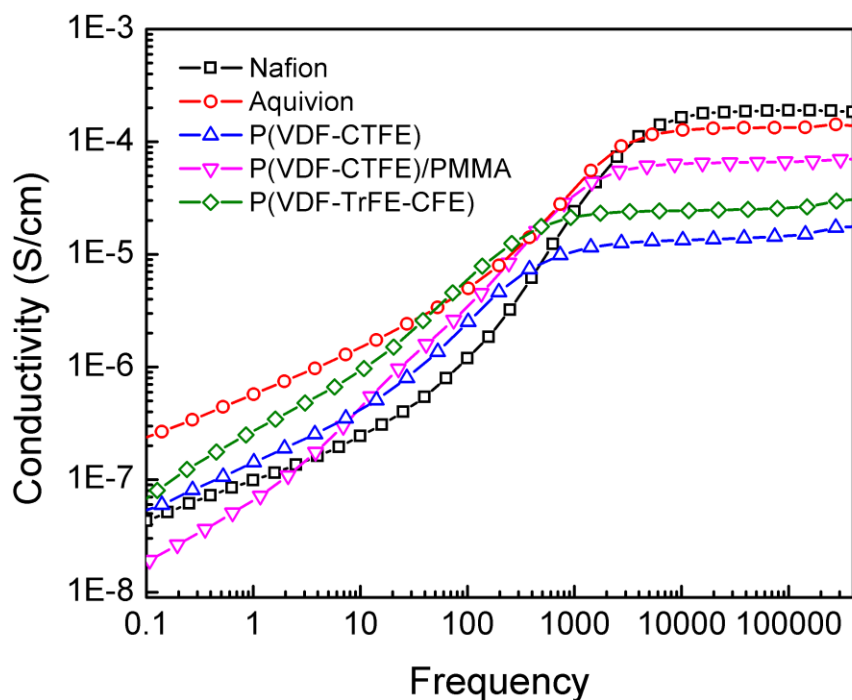


Figure 6-9 Frequency-dependent conductivity of the five types of ionic polymer membrane actuators with 40 wt% EMI-Tf under a 4 V step voltage

Presented in Figure 6-10 is the charge responses of five ionic polymer membrane actuators made with Nafion, Aquivion, P(VDF-CTFE), cross-linked P(VDF-CTFE)/PMMA, and P(VDF-TrFE-CFE) under a 4V step voltage. With the same weight percentages (40 wt%) of EMI-Tf uptake, Nafion and Aquivion membranes consume ~70-100% more charge than those of PVDF based membranes. The higher charge densities and conductivities of Nafion and Aquivion with ionic liquids could be attributed to the ion channels that facilitate the ion transport and accommodate more ions.

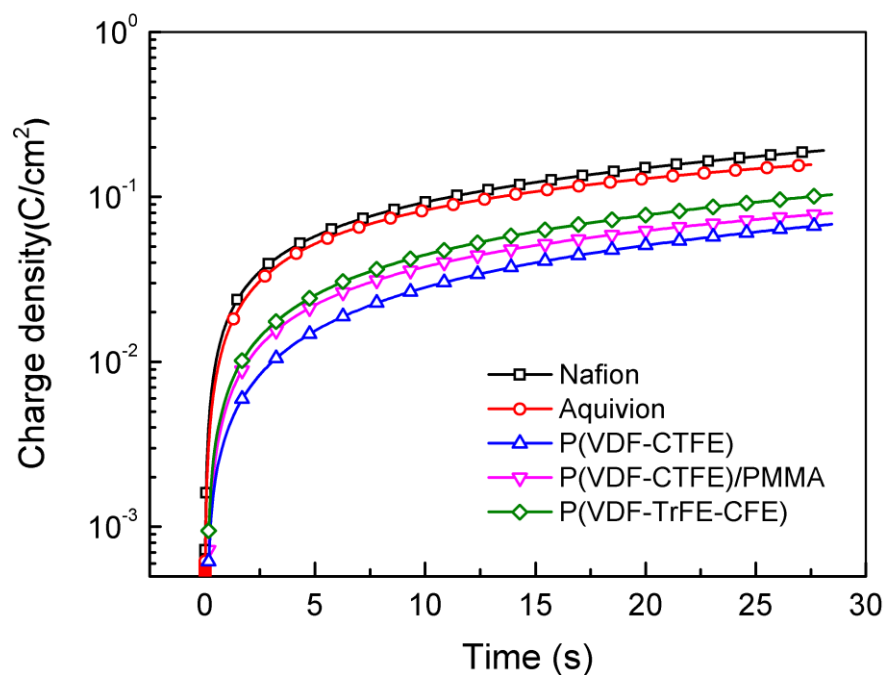


Figure 6-10 Charge density of the five types of *i*-EAP membrane actuators with 40 wt% EMI-Tf under a 4 V step voltage

It is noticed that due to the difference in polymer density, the corresponding volume percentages of the EMI-Tf content in the films vary slightly, which may affect the electrical performances of the devices. However, since the observed difference in EMI-Tf volume percentage in different films is within 5%, it is unlikely to be responsible for the observed large difference (more than 100%) in charge stored at the electrodes between the ionomers and PVDF-based polymers.

6.3.3 Electromechanical coupling

6.3.3.1 Bending actuation

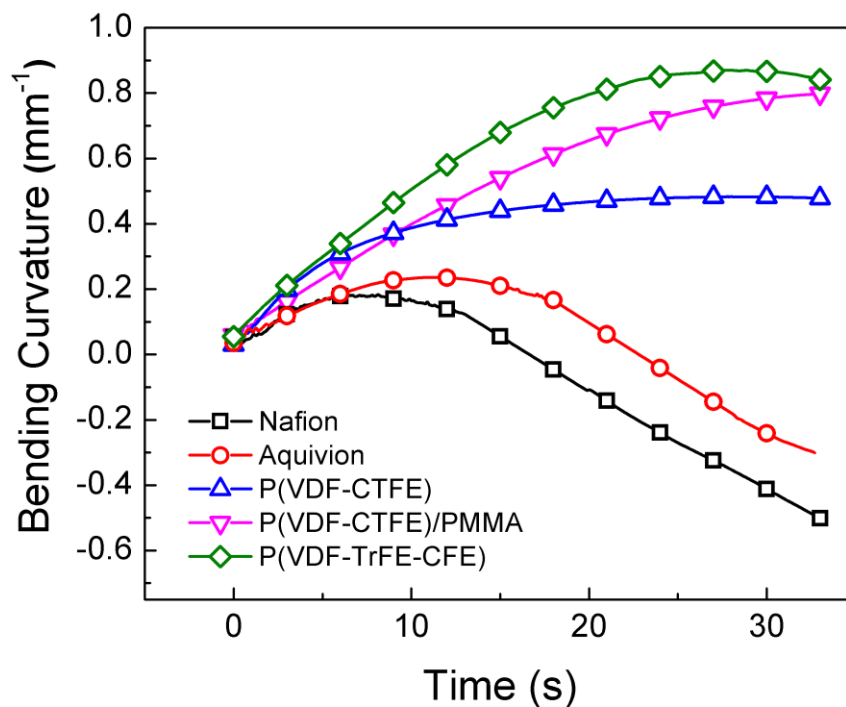


Figure 6-11 Bending curvature of the five types of ionic polymer membrane actuators with 40 wt% EMI-Tf under a 4 V step voltage

Figure 6-11 shows the evolution of the bending actuation of the five ionic polymer membrane actuators under a 4 V step voltage. As discussed in Chapter 3, the actuator initially bends towards the anode, and as the time progresses, it reverses the actuation direction and bends towards the cathode. This is an intrinsic properties of the ionic polymer actuators that caused by the two mobile ions in the actuation process.[108] As shown figure 6-11, P(VDF-CTFE), P(VDF-CTFE)/PMMA, and P(VDF-TrFE-CFE) all possess enhanced electromechanical responses compared to Aquivion and Nafion. P(VDF-CTFE) exhibits bending magnitude of 0.45 mm^{-1} and

a relatively faster initial strain (<10 s) response, which is an indication of better AC actuation for this materials which will be discussed in the next section. P(VDF-CTFE)/PMMA displayed a even higher strain response (0.75 mm^{-1}) at longer actuation time scale (>12 s). P(VDF-TrFE-CFE) showed the highest strain response (0.87 mm^{-1}) and the fastest initial strain response. As has been introduced in Chapter 2 and 3, the later stage strain response is mainly determined the by diffusion process of anions near the electrodes (due to the ion concentration gradient).All PVDF polymers bend back at larger time scales, which follows the 2-carrier model in Chapter 3.[58]

6.3.3.2 Stress charge ratio

The bending curvature, although is proportional to the net strain S through a relation $S = \kappa t \times 100\%$ and provides a straight-forward measure of the device performance,[70] is strongly affected by the modulus of the material. Therefore, neither the bending curvature nor the net strain could effectively quantify the electromechanical coupling between the ionic liquids and the polymer matrix. As shown in Table 6-1, the difference in Young's moduli between different materials is quite large, where P(VDF-CTFE)/PMMA with electrolyte exhibits 150MPa and Nafion and Aquivion with electrolyte have a Young's modulus of only 50 MPa.

To evaluate the capability of polymer materials in generating deformation regardless of their moduli, the intrinsic stress T_0 , as illustrated in Figure 6-12, can be deduced from the bending curvature and the Young's moduli of the membrane actuators as introduced in Chapter 2 Section 2.3.1.1.[138] Here we model the bending actuator as a bimorph beam with an assumption that an intrinsic extension stress $+T_0$ (contraction stress $-T_0$) is uniformly generated in the upper (lower) half of the polymer membrane, as shown in Figure 6-12. The intrinsic stress T_0 could be derived as follows,

$$T_0 = -\frac{Y_m(8t_m^3 + 12t_m^2t_i + 6t_mt_i^2) + Y_it_i^3}{3t_i^2} \cdot \kappa \quad (6.1)$$

where Y_i and Y_m are the Young's Moduli of the ionic polymer membrane layer and gold electrode, t_i and t_m are the thickness of the ionic polymer membrane and gold electrode respectively.

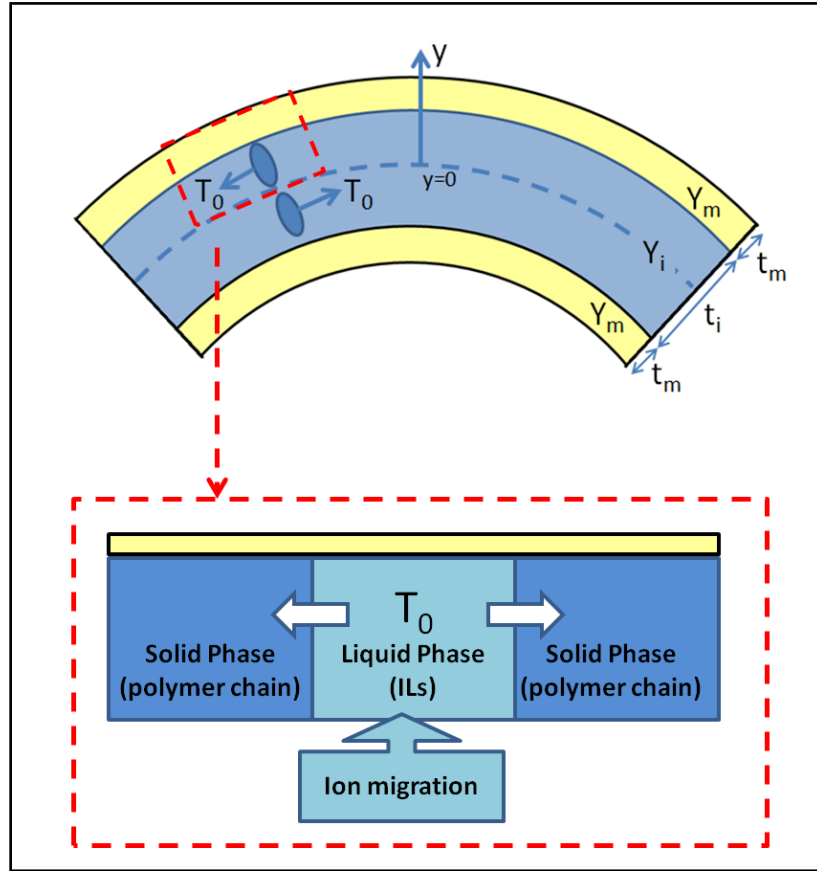


Figure 6-12 Schematic of a bimorph bending actuator with a 3-layer structure and a conceptual diagram of the microscopic interaction between ionic liquids and the polymer matrix.

It was noted that the intrinsic strain $S_0 (=T_0/Y_i)$ and the intrinsic strain-charge ratio S_0/C have been extensively discussed in Chapter 3 and in the literature,[78] respectively, when comparing ionic polymer actuators with similar moduli.[71, 78, 139] For comparison between ionic polymer membrane actuators with considerable modulus difference, the intrinsic stress-charge ratio T_0/C gives a better measure of the electromechanical coupling between the

electrolytes and the polymer matrix than S_0/C . As displayed in Figure 6-12, microscopically, the intrinsic stress T_0 can be considered as the pressure of the liquid phase (ionic liquids) on the solid phase (polymer). When the charging process introduces ion migration towards the gold electrode, a pressure is introduced, so that the effectiveness of the charges in converting into mechanical stress can be evaluated by T_0/C , as presented in Figure 6-13.

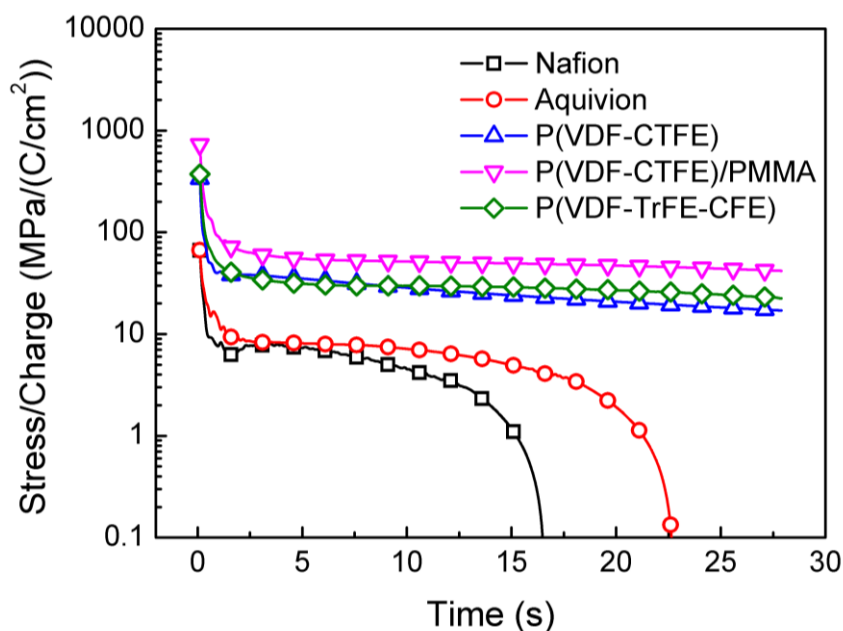


Figure 6-13 Stress charge ratio of the five types of ionic polymer membrane actuators with 40 wt% EMI-Tf under a 4 V step voltage

P(VDF-CTFE), P(VDF-CTFE)/PMMA and P(VDF-TrFE-CFE) show higher T_0/C values than those of Nafion and Aquivion ionomers in the entire actuation time scale. As has been discussed with Figure 6-2, it is highly possible that the flexible sulfonic acid side chains of the ionomers act as a buffer layer and reduced the stress/pressure generated through segmental motions. [30]

Besides the comparison between polymer matrices, it was also found that T_0/C slowly decreases with time, which implies that under a step voltage, charges accumulated within short

period of time (e.g. $t < 10$ s) are more effective in generating stress/strain. There are three possible reasons that superpose and lead to this phenomenon: (i) Cancellation in strains between the cations and anions when substantial anion diffusion occurs as discussed in Chapter 3.[108] (ii) as the diffuse layer grow thicker and the charges (in Figure 6-9) saturate, the Coulomb force between the electrons on the external gold electrode and the ions accumulated at a later stage becomes weaker, therefore they do not effectively generate stress; (iii) small leakage currents cause the measured charge grows with time, which may not be related to an actual ion motion.

6.3.3.3 Energy Efficiency under direct current (DC) stimulus

As shown in Figure 6-14, the mechanical energy density of the five *i*-EAP membrane actuators can be calculated from the bending curvature κ and the Young's moduli of the ionic polymer layer Y_i and the Au layer Y_m by the equation below,

$$u_m = \frac{1}{t_i + 2t_m} \left[\int_0^{\frac{t_i}{2}} Y_i (\kappa y)^2 dy + \int_{\frac{t_i}{2}}^{\frac{t_i}{2} + t_m} Y_m (\kappa y)^2 dy \right] \quad (6.2)$$

where y is the distance from the middle plane of the actuator.

Meanwhile, the electrical energy density u_e could be calculated as follows,

$$u_e = QV/At \quad (6.3)$$

where Q/A is the charge density, V is the applied voltage, and t is the total sample thickness. Hence, the electromechanical energy efficiency of the actuators can be deduced by the following relation.

$$\eta = u_m/u_e \times 100\% \quad (6.4)$$

As illustrated in Figure 6-15, P(VDF-CTFE), P(VDF-CTFE)/PMMA and P(VDF-TrFE-CFE) has achieved an order of magnitude higher energy efficiencies than Nafion and Aquivion, which makes them preferred materials for *i*-EAP actuators.

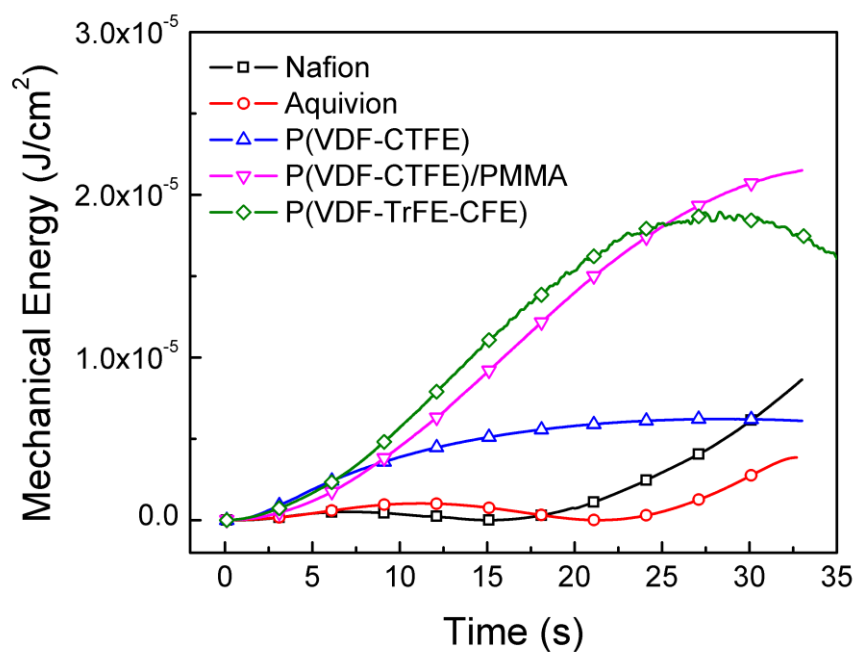


Figure 6-14 Areal mechanical energy of the five types of *i*-EAP membrane actuators with 40 wt% EMI-Tf under a 4 V step voltage. Since Nafion and Aquivion bends back to initial position at $t \sim 15$ -20s, their mechanical energy reaches zero at certain time.

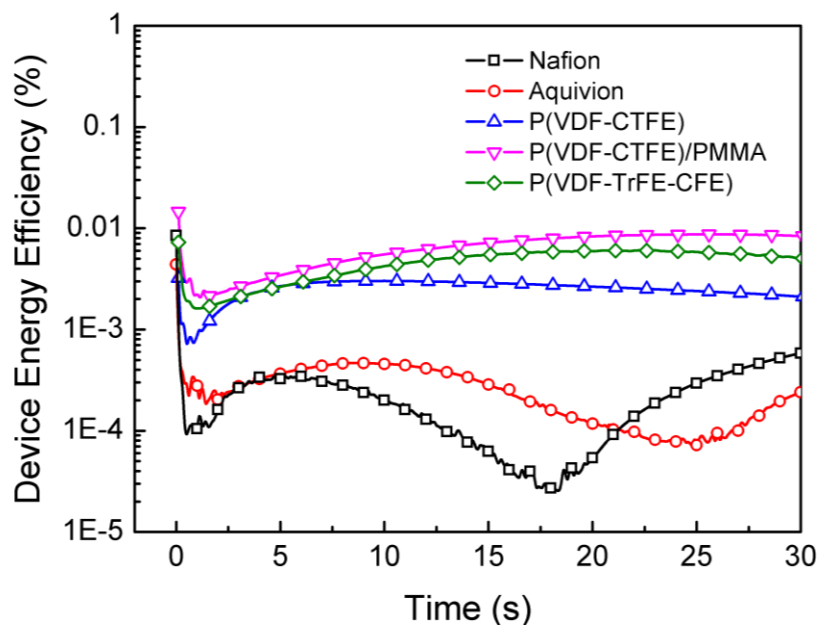


Figure 6-15 Device energy efficiency of the five types of ionic polymer membrane actuators with 40 wt% EMI-Tf under a 4 V step voltage

Although the electromechanical coupling and efficiency is significantly improved by utilizing P(VDF-CTFE) based materials, it is found that the efficiencies of these membrane actuators are still very low ($<0.1\%$), since their device configuration is not optimized for applications. *i*-EAP actuators (e.g. IPCNCs) are complex systems that are featured by many components, such as the electrolyte, polymer matrix and composite electrode. By adding conductor network composite (CNC) and varying the electrolyte, the electromechanical transduction efficiency, as well as the actuation speed, can be improved, as previously studied in literature, [78] discussed in Chapter 3 Section 3.3.2, and will be presented in Section 6.3.3.6 of this chapter.

6.3.3.4 Energy efficiency under alternating current (AC) stimulus

Since the electromechanical coupling between ionic liquids and the polymer matrix is stronger at a short charging time ($t < 10$ s) than a long time (Figure 6-13), a comparison of the five ionic polymer membrane actuators under AC stimulus is performed. An example of the AC response of ionic polymer membrane actuators under 4V 0.1Hz triangle wave is presented in Figure 6-16 and a comparison of the five membrane actuators studied is displayed in Figure 6-17.

Again, despite their large Young's moduli, PVDF based *i*-EAP membrane actuators have larger bending curvatures, while consuming less driving current than Nafion and Aquivion perfluorosulfonate ionomers, which confirmed that P(VDF-CTFE), P(VDF-CTFE)/PMMA and P(VDF-TRFE-CFE) are superior *i*-EAP actuator material candidates in effectively generating strain.

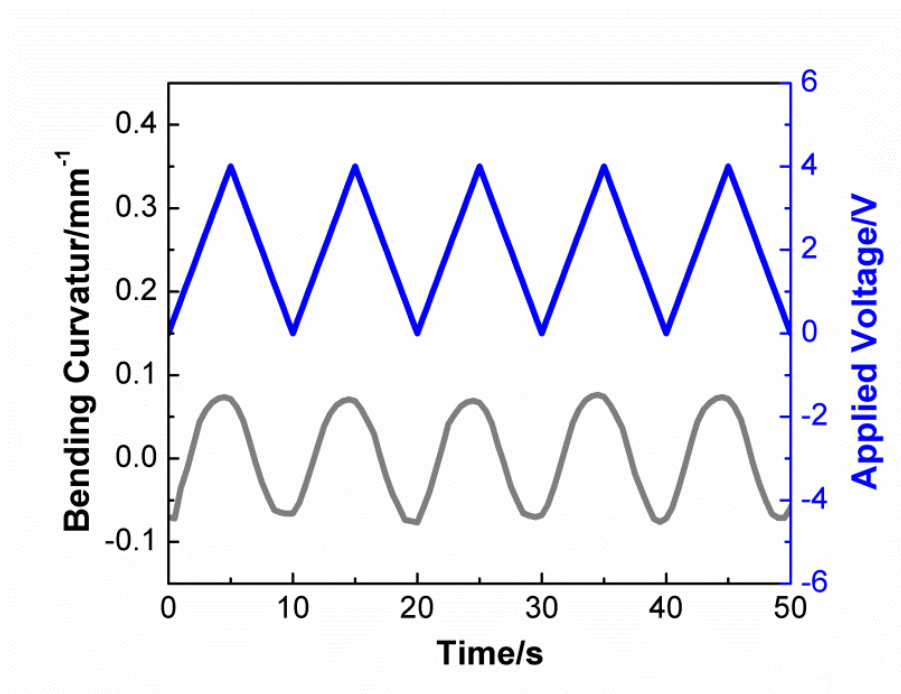


Figure 6-16 Time-dependent diagram of the bending actuation of P(VDF-CTFE) membrane actuator under 4 V 0.1Hz triangle wave

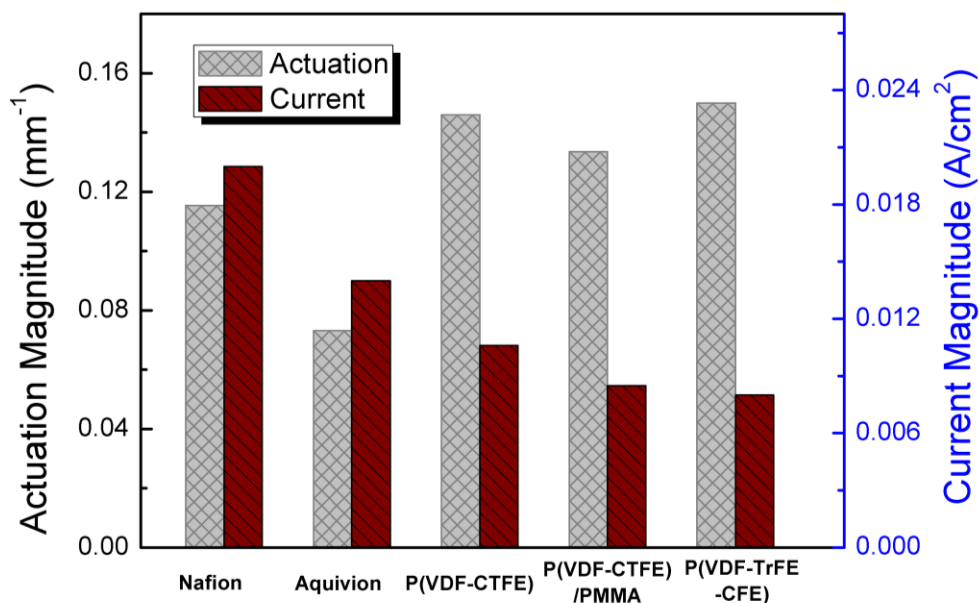


Figure 6-17 Comparison of peak-to-peak bending magnitude and peak-to-peak current consumption of five types of ionic polymer membrane actuators driven by 4V 0.1 Hz triangle stimulus

6.3.3.5 P(VDF-CTFE)/PMMA CNC

As introduced in Chapter 3, with CNC layer, the actuation speed can be improved. Therefore, 3 μm of P(VDF-CTFE)/PMMA with 40 vol% RuO_2 is added to two sides of an P(VDF-CTFE)/PMMA membrane. Since these CNCs are first sprayed onto the P(VDF-CTFE)/PMMA membrane and then melt molded with a hot pressing machine, the morphology or modulus of the actuators may be affected by the pressure or the temperature. After many trials, IPCNC actuator with reasonable bending magnitude was achieved, although the CNC quality may not be ideal yet. To generally illustrate the effect of CNC on actuation speed, bending actuations for P(VDF-CTFE)/PMMA and P(VDF-CTFE)/PMMA with 3 μm CNC are compared in Figure 6-18 and Figure 6-19.

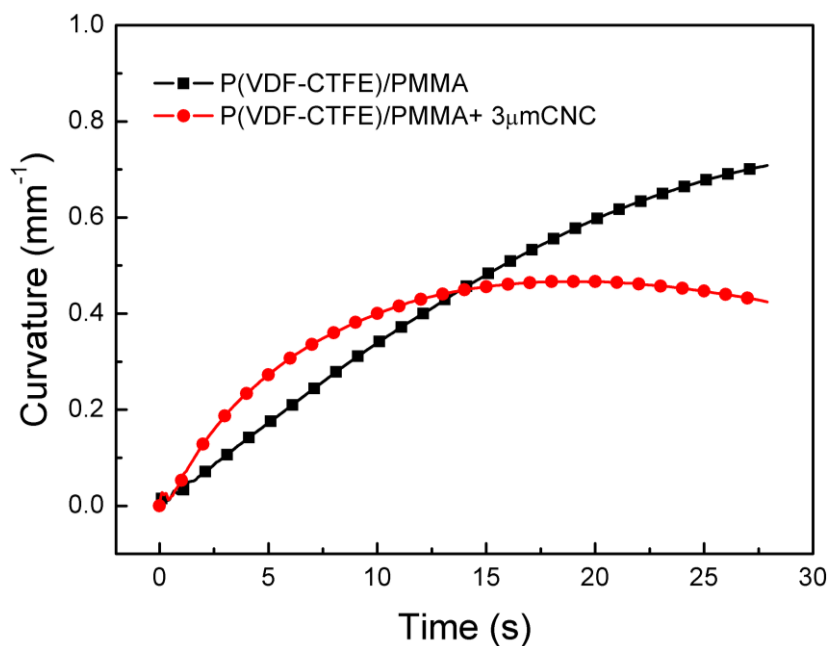


Figure 6-18 Bending curvature of two actuators with 40 wt% EMI-Tf under a 4 V step voltage, including P(VDF-CTFE)/PMMA and P(VDF-CTFE)/PMMA with CNC. CNC is made of P(VDF-CTFE)/PMMA with 40 vol% of RuO_2

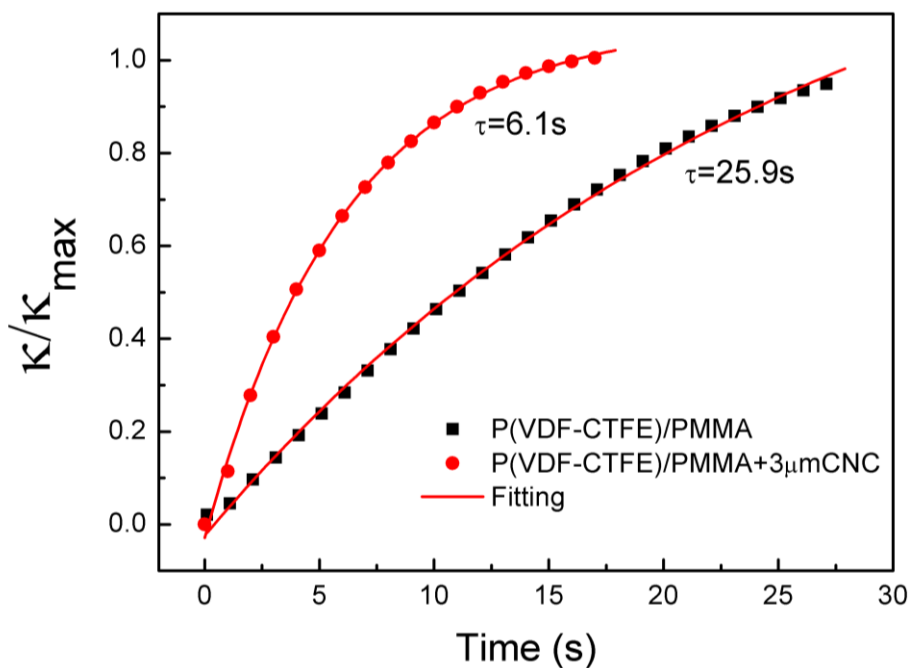


Figure 6-19 Normalized curves of two actuators with 40 wt% EMI-Tf under a 4 V step voltage, including P(VDF-CTFE)/PMMA and P(VDF-CTFE)/PMMA with 3 μm CNC. CNC is made of P(VDF-CTFE)/PMMA with 40 vol% of RuO_2

From figure 6-19, it can be seen that the initial bending actuation magnitude is improved by adding P(VDF-CTFE)/PMMA composite. Since membrane actuators and IPCNC actuators have different morphologies, their intrinsic stresses/strains need to be evaluated with different mechanical models (3 layer model in Section 2.3.1.1 and 5 layer model in Section 2.3.1.2), and thus cannot be compared fairly. However, because the intrinsic strain is proportional to the bending curvature, the actuation speed can be compared by fitting the bending curve to an exponential equation (previously introduced in Chapter 3), as shown in Figure 6-19,

$$S_0(t) = S_{0\max}(1 - e^{-t/\tau}) \quad (6.5)$$

where τ for P(VDF-CTFE)/PMMA without and with CNC are 25.9 s and 6.1s, respectively.

Furthermore, although the bending actuation of IPCNC is complex and the later stage back relaxation is indeed dominated by diffusion of anions, as discussed in Chapter 3 (2 carrier model), it can be found that the P(VDF-CTFE)/PMMA with CNC practically shows a faster response and a higher efficiency in short time scale, as shown in Figure 6-20.

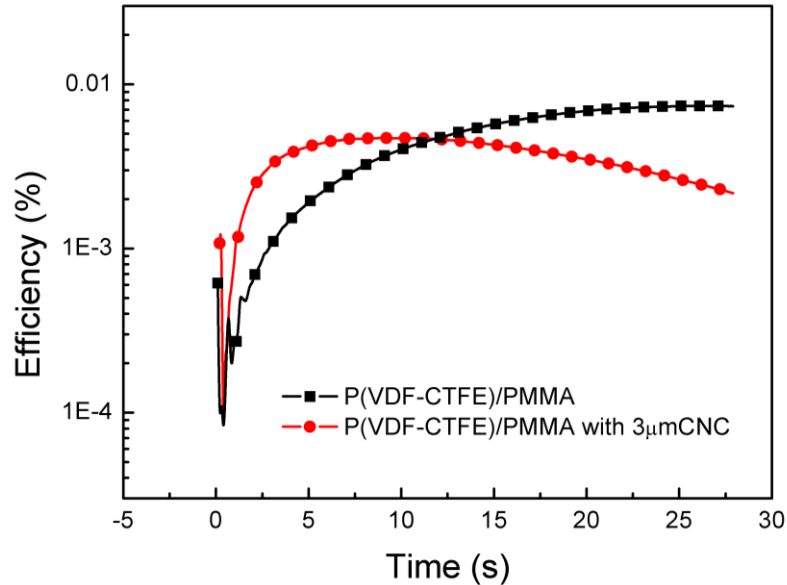


Figure 6-20 Energy conversion efficiency of two actuators with 40 wt% EMI-Tf under a 4 V step voltage, including P(VDF-CTFE)/PMMA and P(VDF-CTFE)/PMMA with CNC. CNC is made of P(VDF-CTFE)/PMMA with 40 vol% of RuO₂

6.4 Conclusion

In conclusion, ionic polymer membrane actuators based on P(VDF-CTFE), P(VDF-CTFE)/PMMA and P(VDF-TrFE-CFE) polymers with 40 wt% of EMI-Tf are investigated.

These actuators exhibit great electromechanical responses in comparison with Nafion and Aquivion perfluorosulfonate ionomers. The improvement in the intrinsic stress charge ratio T_0/C illustrates that the electromechanical coupling between the ionic liquids and the polymer matrix is enhanced by selecting *i*-EAP polymers without flexible side chains or clustered ion channels. Under both DC and AC stimulus, the reduction in charge consumption and the increase in mechanical energy output of the PVDF based membrane actuators lead to order-of-magnitude higher electromechanical energy efficiencies, which indicates that they are valuable *i*-EAP actuator materials.

Furthermore, IPCNC made of P(VDF-CTFE)/PMMA membrane and 3 μm P(VDF-CTFE)/PMMA/RuO₂ composite has also demonstrated a faster device response and better electromechanical coupling at a short time scale (<10s).

Chapter 7

Conclusion and Future Work

7.1 Conclusion

In conclusion, this dissertation studied the bending mechanism and limiting factors of IPCNC actuators and investigated possible solutions towards enhanced performance by decomposing and optimizing the IPCNC actuators by components. In Chapter 3 and 4, CNCs were first analyzed and optimized, and then in Chapter 5 and 6, in-depth studies of ion-polymer interaction were performed on the ionic polymer membranes, where enhancements are also achieved.

The actuation of IPCNC actuators is complicated; therefore two models were built to describe their short time and long time behaviors, as well as the cause of their low efficiencies. Equivalent circuits were established to model the complex frequency-dependent impedance of ionic polymer actuators and the physics behind the impedance elements. Since Warburg diffusion was found in the low frequency responses of Nafion membrane actuators, Warburg impedance was included in new equivalent circuits to model the low frequency diffusion in IPCNC actuators. When there is no CNC or CNC is very thin (tens of nm), a simple equivalent circuit was used to model the impedance response of the ionic polymer actuator, which only consist of Warburg impedance A_w , bulk resistance R , and electric double layer capacitance C_{dl} . It was found that C_{dl} for Nafion with 40 wt% EMI-Tf is $7.5\mu\text{F}/\text{cm}^2$ and increases to $11.4\mu\text{F}/\text{cm}^2$ with increasing surface area of the LbL composite electrode, while the Warburg coefficient A_w remains nearly the same for both devices. As a result, the actuation magnitude and speed increase with charges accumulated due to higher C_{dl} , without much increase in the contribution from the slow ion

diffusion process. When CNC is thick, the simple equivalent circuit with Warburg element was found no longer adequate to model the IPCNCs; therefore, de Levi transmission line was introduced to describe the CNC layer. De Levi transmission line model shows that, thick CNCs lead to a large transport time constant within the CNC layer, so that the IPCNC actuator with thick DAP fabricated Nafion/RuO₂ CNC are slower than that with thin LbL fabricated PAH/Au CNCs.

The analysis of equivalent circuits and actuation is mainly valid for the short time actuation behavior; at longer time scale (>10s), the strain cancellation effect of two carriers starts to dominate the actuation and leads to the back relaxation and low electromechanical efficiency of IPCNC actuators. By combining the time domain electric and electromechanical responses, quantitative information on transport behavior of the two mobile ions in ionic liquids (i.e., cation and anion) in these electroactive devices was obtained from a two carrier model. The result reveals that anions have a larger effective ion size than cations, and thus dominate the long time response of the ionic polymer actuators and cause low electromechanical energy efficiency.

Since CNC limits the transport speed and actuation magnitude, aligned carbon nanotubes (VA-CNTs) with ultrahigh volume fraction were introduced into the fabrication of IPCNC actuators for the purpose of device optimization. High elastic modulus of the VA-CNTs creates an anisotropic elastic response in the composite electrodes, which suppresses the unwanted strain and markedly enhances the actuation strain ($S_0 = 8.2\%$ under 4 V), when compared to RuO₂ actuators ($S_0 = 2\%$ under 4 V). In the meantime, continuous paths through inter-VA-CNT channels and high electrical conduction of the aligned CNTs in the composite electrodes allow fast ion transport, high ionic conductivity, and thus lead to faster device actuation speed ($\tau_0 = 0.82$ s) than RuO₂ IPCNC actuator ($\tau_0 = 3$ s). This fast speed can be understood by developing equivalent circuits for IPCNC actuators, where De Levi transmission line model was simplified and fitted to the data. The fitting results showed that in the VA-CNT actuators, the charge

diffusion process (slow process) becomes comparably less significant than the electric double layer formation (fast process). Hence by properly controlling the nano-morphology of the CNCs to enhance the electric double layer formation and suppress the diffuse layer formation, IPCNC actuator with large strain and fast response was achieved.

Besides CNCs, intrinsic properties of ions transport and storage in ionic polymer are also important to the strain generation. 2-carrier modeling indicated that ions form clusters in their transport and storage process, so that direct observations of the ion distribution in an ionic polymer membrane would provide valuable information about the ion cluster effect. To explore the ion response of ionic liquids under electric field, depth profiles of the electric double layer (EDL) in charged *i*-EAP actuator (Aquivion/1-butyl-2,3-dimethylimidazolium chloride) were collected by Time-of-Flight Secondary Ion Mass Spectrometry (ToF-SIMS) at liquid nitrogen temperature. Experimental results reveal that both cations and anions aggregate near both electrodes due to a strong Coulomb ion-ion correlation, and the ion diffuse layer thicknesses of cations and anions reach 6 μm and 0.5 μm , respectively. This 12 times difference in thickness, together with asymmetric clustering, result from the cation/anion size difference, which is the origin of strain in actuators. These findings emphasized the importance of engineering the electrolyte for IPCNC actuators, as well as provided important experimental data for future theory development.

Finally, the low energy efficiency of ionic polymer actuators was tackled by improving the electromechanical coupling between the ions and the polymer matrix. P(VDF-CTFE), P(VDF-CTFE)/PMMA and P(VDF-TrFE-CFE) polymers with 40 wt% of EMI-Tf exhibit great electromechanical responses in comparison with Nafion and Aquivion perfluorosulfonate ionomers. The improvement in the intrinsic stress charge ratio T_0/C illustrates that the electromechanical coupling between the ionic liquids and the polymer matrix is enhanced by selecting ionic polymers without flexible side chains or clustered ion channels. Under both DC

and AC stimulus, the reduction in charge consumption and the increase in mechanical energy output of the PVDF based membrane actuators lead to order-of-magnitude higher electromechanical energy efficiencies, which indicates that they are valuable *i*-EAP actuator materials. Furthermore, IPCNC made of P(VDF-CTFE)/PMMA membrane and 3 μm P(VDF-CTFE)/PMMA/RuO₂ composite has also demonstrated a faster device response and better electromechanical coupling at a short time scale ($t < 10\text{s}$).

7.2 Future Work

More research directions based on this dissertation are suggested in this section.

Firstly, electrolytes should be engineered to optimize the bending actuation and electromechanical energy conversion efficiency. As shown in this dissertation, one cause of the low energy efficiency of IPCNC actuators is the strain cancellation between the two charge carriers in ionic liquids. Cations and anions form clusters, therefore diminish or even reverse the size ratio between the two types of ions. For example, structurally, EMI⁺ has a larger ion size than BF₄⁻, but from the observation of both NMR and IPCNC actuation, it is found that BF₄⁻ has a larger effective ion size than EMI⁺.

To achieve the optimization, single ion conductors should be further studied. Since single ion conductor does not show back relaxation or have strain cancellation between carriers, they may possess higher energy conversion efficiency. Besides single ion conductor, ionic liquids with large effective ion size difference may also be studied. NMR could be used to filter the suitable ionic liquids, of which the ions have large difference in their effective ion sizes. These ionic liquids could then be soaked into ionic polymers, charged with a dc bias, and studied by ToF-SIMS. The ones with large difference in diffuse layer thickness and less ion clustering will be more efficient in energy conversion and should be tried in IPCNC fabrication.

Secondly, a more complete equivalent circuit, which consists of an electrical branch and an electromechanical branch, should be developed to provide better understanding on how to significantly improve the electromechanical efficiency. Currently, the energy is primarily stored in the actuators as electric energy (in electric double layer capacitance), therefore the electromechanical energy conversion efficiency is very low. Although this dissertation modeled the electric response of the actuators, to fully represent the mechanical response, the electromechanical transduction should also be included in the new equivalent circuit. By varying the experiment condition and compare the fitting result with this improved equivalent circuit, the method to achieve higher efficiency may be found. Besides that, *i*-EAP actuators discussed in this thesis can be also regarded as solid state electric double layer capacitors (electric energy storage device), so that on the other hand, developments towards the reduction of strain are also interesting study topics for electric energy storage.

Thirdly, asymmetric IPCNC actuators may be developed. All the *i*-EAP actuators discussed in this dissertation are built with a symmetric structure, which actually has not been designed purposely. In batteries and supercapacitors, it is common to build hybrid/asymmetric structures to optimize the energy density or operation voltage. In the design of IPCNC actuators, this concept could be adopted for the following reasons.

- (i) The electrochemical window and the specific capacitance of cations and anions are usually asymmetric. Although the electrical double layer capacitances near two electrodes are assumed symmetric in this dissertation and in most of the studies, the difference in cations and anions lead to asymmetric capacitance and voltage drop near two identical electrodes.

As shown in Figure 7-1, when cation and anion possess different sizes, C_1 and C_2 are different from each other, and thus lead to different voltage drops near the two charged electrodes. By purposely varying the surface area of the

electrodes, C_1 and C_2 or V_1 and V_2 can be tuned. Since the electrochemical window varies with the electronegativity of ions. By tuning the C_1/C_2 ratio to the ratio of electrochemical window of the two ions, maximum operation voltage of the ionic liquid can be accessed without introducing electrochemical reactions.

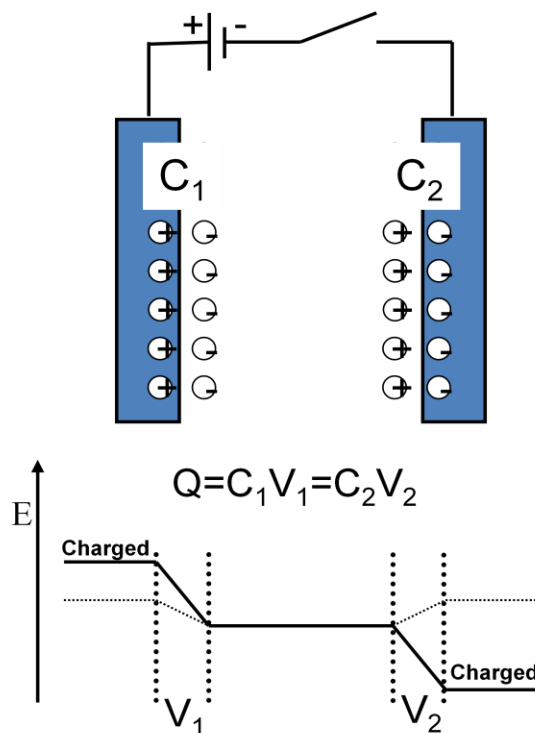


Figure 7-1 Capacitance and voltage drop near two charged electrodes

- (ii) Different polymer materials could be used in tuning the CNCs with enhanced or diminished strain response. By using ionomers or porous polymer materials in one CNC and PVDF polymer in another CNC, the bending actuator will be preferable in certain bending direction without or with reduced back relaxation. This design will make IPCNCs effectively hold their position under DC bias. In a lot of applications, such as medical or robotics, sustaining a constant pressure is crucial to the device performance. By properly design asymmetric IPCNCs, this application requirement will be satisfied.

Finally, more novel materials should be introduced to IPCNC fabrications. Figure 7-2 shows aligned graphene sheets, which might be applied in IPCNC fabrication. Graphene sheets have even larger surface area and volumetric capacitance if densified, which are all desired properties for IPCNCs.

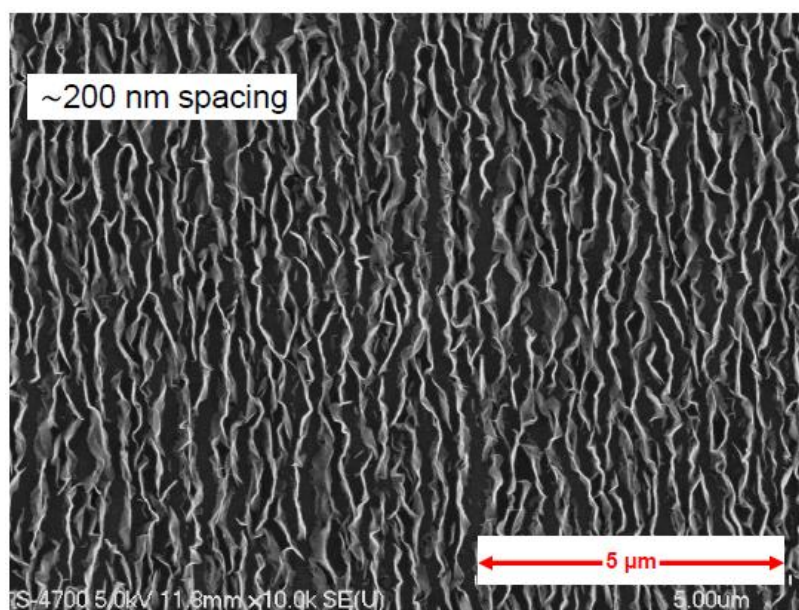


Figure 7-2 SEM image of aligned graphene sheets. [140]

Appendix A: Derivation of Equation (2.6) and (2.12)

(a) Derivation of Equation (2.6)

Due to the symmetry of the structure, $\int dF = 0$ in is always true as below.

$$\begin{aligned} \int dF = & \int_{-(t^m + \frac{t^i}{2})}^{-\frac{t^i}{2}} Y^m \kappa y w dy + \int_{-\frac{t^i}{2}}^0 (Y^i \kappa y - Y^i S_{10}^i) w dy \\ & \int_0^{\frac{t^i}{2}} (Y^i \kappa y + Y^i S_{10}^i) w dy + \int_{\frac{t^i}{2}}^{t^m + \frac{t^i}{2}} Y^m \kappa y w dy = 0 \end{aligned} \quad (1)$$

From $\int dM = 0$, the value of κ needs to satisfy

$$\begin{aligned} \int dM = & \int_{-(t^m + \frac{t^i}{2})}^{-\frac{t^i}{2}} Y^m \kappa y^2 w dy + \int_{-\frac{t^i}{2}}^0 (Y^i \kappa y - Y^i S_{10}^i) y w dy \\ & \int_0^{\frac{t^i}{2}} (Y^i \kappa y + Y^i S_{10}^i) y w dy + \int_{\frac{t^i}{2}}^{t^m + \frac{t^i}{2}} Y^m \kappa y^2 w dy = 0 \end{aligned} \quad (2)$$

Then, after rearranging and equating,

$$S_{10}^i = -\frac{Y^m (8t^{m3} + 12t^{m2}t^i + 6t^m t^{i2}) + Y^i t^{i3}}{3Y^i t^{i2}} \cdot \kappa \quad (3)$$

(b) Derivation of Equation (2.12)

Due to the symmetry of the structure, $\int dF = 0$ in is always true as below.

$$\begin{aligned}
\int dF = & \int_{-(t^m+t^e+\frac{t^i}{2})}^{-(t^e+\frac{t^i}{2})} Y^m \kappa y w dy + \int_{-(t^e+\frac{t^i}{2})}^{-\frac{t^i}{2}} (Y^e \kappa y - Y^e S_{10}^e) w dy + \int_{-\frac{t^i}{2}}^{\frac{t^i}{2}} Y^i \kappa y w dy + \\
& \int_{\frac{t^i}{2}}^{t^e+\frac{t^i}{2}} (Y^e \kappa y + Y^e S_{10}^e) w dy + \int_{t^e+\frac{t^i}{2}}^{t^m+t^e+\frac{t^i}{2}} Y^m \kappa y w dy = 0
\end{aligned} \tag{4}$$

From $\int dM = 0$, the value of κ needs to satisfy

$$\begin{aligned}
\int dM = & \int_{-(t^m+t^e+\frac{t^i}{2})}^{-(t^e+\frac{t^i}{2})} Y^m \kappa y^2 w dy + \int_{-(t^e+\frac{t^i}{2})}^{-\frac{t^i}{2}} (Y^e \kappa y - Y^e S_{10}^e) y w dy + \int_{-\frac{t^i}{2}}^{\frac{t^i}{2}} Y^i \kappa y^2 w dy + \\
& \int_{\frac{t^i}{2}}^{t^e+\frac{t^i}{2}} (Y^e \kappa y + Y^e S_{10}^e) y w dy + \int_{t^e+\frac{t^i}{2}}^{t^m+t^e+\frac{t^i}{2}} Y^m \kappa y^2 w dy = 0
\end{aligned} \tag{5}$$

Then, after rearranging and equating,

$$S_{10}^e = - \frac{Y^m \left(\frac{2t^{m3}}{3} + 2t^m \left(t^m + \frac{t^i}{2} \right)^2 + t^{m2} (2t^e + t^i) \right) + Y^e \left(\frac{2t^{e3}}{3} + t^e \frac{t^{i2}}{2} + t^{e2} t^i \right) + Y^i \frac{t^{i3}}{12}}{Y^e (t^i t^e + t^{e2})} \cdot \kappa$$

(6)

Appendix B: Gouy-Chapman Solution of Poisson-Boltzmann Equation

At large voltages, we cannot linearise the Poisson-Boltzmann equation as the way in Debye-Huckel equation. Instead, the full nonlinear problem for the case of a symmetric dilute electrolyte in one dimension is solved as below, which is referred to as the Gouy-Chapman Model.[59] The Poisson Boltzmann equation in this case is as follows.

$$-\varepsilon \frac{d^2\phi}{dx^2} = \rho_{eq} = c_0 z e (e^{-ze\phi/k_B T} - e^{ze\phi/k_B T}) \quad (1)$$

The equation can be first non-dimensionalized using thermal voltage scale ($\tilde{\phi} = ze\phi/k_B T$) and Debye Length ($\tilde{x} = x/\lambda_D$).

$$\tilde{\phi}'' = \sinh \tilde{\phi} \quad (2)$$

This differential equation can be integrated to obtain the expression of $\tilde{\phi}'$ and $\tilde{\phi}$.

$$\tilde{\phi}' = -2 \sinh(\tilde{\phi}/2) \quad (3)$$

$$\tilde{\phi} = -2 \cosh(\tilde{\phi}/2) \quad (4)$$

Although further integration can be done to deduce the solution of $\tilde{\phi}$, the capacitance is more interested in Gouy-Chapman Model. Since the total charge can be calculated from the following equation, Gouy-Chapman capacitance (C_D) can be deduced.

$$q = -\int_0^\infty \varepsilon \frac{d^2\phi}{dx^2} dx = \varepsilon \frac{d\phi}{dx} \Big|_{x=0} \quad (5)$$

$$\tilde{q} = -2 \sinh(\tilde{\phi}/2) \quad (6)$$

$$\tilde{C}_D = \frac{d\tilde{q}}{d\tilde{\phi}} = \cosh(\tilde{\phi}/2) \quad (7)$$

The dimensional expression of the Gouy-Chapman capacitance can be written and plotted as a function of $\tilde{\phi}$ in the figure below.

$$C_D^{GC} = \frac{\varepsilon}{\lambda_D} \cosh\left(\frac{ze\phi}{2k_B T}\right) \quad (8)$$

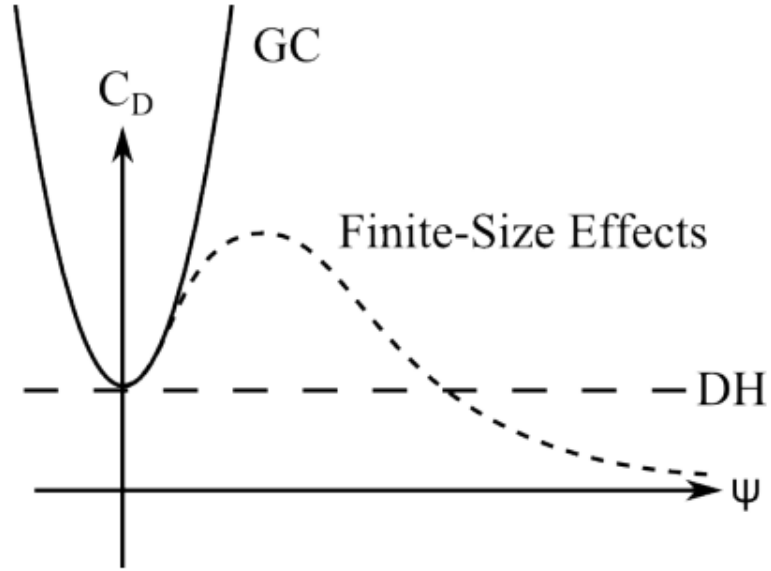


Figure 1. Plots of capacitance in different models GC: Gouy-chapman (non-linear solution of Poisson Boltzmann); DH: Debye-Huckel (linear solution of Poisson Boltzmann). When voltage is small, GC approaches DH. At large potentials, ions begin to concentrate at the strongly charged surface and steric effect limits the capacitance, which is indicated as the dashed line.[59, 141]

Appendix C: Derivation of Warburg Impedance

Assume a small voltage is applied to an ionic system with a linear response in concentration ($\Delta C \ll C_0$),

$$\Delta V = \alpha \Delta C \quad (1)$$

where ΔV is applied voltage, ΔC is the perturbation to the concentration, and α is a coefficient.

The corresponding current due to diffusion always follows the expression below

$$\Delta I = -neAD \frac{\partial C}{\partial x} \quad (2)$$

where n is the number of charge on each ion, A is the electrode area and D is the diffusion coefficient.

Assume the small voltage is an alternating voltage, the expression of voltage, current, and concentration are as below.

$$\Delta V = V e^{i\omega t} \quad (3)$$

$$C(x, t) = C_0 + |\Delta C| e^{i\omega t} \quad (4)$$

Apply Fick's second law (Equation (5)) to Equation (4),

$$\frac{\partial C}{\partial t} = D \frac{\partial^2 C}{\partial x^2} \quad (5)$$

a differential equation of ΔC can be obtained.

$$i\omega \Delta C = D \frac{\partial^2 \Delta C}{\partial x^2} \quad (6)$$

Hence, the solution of this equation with boundary conditions $\Delta C(x=0)=\Delta C^0$ and $\Delta C(x=\infty)=0$ is

$$\Delta C = \Delta C^0 e^{-\sqrt{\frac{i\omega}{D}} x} \quad (7)$$

Inserting Equation (7) into Equation (1) and (2) can deduce ΔV and ΔI .

$$\Delta V = \alpha \Delta C^0 e^{-\sqrt{\frac{i\omega}{D}}x} \quad (8)$$

$$\Delta I = -neA\sqrt{i\omega D}\Delta C^0 e^{-\sqrt{\frac{i\omega}{D}}x} \quad (9)$$

Then impedance Z of the system is as below

$$Z = \frac{\Delta V}{\Delta I} = \frac{\alpha}{neA\sqrt{D}} \frac{1}{\sqrt{i\omega}} = \frac{A_w}{\sqrt{i\omega}} \quad (10)$$

where $A_w = \frac{\alpha}{neA\sqrt{D}}$.

(For the system with electrochemical reactions, Nernst Equations gives the expression of α as

below. $\alpha = \frac{k_B T}{neC_0}$) [59]

References

- [1] W. C. Roentgen, "About the changes in shape and volume of dielectrics caused by electricity," *Ann. Phys. Chem.*, vol. 11, pp. 771-786, 1880.
- [2] Q. M. Zhang, *et al.*, "Giant electrostriction and relaxor ferroelectric behavior in electron-irradiated poly(vinylidene fluoride-trifluoroethylene) copolymer," *Science*, vol. 280, pp. 2101-2104, Jun 1998.
- [3] K. Oguro, *et al.*, "Bending of an ion-conducting polymer film-electrode composite by and electric stimulus at low voltage," *J. Micromachine Soc.*, vol. 5, 1992.
- [4] F. Xia, *et al.*, "High electromechanical responses in a poly(vinylidene fluoride-trifluoroethylene-chlorofluoroethylene) terpolymer (vol 14, pg 1574, 2002)," *Advanced Materials*, vol. 14, pp. 1600-1600, Nov 2002.
- [5] R. H. Baughman, "Conducting polymer artificial muscles," *Synthetic Metals*, vol. 78, pp. 339-353, Apr 1996.
- [6] M. Zhenyl, *et al.*, "HIGH-FIELD ELECTROSTRICTIVE RESPONSE OF POLYMERS," *Journal of Polymer Science Part B-Polymer Physics*, vol. 32, pp. 2721-2731, Dec 1994.
- [7] R. Pelrine, *et al.*, "High-speed electrically actuated elastomers with strain greater than 100%," *Science*, vol. 287, pp. 836-839, Feb 2000.
- [8] Y. Bar-Cohen, *et al.*, "Polymer Piezoelectric Transducers for Ultrasonic NDE," in *First International Workshop on Ultrasonic NDE*, Germany, 1996.
- [9] Y. Bar-Cohen and Q. M. Zhang, "Electroactive polymer actuators and sensors," *Mrs Bulletin*, vol. 33, pp. 173-181, Mar 2008.
- [10] E. Smela, "Conjugated polymer actuators for biomedical applications," *Advanced Materials*, vol. 15, pp. 481-494, Mar 17 2003.
- [11] M. Shahinpoor, "Micro-Electro-Mechanics of Ionic Polymeric Gels As Electrically Controllable Artificial Muscles," *Journal of Intelligent Material Systems and Structures*, vol. 6, pp. 307-314, 1995.

- [12] S. R. Quake and A. Scherer, "From micro- to nanofabrication with soft materials," *Science*, vol. 290, pp. 1536-1540, Nov 2000.
- [13] E. W. H. Jager, *et al.*, "Microfabricating conjugated polymer actuators," *Science*, vol. 290, pp. 1540-1545, Nov 2000.
- [14] Y. Bar-Cohen, "Electroactive polymers as artificial muscles: A review," *Journal of Spacecraft and Rockets*, vol. 39, pp. 822-827, Nov-Dec 2002.
- [15] M. Shahinpoor, *et al.*, "Ionic polymer-metal composites (IPMCs) as biomimetic sensors, actuators and artificial muscles - a review," *Smart Materials & Structures*, vol. 7, pp. R15-R30, Dec 1998.
- [16] D. G. Caldwell, "PSEUDOMUSCULAR ACTUATOR FOR USE IN DEXTEROUS MANIPULATION," *Medical & Biological Engineering & Computing*, vol. 28, pp. 595-600, Nov 1990.
- [17] J. D. W. Madden, *et al.*, "Artificial muscle technology: Physical principles and naval prospects," *Ieee Journal of Oceanic Engineering*, vol. 29, pp. 706-728, Jul 2004.
- [18] NASA. Available: <http://ndea.jpl.nasa.gov/nasa-nde/lommas/eap/EAP-armwrestling.htm>
- [19] B. J. Akle, *et al.*, "High-strain ionomeric-ionic liquid electroactive actuators," *Sensors and Actuators a-Physical*, vol. 126, pp. 173-181, Jan 26 2006.
- [20] N. Terasawa and I. Takeuchi, "Electrochemical property and actuation mechanism of an actuator using three different electrode and same electrolyte in air: Carbon nanotube/ionic liquid/polymer gel electrode, carbon nanotube/ionic liquid gel electrode and Au paste as an electrode," *Sensors and Actuators B-Chemical*, vol. 145, pp. 775-780, Mar 2010.
- [21] L. Bay, *et al.*, "A conducting polymer artificial muscle with 12% linear strain," *Advanced Materials*, vol. 15, pp. 310-313, Feb 17 2003.
- [22] J. D. Madden, *et al.*, "Fast contracting polypyrrole actuators," *Synthetic Metals*, vol. 113, pp. 185-192, Jun 15 2000.
- [23] R. H. Baughman, *et al.*, "Carbon nanotube actuators," *Science*, vol. 284, pp. 1340-1344, May 1999.
- [24] K. Bohon and S. Krause, "An electrorheological fluid and siloxane gel based electromechanical actuator: Working toward an artificial muscle," *Journal of Polymer Science Part B-Polymer Physics*, vol. 36, pp. 1091-1094, Apr 1998.
- [25] I. S. Park, *et al.*, "Physical principles of ionic polymer-metal composites as electroactive actuators and sensors," *Mrs Bulletin*, vol. 33, pp. 190-195, Mar 2008.

- [26] S. Nemat-Nasser, "Micromechanics of actuation of ionic polymer-metal composites," *Journal of Applied Physics*, vol. 92, pp. 2899-2915, Sep 1 2002.
- [27] B. J. Akle, *et al.*, "Direct assembly process: a novel fabrication technique for large strain ionic polymer transducers," *Journal of Materials Science*, vol. 42, pp. 7031-7041, Aug 2007.
- [28] S. Liu, *et al.*, "Layer-by-layer self-assembled conductor network composites in ionic polymer metal composite actuators with high strain response," *Applied Physics Letters*, vol. 95, 2009.
- [29] P. T. Hammond, "Form and function in multilayer assembly: New applications at the nanoscale," *Advanced Materials*, vol. 16, pp. 1271-1293, Aug 2004.
- [30] K. A. Mauritz and R. B. Moore, "State of understanding of Nafion," *Chemical Reviews*, vol. 104, pp. 4535-4585, 2004.
- [31] W. Y. Hsu and T. D. Gierke, "Ion-Transport and Clustering in Nafion Perfluorinated Membranes," *Journal of Membrane Science*, vol. 13, pp. 307-326, 1983.
- [32] S. Nemat-Nassera, *et al.*, "Effect of solvents on the chemical and physical properties of ionic polymer-metal composites," *Journal of Applied Physics*, vol. 99, 2006.
- [33] M. D. Bennett and D. J. Leo, "Ionic liquids as stable solvents for ionic polymer transducers," *Sensors and Actuators a-Physical*, vol. 115, pp. 79-90, 2004.
- [34] W. Lu, *et al.*, "Use of ionic liquids for pi-conjugated polymer electrochemical devices," *Science*, vol. 297, pp. 983-987, 2002.
- [35] D. Kim, *et al.*, "Self-oscillating electroactive polymer actuator," *Applied Physics Letters*, vol. 90, 2007.
- [36] A. B. McEwen, *et al.*, "Electrochemical properties of imidazolium salt electrolytes for electrochemical capacitor applications," *Journal of the Electrochemical Society*, vol. 146, pp. 1687-1695, May 1999.
- [37] M. Ue, *et al.*, "Application of low-viscosity ionic liquid to the electrolyte of double-layer capacitors," *Journal of the Electrochemical Society*, vol. 150, pp. A499-A502, Apr 2003.
- [38] N. Byrne, *et al.*, "The zwitterion effect in ionic liquids: Towards practical rechargeable lithium-metal batteries," *Advanced Materials*, vol. 17, pp. 2497-+, 2005.
- [39] J. H. Shin, *et al.*, "PEO-based polymer electrolytes with ionic liquids and their use in lithium metal-polymer electrolyte batteries," *Journal of the Electrochemical Society*, vol. 152, pp. A978-A983, 2005.

- [40] R. F. de Souza, *et al.*, "Room temperature dialkylimidazolium ionic liquid-based fuel cells," *Electrochemistry Communications*, vol. 5, pp. 728-731, Aug 2003.
- [41] P. Wang, *et al.*, "Charge separation and efficient light energy conversion in sensitized mesoscopic solar cells based on binary ionic liquids," *Journal of the American Chemical Society*, vol. 127, pp. 6850-6856, 2005.
- [42] R. Kawano, *et al.*, "High performance dye-sensitized solar cells using ionic liquids as their electrolytes," *Journal of Photochemistry and Photobiology a-Chemistry*, vol. 164, pp. 87-92, Jun 1 2004.
- [43] S. Liu, "HIGH ELECTROMECHANICAL RESPONSE ELECTROACTIVE POLYMERS AND THEIR APPLICATIONS FOR SOLID STATE ACTUATORS," Ph. D., Electrical Engineering, Pennsylvania State University, University Park, 2010.
- [44] Available: <http://www.geos.ed.ac.uk/facilities/ionprobe/SIMS4.pdf>
- [45] D. Touboul, *et al.*, "Tissue molecular ion imaging by gold cluster ion bombardment," *Analytical Chemistry*, vol. 76, pp. 1550-1559, Mar 15 2004.
- [46] P. Sjoval, *et al.*, "Mass spectrometric imaging of lipids in brain tissue," *Analytical Chemistry*, vol. 76, pp. 4271-4278, Aug 1 2004.
- [47] T. L. Colliver, *et al.*, "Atomic and molecular imaging at the single-cell level with TOF-SIMS," *Analytical Chemistry*, vol. 69, pp. 2225-2231, Jul 1 1997.
- [48] S. G. Ostrowski, *et al.*, "Mass spectrometric imaging of highly curved membranes during Tetrahymena mating," *Science*, vol. 305, pp. 71-73, Jul 2 2004.
- [49] D. Weibel, *et al.*, "A C-60 primary ion beam system for time of flight secondary ion mass spectrometry: Its development and secondary ion yield characteristics," *Analytical Chemistry*, vol. 75, pp. 1754-1764, Apr 1 2003.
- [50] N. Winograd, "The magic of cluster SIMS," *Analytical Chemistry*, vol. 77, pp. 142a-149a, Apr 1 2005.
- [51] C. M. Mahoney, *et al.*, "Depth profiling of 4-acetaminophenol-doped poly(lactic acid) films using cluster secondary ion mass spectrometry," *Analytical Chemistry*, vol. 76, pp. 3199-3207, Jun 1 2004.
- [52] J. Cheng and N. Winograd, "Depth profiling of peptide films with TOF-SIMS and a C-60 probe," *Analytical Chemistry*, vol. 77, pp. 3651-3659, Jun 1 2005.
- [53] A. G. Sostarecz, *et al.*, "Depth profiling studies of multilayer films with a C-60(+) ion source," *Applied Surface Science*, vol. 231, pp. 179-182, Jun 15 2004.

- [54] M. S. Wagner, "Molecular depth profiling of multilayer polymer films using time-of-flight secondary ion mass spectrometry," *Analytical Chemistry*, vol. 77, pp. 911-922, Feb 1 2005.
- [55] C. M. McQuaw, *et al.*, "Lateral heterogeneity of dipalmitoylphosphatidylethanolamine-cholesterol Langmuir-Blodgett films investigated with imaging time-of-flight secondary ion mass spectrometry and atomic force microscopy," *Langmuir*, vol. 21, pp. 807-813, Feb 1 2005.
- [56] J. Kozole, *et al.*, "Energy deposition during molecular depth profiling experiments with cluster ion beams," *Analytical Chemistry*, vol. 80, pp. 5293-5301, Jul 15 2008.
- [57] B. E. Conway, *Electrochemical supercapacitors : scientific fundamentals and technological applications*. New York: Plenum Press, 1999.
- [58] J. H. Lin, *et al.*, "Charge dynamics and bending actuation in Aquivion membrane swelled with ionic liquids," *Polymer*, vol. 52, pp. 540-546, Jan 21 2011.
- [59] C. Lim, "IV. Transport Phenomena in Lecture Notes for Electrochemical Energy Systems," 2011.
- [60] R. J. Klein, *et al.*, "Modeling electrode polarization in dielectric spectroscopy: Ion mobility and mobile ion concentration of single-ion polymer electrolytes," *Journal of Chemical Physics*, vol. 124, 2006.
- [61] R. Coelho, "On the Static Permittivity of Dipolar and Conductive Media - an Educational-Approach," *Journal of Non-Crystalline Solids*, vol. 131, pp. 1136-1139, Jun 1991.
- [62] J. R. Macdonald, "Theory of Ac Space-Charge Polarization Effects in Photoconductors, Semiconductors, and Electrolytes," *Physical Review*, vol. 92, pp. 4-17, 1953.
- [63] F. Beunis, *et al.*, "Dynamics of charge transport in planar devices," *Physical Review E*, vol. 78, 2008.
- [64] M. Z. Bazant. (2011, Chapter V Electrostatics in Lecture Notes for Electrochemical Energy Systems. Available: <http://ocw.mit.edu/courses/chemical-engineering/10-626-electrochemical-energy-systems-spring-2011/lecture-notes/>
- [65] M. Z. Bazant, *et al.*, "Diffuse-charge dynamics in electrochemical systems," *Physical Review E*, vol. 70, 2004.
- [66] M. S. Kilic, *et al.*, "Steric effects in the dynamics of electrolytes at large applied voltages. I. Double-layer charging," *Physical Review E*, vol. 75, 2007.

- [67] F. Beunis, *et al.*, "Diffuse double layer charging in nonpolar liquids," *Applied Physics Letters*, vol. 91, 2007.
- [68] M. Marescaux, *et al.*, "Impact of diffusion layers in strong electrolytes on the transient current," *Physical Review E*, vol. 79, 2009.
- [69] F. Strubbe, *et al.*, "Generation current of charged micelles in nonaqueous liquids: Measurements and simulations," *Journal of Colloid and Interface Science*, vol. 300, pp. 396-403, 2006.
- [70] R. Montazami, *et al.*, *Thickness dependence of curvature, strain, and response time in ionic electroactive polymer actuators fabricated via layer-by-layer assembly* vol. 109: AIP, 2011.
- [71] S. Liu, *et al.*, "Influence of the conductor network composites on the electromechanical performance of ionic polymer conductor network composite actuators," *Sensors and Actuators a-Physical*, vol. 157, pp. 267-275, Feb 2010.
- [72] G. Decher, "Fuzzy nanoassemblies: Toward layered polymeric multicomposites," *Science*, vol. 277, pp. 1232-1237, Aug 29 1997.
- [73] J. E. B. Randles, "Kinetics of Rapid Electrode Reactions," *Discussions of the Faraday Society*, vol. 1, pp. 11-19, 1947.
- [74] P. Delahay, *New Instrumental Methods in Electrochemistry* vol. Chap. 7. New York: Wiley-Interscience, 1954.
- [75] A. J. Bard and L. R. Faulkner, *Electrochemical Methods: Fundamentals and Applications*, 2nd ed.: Wiley, 2000.
- [76] J. Bisquert and A. Compte, "Theory of the electrochemical impedance of anomalous diffusion," *Journal of Electroanalytical Chemistry*, vol. 499, pp. 112-120, Feb 23 2001.
- [77] R. de Levie, *Advances in Electrochemistry and Electrochemical Engineering* vol. 6. New York: Wiley-Interscience, 1967.
- [78] S. Liu, *et al.*, "Influence of imidazolium-based ionic liquids on the performance of ionic polymer conductor network composite actuators," *Polymer International*, vol. 59, pp. 321-328, Mar 2010.
- [79] S. Frank, *et al.*, "Carbon nanotube quantum resistors," *Science*, vol. 280, pp. 1744-1746, Jun 12 1998.
- [80] W. J. Liang, *et al.*, "Fabry-Perot interference in a nanotube electron waveguide," *Nature*, vol. 411, pp. 665-669, Jun 2001.

- [81] R. H. Baughman, *et al.*, "Carbon nanotubes - the route toward applications," *Science*, vol. 297, pp. 787-792, Aug 2 2002.
- [82] P. Kim, *et al.*, "Thermal transport measurements of individual multiwalled nanotubes," *Physical Review Letters*, vol. 87, Nov 19 2001.
- [83] M. Kociak, *et al.*, "Superconductivity in ropes of single-walled carbon nanotubes," *Physical Review Letters*, vol. 86, pp. 2416-2419, Mar 12 2001.
- [84] Z. K. Tang, *et al.*, "Superconductivity in 4 angstrom single-walled carbon nanotubes," *Science*, vol. 292, pp. 2462-2465, Jun 29 2001.
- [85] E. W. Wong, *et al.*, "Nanobeam mechanics: Elasticity, strength, and toughness of nanorods and nanotubes," *Science*, vol. 277, pp. 1971-1975, Sep 26 1997.
- [86] M. F. Yu, *et al.*, "Tensile loading of ropes of single wall carbon nanotubes and their mechanical properties," *Physical Review Letters*, vol. 84, pp. 5552-5555, Jun 12 2000.
- [87] A. Thess, *et al.*, "Crystalline ropes of metallic carbon nanotubes," *Science*, vol. 273, pp. 483-487, Jul 26 1996.
- [88] H. W. Zhu, *et al.*, "Direct synthesis of long single-walled carbon nanotube strands," *Science*, vol. 296, pp. 884-886, May 3 2002.
- [89] L. M. Ericson, *et al.*, "Macroscopic, neat, single-walled carbon nanotube fibers," *Science*, vol. 305, pp. 1447-1450, Sep 3 2004.
- [90] Y. L. Li, *et al.*, "Direct spinning of carbon nanotube fibers from chemical vapor deposition synthesis," *Science*, vol. 304, pp. 276-278, Apr 9 2004.
- [91] K. L. Jiang, *et al.*, "Nanotechnology: Spinning continuous carbon nanotube yarns - Carbon nanotubes weave their way into a range of imaginative macroscopic applications.," *Nature*, vol. 419, pp. 801-801, Oct 24 2002.
- [92] Z. F. Ren, *et al.*, "Synthesis of large arrays of well-aligned carbon nanotubes on glass," *Science*, vol. 282, pp. 1105-1107, Nov 6 1998.
- [93] S. S. Fan, *et al.*, "Self-oriented regular arrays of carbon nanotubes and their field emission properties," *Science*, vol. 283, pp. 512-514, Jan 22 1999.
- [94] K. Hata, *et al.*, "Water-assisted highly efficient synthesis of impurity-free single-walled carbon nanotubes," *Science*, vol. 306, pp. 1362-1364, Nov 19 2004.
- [95] D. T. Welna, *et al.*, "Vertically aligned carbon nanotube electrodes for lithium-ion batteries," *Journal of Power Sources*, vol. 196, pp. 1455-1460, Feb 1 2011.
- [96] K. Evanoff, *et al.*, "Towards Ultrathick Battery Electrodes: Aligned Carbon Nanotube - Enabled Architecture," *Advanced Materials*, vol. 24, pp. 533+, Jan 24 2012.

- [97] D. N. Futaba, *et al.*, "Shape-engineerable and highly densely packed single-walled carbon nanotubes and their application as super-capacitor electrodes," *Nature Materials*, vol. 5, pp. 987-994, Dec 2006.
- [98] W. Lu, *et al.*, "High performance electrochemical capacitors from aligned carbon nanotube electrodes and ionic liquid electrolytes," *Journal of Power Sources*, vol. 189, pp. 1270-1277, Apr 15 2009.
- [99] S. Iijima and T. Ichihashi, "Single-Shell Carbon Nanotubes of 1-Nm Diameter," *Nature*, vol. 363, pp. 603-605, Jun 17 1993.
- [100] Webpage. Available: http://en.wikipedia.org/wiki/Carbon_nanotube#Discovery
- [101] E. Frackowiak, *et al.*, "Nanotubular materials as electrodes for supercapacitors," *Fuel Processing Technology*, vol. 77, pp. 213-219, Jun 20 2002.
- [102] L. Ci, *et al.*, "Continuous carbon nanotube reinforced composites," *Nano Letters*, vol. 8, pp. 2762-2766, Sep 2008.
- [103] H. Cebeci, *et al.*, "Multifunctional properties of high volume fraction aligned carbon nanotube polymer composites with controlled morphology," *Composites Science and Technology*, vol. 69, pp. 2649-2656, Dec 2009.
- [104] A. J. Hart and A. H. Slocum, "Rapid growth and flow-mediated nucleation of millimeter-scale aligned carbon nanotube structures from a thin-film catalyst," *Journal of Physical Chemistry B*, vol. 110, pp. 8250-8257, 2006.
- [105] E. J. Garcia, *et al.*, "Long carbon nanotubes grown on the surface of fibers for hybrid composites," *Aiaa Journal*, vol. 46, pp. 1405-1412, 2008.
- [106] A. J. Hart and A. H. Slocum, "Force output, control of film structure, and microscale shape transfer by carbon nanotube growth under mechanical pressure," *Nano Letters*, vol. 6, pp. 1254-1260, Jun 2006.
- [107] B. L. Wardle, *et al.*, "Fabrication and characterization of ultrahigh-volume-fraction aligned carbon nanotube-polymer composites," *Advanced Materials*, vol. 20, pp. 2707-+, Jul 17 2008.
- [108] Y. Liu, *et al.*, "Ion transport and storage of ionic liquids in ionic polymer conductor network composites," *Applied Physics Letters*, vol. 96, 2010.
- [109] M. Z. Bazant, *et al.*, "Double Layer in Ionic Liquids: Overscreening versus Crowding," *Physical Review Letters*, vol. 106, Jan 24 2011.
- [110] M. Mezger, *et al.*, "Molecular layering of fluorinated ionic liquids at a charged sapphire (0001) surface," *Science*, vol. 322, pp. 424-428, Oct 17 2008.

- [111] H. Zhao, "Diffuse-charge dynamics of ionic liquids in electrochemical systems," *Physical Review E*, vol. 84, Nov 15 2011.
- [112] B. Skinner, *et al.*, "Capacitance of the Double Layer Formed at the Metal/Ionic-Conductor Interface: How Large Can It Be?," *Physical Review Letters*, vol. 104, Mar 2010.
- [113] L. L. Zheng, *et al.*, "Retrospective sputter depth profiling using 3D mass spectral imaging," *Surface and Interface Analysis*, vol. 43, pp. 41-44, Jan-Feb 2011.
- [114] T. Singh and A. Kumar, "Static Dielectric Constant of Room Temperature Ionic Liquids: Internal Pressure and Cohesive Energy Density Approach," *Journal of Physical Chemistry B*, vol. 112, pp. 12968-12972, Oct 16 2008.
- [115] M. Kunze, *et al.*, "New Insights to Self-Aggregation in Ionic Liquid Electrolytes for High-Energy Electrochemical Devices," *Advanced Energy Materials*, vol. 1, pp. 274-281, Mar 18 2011.
- [116] M. V. Fedorov and A. A. Kornyshev, "Towards understanding the structure and capacitance of electrical double layer in ionic liquids," *Electrochimica Acta*, vol. 53, pp. 6835-6840, Oct 1 2008.
- [117] L. Onsager, "Theories of concentrated electrolytes," *Chemical Reviews*, vol. 13, pp. 73-89, Aug 1933.
- [118] K. J. Laidler and J. H. Meiser, *Physical chemistry*, 3rd ed. Boston: Houghton Mifflin, 1999.
- [119] A. Eisenberg, *et al.*, "A New Multiplet-Cluster Model for the Morphology of Random Ionomers," *Macromolecules*, vol. 23, pp. 4098-4107, Sep 3 1990.
- [120] Y. K. Hyon, *et al.*, "Energy Variational Approach To Study Charge Inversion (Layering) Near Charged Wall," *Discrete and Continuous Dynamical Systems* In press.
- [121] J. N. A. C. Lopes and A. A. H. Padua, "Nanostructural organization in ionic liquids," *Journal of Physical Chemistry B*, vol. 110, pp. 3330-3335, Feb 23 2006.
- [122] A. A. H. Padua, *et al.*, "Molecular solutes in ionic liquids: A structural, perspective," *Accounts of Chemical Research*, vol. 40, pp. 1087-1096, Nov 2007.
- [123] Y. T. Wang and G. A. Voth, "Tail aggregation and domain diffusion in ionic liquids," *Journal of Physical Chemistry B*, vol. 110, pp. 18601-18608, Sep 21 2006.
- [124] A. Seduraman, *et al.*, "Characterization of nano-domains in ionic liquids with molecular simulations," *Calphad-Computer Coupling of Phase Diagrams and Thermochemistry*, vol. 33, pp. 605-613, Sep 2009.

- [125] A. Triolo, *et al.*, "Nanoscale segregation in room temperature ionic liquids," *Journal of Physical Chemistry B*, vol. 111, pp. 4641-4644, May 10 2007.
- [126] A. Triolo, *et al.*, "Nanoscale organization in piperidinium-based room temperature ionic liquids," *Journal of Chemical Physics*, vol. 130, Apr 28 2009.
- [127] C. Hardacre, *et al.*, "Small angle neutron scattering from 1-alkyl-3-methylimidazolium hexafluorophosphate ionic liquids ([C(n)mim][PF(6)], n=4, 6, and 8)," *Journal of Chemical Physics*, vol. 133, Aug 21 2010.
- [128] M. D. Bennett, "Electromechanical Transduction in Ionic Liquid–Swollen Nafion Membranes," Ph. D, Department of Mechanical Engineering, Virginia Polytechnic Institute and State University, Blacksburg, VA, 2005.
- [129] C. Schmidt, *et al.*, "Modification of Nafion membranes by impregnation with ionic liquids," *Chemical Engineering & Technology*, vol. 31, pp. 13-22, Jan 2008.
- [130] K. A. Page, *et al.*, "Molecular origins of the thermal transitions and dynamic mechanical relaxations in perfluorosulfonate ionomers," *Macromolecules*, vol. 38, pp. 6472-6484, Jul 2005.
- [131] Z. M. Li, *et al.*, "Electromechanical properties of poly(vinylidene-fluoride-chlorotrifluoroethylene) copolymer," *Applied Physics Letters*, vol. 88, Feb 2006.
- [132] R. J. Klein, *et al.*, "Influence of composition on relaxor ferroelectric and electromechanical properties of poly(vinylidene fluoride-trifluoroethylene-chlorotrifluoroethylene)," *Journal of Applied Physics*, vol. 97, May 2005.
- [133] C. Ishiyama and Y. Higo, "Effects of humidity on Young's modulus in poly(methyl methacrylate)," *Journal of Polymer Science Part B-Polymer Physics*, vol. 40, pp. 460-465, Mar 1 2002.
- [134] T. Kashiwagi, *et al.*, "Thermal and Oxidative-Degradation of Poly(Methyl Methacrylate) - Molecular-Weight," *Macromolecules*, vol. 18, pp. 131-138, 1985.
- [135] K. D. Kreuer, *et al.*, "Short-side-chain proton conducting perfluorosulfonic acid ionomers: Why they perform better in PEM fuel cells," *Journal of Power Sources*, vol. 178, pp. 499-509, Apr 1 2008.
- [136] A. Ghielmi, *et al.*, "Proton exchange membranes based on the short-side-chain perfluorinated ionomer," *Journal of Power Sources*, vol. 145, pp. 108-115, 2005.
- [137] H. S. Nalwa, *Ferroelectric polymers : chemistry, physics, and applications*. New York: M. Dekker, Inc., 1995.

- [138] Q. M. Wang, *et al.*, "Nonlinear piezoelectric behavior of ceramic bending mode actuators under strong electric fields," *Journal of Applied Physics*, vol. 86, pp. 3352-3360, Sep 15 1999.
- [139] S. Liu, *et al.*, "Layer-by-layer self-assembled conductor network composites in ionic polymer metal composite actuators with high strain response," *Applied Physics Letters*, vol. 95, pp. -, Jul 13 2009.
- [140] J. R. Miller, *et al.*, "Graphene Double-Layer Capacitor with ac Line-Filtering Performance," *Science*, vol. 329, pp. 1637-1639, Sep 2010.
- [141] A. A. Kornyshev, "Double-layer in ionic liquids: Paradigm change?," *Journal of Physical Chemistry B*, vol. 111, pp. 5545-5557, May 2007.

VITA

Yang Liu

Yang Liu was born on February 7th, 1982 in Tianjin, China. She received the Bachelor of Science degree in Physics from University of Science and Technology of China in 2004 and the Master of Science degree in Physics from Northeastern University in 2008. In 2008, she started her Ph.D. study in Department of Electrical Engineering at the Pennsylvania State University under supervision of Prof. Qiming Zhang. Her research focused on the high performance ionic electroactive polymers and their applications in actuators. Up to 2012, she has tens of publications in the field and is a co-inventor of two U.S. patents. Yang Liu is a member of Materials Research Society (MRS) and Society of Photographic Instrumentation Engineers (SPIE).